Doctoral Dissertation

Experimental study on motion control of dual-arm full/semi-autonomous underwater robots

Radzi Bin Ambar
(Student Number: 12584204)

Supervisor: Associate Professor Dr. Shinichi Sagara

Department of Mechanical and Control Engineering
Graduate School of Engineering
Kyushu Institute of Technology

July, 2015

Contents

Chapter 1

Introduction

1.1 Research overview

1.1.1 The significant contributions of underwater robots

It is unquestionable that two most exciting and intriguing exploration of this century are space and ocean. "Space: the final frontier" is a phrase from the 1960's television movie called Star Trek, portraying the effort of humanity exploring deep space hoping to meet other life forms and civilization [1]. The phrase became popular in the early stages of space exploration race, between the United States of America and Soviet Union. Since the Soviet successfully launched the first artificial satellite Sputnik 1 into the orbit in 1957, tremendous efforts involving money, time and exposure have been put forward towards the space-age exploration. But, only few knew that ocean exploration have been done by humans for thousands of years ago.

Undocumented facts suggested that ocean exploration started around 4500 B.C. in coastal cultures such as in Greece and China. Human began diving into the sea as a source for food gathering and commerce. While in between 1519 to 1522, Ferdinand Magellan's ship explored the surface of the ocean by being the first to circumnavigate the world [2]. On 23rd January 1960, oceanographer Jacques Piccard and Lt. Don Walsh of United States Navy explored to the deepest part of the Earth's ocean. Both were the only crew inside a submersible vehicle called Trieste, the first manned or unmanned vessel to reach the deepest point of Challenger Deep in the Mariana Trench, believed to be the deepest point of the sea at a depth of 10,916[m] [3]. Though, despite these achievements, hundred of millions of dollars are still being spent in high-tech earth based telescope, designing space rocket thrusters and sending space probes for studying planets and beyond our solar system.

The author need to stress that Earth's ocean still have a lot to offer in term

of exploring new world that still never been seen by human. Water covers 71% of Earth surface [4–6]. To be more specific, 96.5% of Earth's water can be found in the ocean [6]. Ocean covers a large of the earth, which is relatively less explored. Until recently, to discover the secret in the depth of the sea seems impossible. Furthermore, ocean exploratory activities involving manned underwater vehicle exposed the operator to extreme conditions which may be dangerous such as underwater pressure, visual visibility and oxygen supply problems. These problems have been resolved by underwater vehicle involving robotic manipulator technology.

Underwater vehicles have been heavily involved in various underwater activities especially related to intervention tasks [7–11]. Many of these robots utilized master-slave system where human operators remotely controlling the motions of underwater vehicles and robotic manipulators using controllers from the surface. Since the technology of fully autonomous underwater vehicles for intervention tasks are still in research and developing stages, master-slave control of underwater robots are still the most relevant today. Underwater robots have been utilized in various fields such as scientific explorations, oceans construction, oil and gas explorations, military and even search and rescue operations.

On 12th August 2000, Russian submarine K-141 Kursk sank into the bottom of the Barents Sea after an explosion of one of its torpedo, resulting to the catastrophic second detonation of further torpedoes. With no capability of rescuing on this type of disaster and the delay of accepting aid from other countries by the Russian government resulting to the death of 23 crews who actually remained alive and trapped in one of the submarine's compartment. Remotely operated vehicles (ROVs), Sea Owl and SCV 006 assisted human divers to inspect signs of life on board the submarine using high-tech cameras and powerful underwater torch [7]. However, the deployment of these vehicles to assist the rescue mission was far too late. Another Russian mini-submarine called AS-28 Priz get caught on nets and antenna cables off the Kamchatka Peninsula in Russia. Seven Russian sailors trapped inside the submarine were rescued using a British remotely-controlled ROV called Scorpio 45 [12,13]. The single-manipulator arm equipped ROV sliced through nets that entangled the submarine, and freed the sailors. Since then, the Russian have been busy preparing the navy fleet with underwater vehicle technology [14, 15]. Whereas, the United States navy have gone further steps, recognizing the high impact of underwater vehicle technology by developing underwater spy robot for military purposes [16].

An autonomous underwater vehicle (AUV) called SeaBED was used by a group of antarctic scientists to demonstrate that the Antarctic sea ice are much thicker and more deformed than previously reported [8,17]. The scientists utilized a combination of data based on multi-beam sonar from the AUV with satellite data to present a

3-dimensional maps of sea-ice draft for ten floes (large floating ice), near coastal regions of the Weddel, Bellingshausen and Wilkes Land sectors of Antarctica. The mean drafts thickness ranged from 1.4 to 5.5[m], with the thickest draft measuring 16[m], and an average of 76 percent of the ice volume showed deformity.

In the Deepwater Horizon oil spill tragedy in the Gulf of Mexico, about a dozen of tethered ROVs were utilized to contain the oil spill successfully [9]. Deep Horizon was a deepwater semi-submersible mobile oil platform that was capable to operate in waters up to 2,400[m] deep, and maximum drill depth of 9,100[m]. The tragedy that killed 11 workers was caused by an explosion of the offshore oil platform that eventually sinking the platform and causing the largest marine oil spill in history. ROVs equipped with robotic manipulators were used to saw off the platform's busted pipe and positioned a four-story dome over the oil well, and installed a smaller oil-collecting cap in its place to seal off the oil from gushing out of the drill pipe [18]. On July 15, 2010, the flow of oil was stopped for the first time in 86 days [9].

A HUGIN 3000 AUV and Oceaneering Millennium VI ROV were used for archaeological and historically related work to investigate a sunken shipwreck SS Robert E. Lee and a Russian submarine U-166 in the Gulf of Mexico [10, 19]. In 2001, the untethered HUGGIN AUV surveyed a 2-mile by 1.5-mile of underwater area and detected the shipwreck SS Robert E. Lee and U-166 using sonar and multi-beam bathymetry images. The tethered Millennium ROV was used to visually confirmed the findings. U-boats such as U-166 were sent by Germany's Hitler during World War 2 to destroy petroleum and merchant related ships. U-166 was the only of such submarine destroyed in the gulf of Mexico. On the hand, SS Robert E. Lee was the last ship destroyed by the U-166. Due to the use of underwater robotics in the surveys and verifications, one of the most fascinating historical finds of World War 2 was solved.

Woods Hole Oceanographic Institution's AUV called Sentry combined with mass spectrometer and various sensors was deployed to track, localize and characterize a sub-sea hydrocarbon plume caused by the Deepwater Horizon oil spill incident [11, 20]. By doing this, scientists were able to assess the impact of the incident towards biological communities deep underwater. The scientists discovered that the depth of the plume was approximately 1100[m] and extending 30[km] from the Deepwater Horizon site. Sentry was also used to identify biological communities that grow on rugged seafloors due to its capabilities for long range missions, durability and speed.

From the above explanations regarding the significant contribution of underwater vehicles in various activities, it is clearly understood that underwater vehicles are the perfect tools to enable human to execute impossible tasks. There are many more examples that show underwater robotic technologies has been widely accepted

and became an essential part of researchers and related works [21–25]. Based on these examples, the various types of underwater robots that are built for various specialized missions will be explained in the next section.

1.1.2 Research and development on underwater robots

Generally, underwater vehicles can be classified into Manned Underwater Vehicles (MUVs) and Unmanned Underwater Vehicles (UUVs) [26, 40].

According to Blidberg [26], MUVs can be further classified into military submarines and non-military submarines. There are various types and classes of military submarines operated by navies around the world. These submarines are usually massive in term of size and can occupy large number of crew. Non-military submarines are usually allow small number of crew due to its smaller size. Usually non-military submarines are utilized for underwater scientific missions such as sub-sea biological communities observations and sample collections. These type of submarines are also equipped with various sensors and robotic manipulators.

UUVs are basically underwater robots that can be classified into Remotely Operated Vehicle (ROV) and Autonomous Underwater Vehicle (AUV). ROVs are underwater robots that are linked to a remotely located human operator on surface platform/ship via tether. Usually skilled human operators will use specialized interface device/master controllers to perform various underwater intervention tasks. The power supplies for the ROV and data communications are made possible using tether. Examples of studies related to ROVs are VORTEX from France [27], KAIKO from JAMSTEC, Japan [28] and HEMIRE from KORDI, Korea [29]. A collection of manufacturers of ROVs can be found in [40]. On the other hand, AUVs are UUVs that can be either fully-Autonomous Underwater Vehicle (fully-AUV) or semi-Autonomous Underwater Vehicle (semi-AUV). Both of these vehicles are equipped with on-board power supplies and control system to accomplish a predefined mission [41]. AUVs are usually not physically linked to a surface ship/platform via tether. However, there are semi-AUVs that have functionality that similar as ROV, where the power supplies, data communications and commands are transferred via tether system [30–32]. AUVs are mainly developed by research institutes focusing on designing intelligent decision-making capabilities of AUVs robotic architecture for autonomy. They are commonly utilized for autonomous underwater monitoring or survey operations. AUVs have been studied and developed extensively by researchers concerned with underwater robotics such as the OTTER from Stanford University [33], ODIN and SAUVIM from University of Hawaii [34, 35], RAUVI, ALIVE and AMADEUS from groups of European universities [36–38] and

Twin Burgers from the University of Tokyo [39]. Many more AUV models can be found in [41] and [42].

ROVs and AUVs that are equipped with a single or multiple robotic manipulators are usually called Underwater Vehicle-Manipulator System (UVMS). These manipulators are essential especially for underwater intervention missions.

1.2 Underwater vehicle-manipulator system

1.2.1 Autonomous control methods

Since the 1990s, there are very few research studies related to underwater vehicles equipped with manipulators due to various problems [42]. However, a major common problem is the control of the UVMS due to the external disturbances (hydrodynamic effects), kinematic redundancy of UVMS, dynamic coupling forces between the underwater vehicle and manipulators and gravity forces which can affect the trajectory performances of the manipulator's end-tips. The movement or buoyancy created from the motion of the manipulators also can affect the overall vehicle control performance.

To design an effective control system, it is important to design a robust, stable and precise coordinated motions control between the underwater vehicle and manipulators. There are very few studies on control method for coordinated motion control of the vehicle and manipulator. Furthermore, nearly all of these studies utilized numerical simulations to verify the effectiveness of the proposed methods.

Dunnigan et al. [43] focused on dynamic coupling between vehicle and a manipulator with simple hydrodynamic effects by using Slotine's sliding mode to reduce the effect of the hydrodynamics from manipulator movement. Their work determined that the control of the vehicle's yaw angle was the most important factor in reducing the end-tip error variation. Moreover, they concluded that sliding mode control is suited to trajectory tracking applications compared to the fixed-gain PI-speed limited controller. Xu et al. [44] presented a sliding mode controller to control the trajectory of a single-arm UVMS based on the decentralized form of UVMS's dynamics. The study focused on achieving accurate control using low switching gains with only estimating bounds on parameters with hydrodynamic disturbances. Simulations using a five degrees of freedom UVMS were conducted that showed the high performance of trajectory tracking of the UVMS in the presence of uncertainties of vehicle dynamics and hydrodynamic disturbances. There was also a study on a comprehensive scheme for coordinated control of a ROV and a spatial manipulator was developed based on unified dynamic model of the system [45]. In this study,

a novel two-layered sliding mode method containing adjustable PID gains and unknown vector estimator have been proposed. They demonstrated that the proposed method effectively controls UVMS through robust control which is insensitive to inaccuracies in the dynamic model of the UVMS through simulations. However, the stability of the sliding control system is a concerned because usually high gain is chosen in order to achieve system stability. In turn, high gain leads to high frequency chattering effect and excites unmodelled dynamics of UVMS.

It is also important to design a control system for the UVMS which can self-tune itself to adapt to changes in the dynamics of the robot and its surrounding environment which in turn provide a fast responsive performance of manipulator. This method of self-tuning is called adaptive control method. One of the early studies on adaptive control method for UVMS was done by Mahesh et al. [46]. They proposed an adaptive controller for the whole UVMS system by considering both underwater vehicle and manipulator as a single unit. The effectiveness of the controller required a discrete-time approximation of the nonlinear UVMS dynamic and rely on the ability of the controller to adapt to the alternating hydrodynamic coefficients. The performance of the controller has been demonstrated through numerical simulation. The study was followed by Sarkar et al. [47], where a non-regressor based adaptive control is introduced based on bound estimation method for a coordinated motions of a 6-DOF spherical-shaped vehicle with a 3-DOF planar manipulator. The trajectory planning was coordinated and centralized but the control was decentralized and separate for each system (vehicle and manipulator). The developed controller does not require prior knowledge of the system except numbers of joints and actuator inputs of the system. Antonelli et al. [48] proposed a novel adaptive controller based on virtual decomposition of the manipulator's links and the vehicle resulting to a modular structure of controller. The modular structure simplifies the system by reducing the computational burden by using a reduced-order regressor by taking into account thruster dynamics and unknown ocean currents. The effectiveness of the proposed controller was demonstrated through numerical simulations on a 6-DOF underwater vehicle equipped with 6-DOF manipulator. In a more recent study, Mohan and Kim [49] presented an indirect adaptive control method based on extended Kalman Filter (EKF) for a 6-DOF underwater vehicle and a 3-DOF manipulator. Payload and disturbance compensation were used to compensate the reaction effects during manipulation tasks.

There were several researchers that utilized fuzzy controllers for coordination motion control of UVMS. Antonelli and Chiaverini [50] proposed a task priority inverse kinematic approach to redundancy resolution merged with fuzzy controllers to manage coordinated motion of a 6-DOF underwater vehicle equipped with a 6-

DOF manipulator. A fault-tolerant fuzzy-based redundancy resolution method to distribute the human pilot end-effector command over a ROV with a 4-DOF manipulator was proposed in [51]. The fault-tolerant property demonstrated several advantages such as that it can be use to tolerate faulty joints and impose dynamic joint-velocity constraints for better control of the UVMS. Using numerical simulations, they demonstrated that detailed spatial end-effector motions can be completed in real-time through coordination between ROV and manipulator with the fault-tolerant capacity.

In addition the the above studies, several other researchers proposed various control method for UVMS that incorporate hydrodynamic effects into the system. McMillan et al. [52] developed an efficient dynamic simulation based on O(N) algorithm (N is the number of links) for a UUV with a robotic manipulator taking into account of hydrodynamic forces. A dynamic equations for an underwater vehicle with an n-axis robot arm was introduced based on Kane's method by considering external hydrodynamic forces such as added mass, profile drag, fluid acceleration and buoyancy [53]. There was also a unique study on coordinated motions of an underwater vehicle and multiple arms presented in [54]. Mukherjee and Nakamura proposed inverse kinematics and dynamics of an underwater vehicle based on the formulation of of inverse dynamics for space robots in the presence of external generalized forces [55]. Simulation results showed that precise position control of the end-tip of a single main arm was achieved by using two units of stabilizing arms as paddles to counter the forces and moment existed on the shoulder of the main arm, and disturbances acting on the vehicle.

Sarkar and Podder [56] proposed a motion coordination algorithm based on acceleration level kinematic redundancy resolution technique. The proposed method generates the desired trajectories for both vehicle and manipulator that capable to minimize the total hydrodynamic drag acting on the system. The dynamics of the UVMS is included with thruster dynamics and formulated based on the Lagrangian approach. A unified adaptive force control approach incorporating a direct adaptive impedance control method for a 6-DOF underwater vehicle equipped with a 3-DOF robot arm was proposed in [57]. The proposed method merges the adaptive impedance control with hybrid position/force control by means of fuzzy switching to enable autonomous underwater manipulation. Han et al. [58] introduced a performance index for redundancy resolution to generate trajectories for the vehicle and manipulators. The proposed performance index was designed to minimize the vehicle's restoring moments that affect the attitude of the UVMS during manipulation tasks. Based on the simulation results, by optimizing the index using gradient projection method, restoring moments of the UVMS can be reduced without imped-

ing the control performance of the end-effector. Recently, [59] proposed an inverse dynamic control method by assigning separate task for the end-effector and vehicle. The proposed method considered external hydrodynamic effects and thruster dynamics into the control system. State feedback linearization method is used to solve the non-linearities of the UVMS's dynamic.

All of the studies explained above are based on numerical simulation. Only a few number of studies that were able to verify their proposed coordinated motion control methods for UVMS through experimental results using actual vehicle. The following research studies are based on experimental studies using actual UVMS.

One of the most significant studies was done by McLain et al. [60], where they developed a coordinated-control scheme for UVMS and provided the first experimental results to verify the coordinated motion control using an actual underwater vehicle called OTTER mounted with a single-link arm. The experiments demonstrated that hydrodynamic coupling forces between the underwater vehicle and single arm are the major reason in disrupting the stability of the UVMS during manipulation task. They reported that substantial performance improvements can be realized by incorporating model-based information about the hydrodynamic coupling into the control of the system. The model-based approach contains highly accurate model of the arm and vehicle hydrodynamic interaction forces. Based on the experimental results, good station-keeping capability has been achieved and significant reduction of errors and settling times of the end-tip.

Another study that was based on experimental studies was done by Sagara et al. in [30]. In this study, a Resolved Acceleration Control (RAC) method that consider hydrodynamic effect for coordinated motion control of a free-floating underwater robot with a 2-link horizontal planar single manipulator was proposed. The method demonstrated that the end-tip was able to follow the desired trajectory in spite of the influence of hydrodynamic forces towards the UVMS. Then, a continuous-time and discrete-time Resolved Acceleration Control (RAC) methods for an underwater vehicle equipped with a 2-link vertical planar single manipulator have been presented [61]. The proposed digital RAC method was developed by taking into consideration of the singular configuration of the manipulator. From the experimental results, the vehicle and end-tip of the manipulator were able to follow the reference trajectories in spite of the hydrodynamic forces acting on the overall UVMS. Experimental results showed small tracking errors of the manipulator's end-tip in spite of large underwater vehicle motions. The work was further expanded to include a disturbance compensation control method based on the proposed RAC method [62]. The influence of the hydrodynamic force with respect to the vehicle was treated as a disturbance. These are the only experiment-oriented studies that

the authors are aware of.

Basically, in literature related to the design of control system for coordinated motions of underwater vehicle and manipulator, there are many more studies that verified the results through extensive numerical simulations compared to experiment-oriented studies using actual UVMSs. Furthermore, although majority of the control methods considered hydrodynamic effects acting on the UVMSs, nearly all of these studies utilized only a single manipulator except for the work done in [54]. This is easily understood because researchers need to address additional external forces problems related to multiple manipulators such as hydrodynamic forces due to added mass and moment, restoring forces due to gravity and buoyancy and hydrodynamic damping [63]. Therefore, it would be interesting to see how a control method performs with actual underwater vehicle equipped with multiple manipulators.

1.2.2 Master-slave system

Underwater robotic technologies allow humans to execute intervention tasks in an efficient and safe way by reducing the risks fatalities and injuries during underwater operations. Underwater intervention capabilities using robotic arms are necessary to execute tasks such as valve manipulation in oil and gas related operations; conducting science experiments or collection of rocks and marine organisms; and maybe can be deployed for deep-sea search and rescue operation.

In the previous subsection, various autonomous control methods that were specifically designed for coordinated motions of an underwater vehicle and manipulators have been described. However, even with the recent advancement in robotic technologies, the development of fully autonomous underwater manipulation capabilities are still hampered by various common problems such as the precision of control strategies and the ability to avoid unexpected obstacles, and thus limits the ability of the vehicles to underwater survey and monitoring applications only. Due to this reason, human operators are necessary for operating robotic arms because fully autonomous robotic arm manipulation technologies are still far from being perfected.

Apart from autonomous control, another common technique in controlling an underwater robot equipped with manipulators is master-slave system. In this system, a human operator controls the position and attitude of a robot slave in 3-dimensional space from a remote location using a master controller. ROVs are remotely controlled vehicles that implement master-slave system. On the other hand, semi-AUVs is a type of underwater robot that implement master-slave system to an AUV system. The author believe that the control performance of the underwater robot can be improved by maintaining the ability of direct human intervention in an autonomous

robotic system. Thus, semi-AUVs are highly suitable for underwater intervention tasks especially for underwater vehicles attached with multiple robotic arms for object manipulation task.

One of the main component in a master-slave system is the master controller. The master controller is an interface device that sends and possibly receives signals from a control system used, to move a slave robot that includes manipulators [64]. There are various type of master controller such as rate control, position control and force feedback control [40, 65]. Master controllers design based on rate control are commonly utilizing joystick, switches or buttons [66, 67]. On the other hand, position control is usually implemented in the design of manipulator master controllers where it requires the position or angular information of the joints using potentiometers, encoders or servo motors [68]. It utilizes ambidextrous design of master controller, that is a small replica of the manipulator having links and joints similar to the links and joints of the slave manipulator. Position control can also be called unilateral control because when the slave manipulator is exerted by an external force, the master controller will not imitate the motions of the slave manipulator. Force feedback control is similar to position control, except that the master controller will imitate the motions of slave manipulator whenever force is exerted on it (slave manipulator) [29, 69]. Thus, force feedback control can also be known as bilateral control. Usually, the design of the master controllers that has bilateral control utilize actuators inside the joints of the manipulator. There are also master controller designs that have the combination of any type of these controls [70, 71].

Yao et al. [69] utilized an ambidextrous manipulator master controller to control a 6-DOF hydraulically powered manipulator for an underwater vehicle. However, there are no further details about the master controller was developed in-house or off-the-shelf device. Researchers from Korea Ocean Research Development Institute (KORDI) developed a master-slave system for a ROV called HEMIRE consisting of an off-the-shelf master and a worspace-control system to precisely control two ORION manipulators [29]. The off-the-shelf master controller has two units of ambidextrous manipulator master controller to control the two manipulators. The work proposed a workspace-control system that was composed of a computer (for controlling jaw motions and vehicle position and attitude) and a joystick (for controlling end-tips), with the purpose to increase the efficiency manipulation tasks that require precise control of the end-tips such as drilling and coring. In this system, more than a single operator is needed for efficient control of the UVMS. A master controller for a dual-arm UVMS that can be controlled by a single operator was developed and tested in a series of experiments including a field trial in Lake Biwa, Japan [70]. The developed master controller utilized joysticks that control the the position and

attitude motions of the vehicle. The joysticks are mounted on two parallel link mechanisms that work as ambidextrous master manipulator controllers with a total of 10-DOF. Each joint on the links is consisted of pulse encoder for measuring the rotational angle. However, there are no method to determine the amount of commands sent via the joysticks. Thus, the operator needs to rely heavily on the visual provided by the camera system to determine the actual position and attitude of the vehicle.

Soylu et al. [68] utilized a master controller in the form of a parallel architectured 6-DOF joystick to control a small ROV attached with a manipulator. The idea was to unify the UVMS as single redundant manipulator. Thus, the motions of the ROV dependent on the desired end-tip motion using the parallel joystick. A preliminary computer graphical interface was developed to emulate the motion of the robot.

Kawano et al. [71] developed a master-slave system for a 2-link single-arm UVMS. The underwater vehicle's position and attitude motions can be controlled using potentiometers and command-type servo motors, respectively. The 2-link planar slave manipulator can be controlled using an ambidextrous master manipulator controller that utilized command-type servo motors on each joint. An advantage of the design is the operator can easily determine the amount of angles required to control the attitude of the vehicle based on the usage of the command-type servo motors.

A group of researchers from Spain have developed a new approach for semi-autonomous manipulation of unknown objects with underwater robot using laser stripe emitter combined with vision system to reconstruct 3D structure of the location of target objects [72]. Based on the reconstructed 3D structure of the location, a user needs to only indicate the target position for grabbing the target object. Grasping of the target object was done autonomously by the robot. However, the underwater experiments were carried out by assembling the slave manipulator onto a fixed structure, not an actual underwater vehicle that moves. Other works in UVMS studies have utilized video games consoles to control vehicles and arms motions [66, 67].

Most of the studies described above are focusing on developing interface devices for single-arm manipulator applications. Therefore, development of a novel master controller that can control vehicle and multiple robotic arms movement simultaneously is necessary for efficient underwater intervention tasks. Furthermore, the design of the master controller has to be simple and intuitive.

1.3 Problem statements

The motions control of underwater robots are challenging due to many factors. First, underwater robots are not fixed on a stable foundation as the earth-fixed manipulator. Thus, external non-linear forces such as hydrodynamic (buoyant forces and drag forces), moment of inertia and gravity forces applied on the manipulator and the base vehicle can undermine the performance of the system. Moreover, underwater robots equipped with single or more robotic manipulators pose additional complex control problems. Apart from external hydrodynamic forces, each movement of any parts for instance a manipulator, also produce hydrodynamic reaction forces that may effects the other parts and excites each other. Although these reaction forces may have negligible effects on large UVMSs such as [28], [29] and [35], but for small-scaled UVMSs, this may significantly disturbs its system dynamics, especially the control precision of manipulator's end-tip as described in [30] and [60]. Therefore, in order to demonstrate good control performances of the manipulator's end-tip for small UVMSs, the design of control methods are required to not only consider the effect of hydrodynamic forces acting on the vehicle but also the hydrodynamic reaction forces produced by the motions of the manipulator which are challenging.

Next, most of UVMSs control methods are based on methods of AUVs, where the desired accelerations and velocities of manipulator's end-tip are transformed to the desired manipulator's joint accelerations and velocities by using only the kinematic relation [73, 74]. Moreover, computed torque method with joint angle and angular velocity feedbacks are used. Put differently, the computed torque method utilizes errors consisting of manipulator's joint-space signals and vehicle's task-space signals. Due to these reasons, precise position control of the end-tip to follow a pre-defined trajectory is impossible because the control performance of the end-tip depends on the control performance of the vehicle. As a result, if the control performance of the vehicle is not good, it is difficult to have a precise control performance of the end-tip [62]. Thus, control methods that consider coordinated motions between manipulator and the vehicle are very important for precise manipulator's end-tip control.

Furthermore, based on the studies described in the previous section, there are large number of studies related to the design of control method for UVMSs focusing on UVMSs that utilize single manipulator compared to multiple manipulators. Although many control methods described in the previous section demonstrated encouraging results of coordinated motion between vehicle and single manipulator, the studies only verified the effectiveness of the proposed control methods through numerical simulations. As far as this author knows, there are no experiment-oriented

studies that are related to the coordinated motions of underwater vehicle and multiple manipulators. Thus, the lack of verification of control methods for multiple arm UVMS through experimental results in real-world need to be addressed by researchers in the field of UVMSs.

Robotic technologies related to autonomous intervention tasks or object manipulation in underwater environment are still in incubation period. Hence, intervention tasks using master-slave system are still relevant as proved in various real-world events as described in subsection 1.1.1. Although commercially available master-slave systems offer precise and reliable handling of the UVMSs, the cost of the system is a burden especially for educational purposes in higher education institutions. Moreover, although there are companies that have developed master controllers for commercial use, the developed master controllers require more than a single operator to control both manipulators and vehicle at the same time. As far as the author's knowledge, there are no research-based or even commercially available master controller that enables a single operator to operate a vehicle and multiple manipulators simultaneously.

1.4 Objectives of the study

The objectives of the research are described below:

1. To propose a RAC method for multi-link multi-manipulators UVMSs that consider the effects of external hydrodynamic forces and vehicle/arm interaction forces based on work done in [62].

2. To develop a RAC method based on the proposed RAC method for multi-link multi-arm UVMSs for coordinated motion control of
   (a) a fully AUV and 2-link dual-arm,
   (b) a fully AUV and 3-link dual-arm.

3. To verify and demonstrate through experimental results regarding the effectiveness of the proposed RAC method for coordinated motion control of
   (a) a fully AUV and 2-link dual-arm,
   (b) a fully AUV and 3-link dual-arm.

4. To develop a novel master controller for a master-slave system that is capable of controlling a semi-AUV and 3-link dual-arm simultaneously. The term semi-AUV is being used in this work to describe that the control of the motions for the AUV is supported by an autonomous control system using direct human operator's input from the developed master controller. Whereas the robotic

arms are directly controlled by the operator without the assist of autonomous control.

5. To demonstrate the effectiveness of the developed master controller by controlling the semi-AUV to catch a target object in actual underwater experiment.

1.5 Outline of research

The dissertation is organized as follows:

Chapter 2 describes a Resolved Acceleration Control (RAC) method for multi-link and multi-arm underwater vehicle-manipulator system (UVMS). A model of a multi-link multi-arm UVMS is presented. Based on this model, the kinematic equation for the UVMS is described. In addition, the momentum equation consisting of linear and rotational momentum of the UVMS considering hydrodynamic added mass and added inertia moment acting on the UVMS is explained. Hydrodynamic drag forces, drag moment and buoyant forces acting on the UVMS are derived. Then, the dynamic equation to obtain the desired motion of the UVMS is described. At the end of the chapter, the detail explanation about the proposed RAC method for a precise control of manipulator's end-tips is introduced.

In Chapter 3, as a first step to demonstrate the effectiveness of the proposed method described in Chapter 2, a RAC method for a 2-link planar dual-arm UVMS is developed based on the proposed RAC method described in Chapter 2. An experimental system containing an actual fully-AUV equipped with 2-link planar dual-arm that can move in 2-dimensional space is explained. The detail structure and circuitry design of the 2-link planar arm that utilizes servo magnetic coupling mechanism in the joint design is described. Finally, the main objective of this chapter which is to show the effectiveness of the proposed method through experimental results are presented and discussed in detail. To date, this is the first study that verify the effectiveness of a control method for multiple arm UVMS through experiment.

Chapter 4 presents the experimental results that further demonstrate the effectiveness of the RAC method to control the positions of the end-tips in 3-dimensional space. Since a 2-link planar dual-arm UVMS is utilized in the experiment in Chapter 3, the proposed RAC method can only control the end-tips in a 2-dimensional space only. In this chapter, two units of newly developed 3-link arm for UVMS that can move in 3-dimensional space are developed and presented. Furthermore, a RAC method for a 3-link dual-arm UVMS is proposed. Then, experimental results showing the effectiveness and usefulness of the proposed RAC method in controlling the positions of both arm's end-tips in 3-dimensional space are reported and discussed.

In Chapter 5, a simple and intuitive master controller for controlling an experimental semi-AUV equipped with 3-link dual-arm is introduced. As explained in the previous section, there are no research-based or even commercially available master controller that enables a single operator to operate a vehicle and multiple manipulators simultaneously. Therefore, in this chapter, a master controller that enables a single operator to operate a vehicle and multiple manipulators simultaneously is presented. The detail designs of the master controller which include a vehicle main master controller and two units of 3-link manipulator master controller are described. Moreover, the developed master controller also consists of two units of vehicle sub-master controller that allow the operator to simultaneously control two units of 3-link dual-arm and the position and attitude of the vehicle. At the end of this chapter, experimental results on controlling an actual dual-arm underwater robot to catch a target object in underwater environment using the proposed master controller are presented and discussed.

Chapter 6 summarized the whole dissertation and describes recommendations for future research.

Chapter 2

Resolved acceleration control (RAC) method for underwater vehicle-manipulator systems

2.1 Introduction

In this chapter, a Resolved Acceleration Control (RAC) method for multi-link and multi-arm underwater vehicle-manipulator system (UVMS) is proposed. Using the RAC method, a coordinated motion control of an underwater vehicle and manipulator's end-tips can be achieved. First, the mathematical model of a UVMS is introduced. Next, the kinematic equation for the UVMS expressed by the relationship between the linear and angular velocity of the arm's end-tips with the linear and angular velocity of the vehicle and angular velocity of arm's joints is described. In addition, the momentum equation consisting of linear and rotational momentum of the UVMS considering hydrodynamic added mass and added inertia moment acting on the UVMS is presented. Then, the dynamic equation to obtain the desired motion of the UVMS is described. At the end of the chapter, the detail explanation about the proposed RAC method is introduced.

2.2 Modeling of a UVMS

Fig. 2.1 shows the three-dimensional model of a floating underwater vehicle equipped with multi-link dual-arm that is considered in this work.

The model is consists of an inertial coordinate frame Σ_I and vehicle coordinate frame Σ_0. Here, Σ_I is introduced to describe the motion of the entire UVMS system. The vehicle (robot base) is denoted as link 0. The links of the dual-arm are assigned

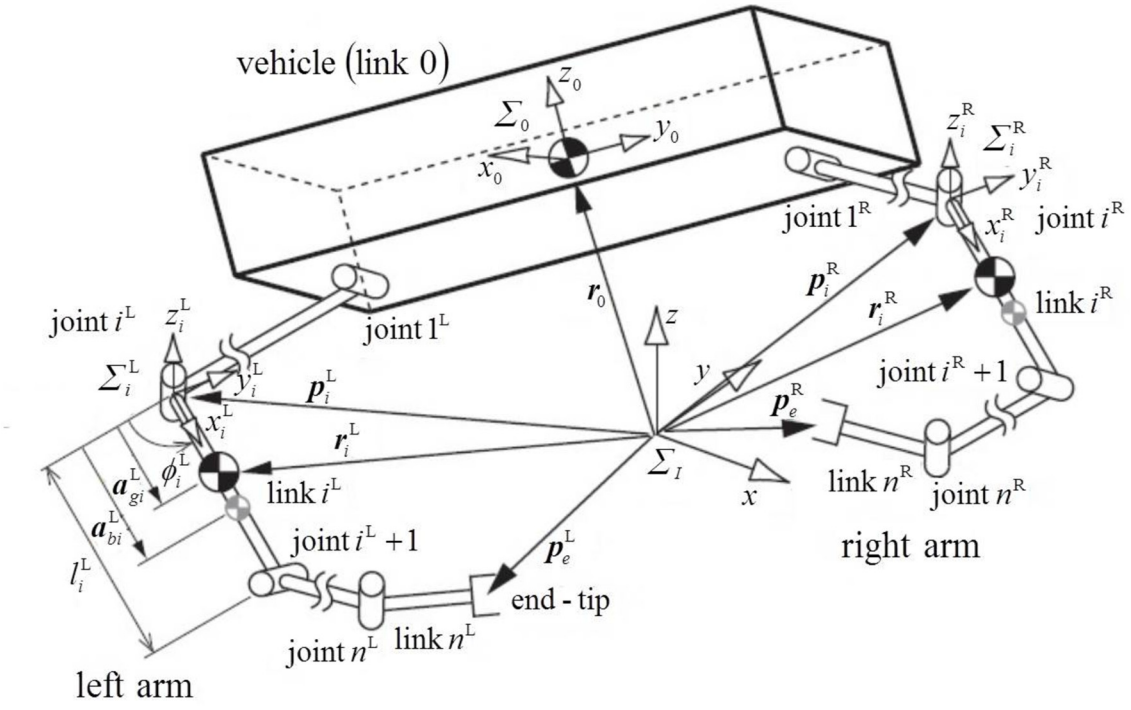

Fig. 2.1: Model of underwater robot equipped with multiple-links dual-arm

with numbers consecutively, starting from the base. Each links of the right arm is numbered from 1 to n. Similarly, each links of the left arm is numbered from 1 to n. The joint between link i and link $(i+1)$ is denoted as joint i. Therefore, the parameters related to both right and left arm can be expressed such as n^*, where $*$ symbol is fixed on the upper right.

In describing the mathematical model of the UVMS, three important assumptions were made:

- The structure of the robot is a collection of rigid bodies connected by joints.
- Although the forces of gravity (weight) and forces of buoyancy of the robot base and each link are not coincide, the whole system of the robot is in the state of equilibrium.
- The surrounding fluid is in a static condition.

Symbols used in the model are defined as follows:

i^* : number of joint and link for arm $*$ ($*$=R: Right arm, $*$=L: Left arm)
n^* : number of joint for arm $*$ ($*$=R: Right arm, $*$=L: Left arm)
Σ_I : inertial coordinate frame
Σ_0 : robot base (vehicle) coordinate frame

Σ_i^* : link i coordinate frame for arm $*$ ($*$=R: Right arm, $*$=L: Left arm)

${}^i\boldsymbol{R}_j^*$: coordinate transformation matrix of arm $*$ from Σ_j^* to Σ_i^*

$\boldsymbol{r}_0$: position vector of center of gravity for robot base with respect to Σ_I

$\boldsymbol{p}_e^*$: position vector of end-tip of arm $*$ with respect to Σ_I

$\boldsymbol{p}_i^*$: position vector of origin of Σ_i^* with respect to Σ_I

$\boldsymbol{r}_i^*$: position vector of center of gravity for link i^* with respect to Σ_I

$\boldsymbol{\psi}_0$: roll-pitch-yaw attitude vector of Σ_0 with respect to Σ_I

$\boldsymbol{\psi}_e^*$: roll-pitch-yaw attitude vector of end-tip for arm $*$ with respect to Σ_I

$\boldsymbol{\omega}_0$: angular velocity vector of Σ_0 with respect to Σ_I

$\boldsymbol{\omega}_i^*$: angular velocity vector of Σ_i^* with respect to Σ_I

$\boldsymbol{\omega}_e^*$: angular velocity vector of end-tip for arm $*$ with respect to Σ_I

ϕ_i^* : relative angle of joint i^*

$\boldsymbol{\phi}$: relative joint angle vector ($= [(\boldsymbol{\phi}^{\mathrm{R}})^T,\ (\boldsymbol{\phi}^{\mathrm{L}})^T]^T$), ($\boldsymbol{\phi}^* = [\phi_1^*, \phi_2^*,\ \cdots,\ \phi_{n^*}^*]^T$)

$\boldsymbol{k}_i^*$: unit vector indicating a rotational axis of joint i^*

m_0 : mass of robot base

m_i^* : mass of link i^*

$\boldsymbol{M}_{a_i}^*$: added mass matrix of link i^* with respect to Σ_i^*

$\boldsymbol{I}_i^*$: inertia tensor of link i^* with respect to Σ_i^*

$\boldsymbol{I}_{a_i}^*$: added inertia tensor of link i^* with respect to Σ_i^*

$\boldsymbol{x}_0$: position and attitude vector of Σ_0 with respect to Σ_I ($= [\boldsymbol{r}_0^T,\ \boldsymbol{\psi}_0^T]^T$)

$\boldsymbol{x}_e^*$: position and attitude vector of end tip for arm $*$ with respect to $*$ Σ_I ($= [(\boldsymbol{p}_e^*)^T,\ (\boldsymbol{\psi}_e^*)^T]^T$)

$\boldsymbol{\nu}_0$: linear and angular velocity vector of Σ_0 with respect to Σ_I ($= [\dot{\boldsymbol{r}}_0^T,\ \boldsymbol{\omega}_0^T]^T$)

$\boldsymbol{\nu}_e^*$: linear and angular velocity vector of end-tip for arm $*$ with respect to Σ_I ($= [(\dot{\boldsymbol{p}}_e^*)^T,\ (\boldsymbol{\omega}_e^*)^T]^T$)

l_i^* : length of link i^*

$a_{g_i}^*$: length between joint i^* to the center of gravity of link i^*

$a_{b_i}^*$: length between joint i^* to the center of buoyancy of link i^*

${}^i\boldsymbol{l}_i^*$: position vector of joint ($i^* + 1$) with respect to Σ_i

$\boldsymbol{a}_{g_i}^*$: position vector from joint i^* to the center of gravity of link i^* with respect to Σ_I

$\boldsymbol{a}_{b_i}^*$: position vector from joint i^* to the center of buoyancy of link i^* with respect to Σ_I

D_i^* : width of link i^*

V_i^* : volume of link i^*

ρ : fluid density

$C_{d_i}^*$: drag force coefficient for link i^*

$\boldsymbol{g}$: gravitational acceleration vector

$\boldsymbol{E}_j$: $j \times j$ unit matrix

$\tilde{\cdot}$: tilde operator stands for a cross product such that $\tilde{\boldsymbol{r}}\boldsymbol{a} = \boldsymbol{r} \times \boldsymbol{a}$

In the field of underwater robotics, when an object moves in a fluid, external hydrodynamic forces comprises of in-line and transverse forces (generated from shedding of vortices) are taken into consideration [75]. However, the motions permitted for underwater robots are usually very slow and the magnitude of the transverse forces are relatively small compared to the in-line forces [75, 76]. Thus, only in-line forces containing drag, added mass and fluid-acceleration forces are usually affecting the motions of a slow moving underwater robot. In [75], accurate modeling of added mass and drag forces can be achieved by state-dependent coefficients. However, in general, added mass are identified experimentally using added mass of a simplified shape as the initial value [77]. Thus, the added mass, added moment of inertia and drag coefficient are based on constant values that depends on the shape of the robots that is usually called strip theory [73, 76, 78]. Therefore, in this work, the hydrodynamic forces is obtained by applying the same principle.

2.2.1 Kinematic equation

In order to derive the kinematic and momentum equations, the center of mass for the robot base and arm links, and angular velocities of the arm joints are determined.

First, the position vector $\boldsymbol{p}_i^*$ of each joint i^* ($i^* = 1,\ 2,\ \cdots,\ n^*$) for both arms, and the position vector $\boldsymbol{r}_i^*$ of the center of mass for each link i^* can be described as

$$\boldsymbol{p}_i^* = \boldsymbol{p}_{i-1}^* + {}^I\boldsymbol{R}_{i-1}^{*\ i-1}\boldsymbol{l}_{i-1}^*, \tag{2.1}$$

$$\boldsymbol{r}_i^* = \boldsymbol{p}_i^* + {}^I\boldsymbol{R}_i^{*i}\boldsymbol{a}_{g_i}^*, \tag{2.2}$$

where ${}^i\boldsymbol{l}_i^* = [l_i^*,\ 0,\ 0]^T$ and Σ_i^*, ${}^i\boldsymbol{a}_{g_i}^* = [a_i^*,\ 0,\ 0]^T$ are the position vectors with respect to Σ_i^*. Note that $\boldsymbol{p}_0 = \boldsymbol{r}_0$. Similarly, the position $\boldsymbol{p}_e^*$ of each end-tip for both arms is

$$\boldsymbol{p}_e^* = \boldsymbol{p}_{n^*}^* + {}^I\boldsymbol{R}_{n^*}^{*\ n^*}\boldsymbol{l}_{n^*}^*. \tag{2.3}$$

Next, the linear velocity vector and angular velocity vector for joint i^* can be described as

$$\dot{\boldsymbol{p}}_i^* = \dot{\boldsymbol{p}}_{i-1}^* + \boldsymbol{\omega}_{i-1}^* \times ({}^I\boldsymbol{R}_{i-1}^{*\ i-1}\boldsymbol{l}_{i-1}^*), \tag{2.4}$$

$$\boldsymbol{\omega}_i^* = \boldsymbol{\omega}_{i-1}^* + {}^I\boldsymbol{R}_i^{*i}\boldsymbol{k}_i^*\dot{\phi}_i^*. \tag{2.5}$$

Similarly, the linear velocity vector for the center of mass for link i^* and each end-tip are

$$\dot{\boldsymbol{r}}_i^* = \dot{\boldsymbol{p}}_i^* + \boldsymbol{\omega}_i^* \times ({}^I\boldsymbol{R}_i^{*i}\boldsymbol{a}_{g_i}^*), \tag{2.6}$$

$$\dot{\boldsymbol{p}}_e^* = \dot{\boldsymbol{p}}_{n^*}^* + \boldsymbol{\omega}_{n^*}^* \times ({}^I\boldsymbol{R}_{n^*}^{*\,n^*}\boldsymbol{l}_{n^*}^*). \tag{2.7}$$

Here,

$${}^I\boldsymbol{R}_{i-1}^{*\,i-1}\boldsymbol{l}_{i-1}^* = \boldsymbol{p}_i^* - \boldsymbol{p}_{i-1}^*,$$

$${}^I\boldsymbol{R}_i^{*i}\boldsymbol{a}_{g_i}^* = \boldsymbol{r}_i^* - \boldsymbol{p}_i^*,$$

and $\boldsymbol{k}_i^*$ is defined as

$$\boldsymbol{k}_i^* = {}^I\boldsymbol{R}_i^{*i}\boldsymbol{k}_i^*.$$

As a result, the linear velocity and angular velocity for joint i^* based on Equations (2.4) and (2.5) are expressed as

$$\begin{aligned}\dot{\boldsymbol{p}}_i^* &= \dot{\boldsymbol{p}}_{i-1}^* + \tilde{\boldsymbol{\omega}}_{i-1}^*(\boldsymbol{p}_i^* - \boldsymbol{p}_{i-1}^*) \\ &= \dot{\boldsymbol{r}}_0 - (\tilde{\boldsymbol{p}}_i^* - \tilde{\boldsymbol{r}}_0)\boldsymbol{\omega}_0 + \sum_{j=1}^{i-1}\tilde{\boldsymbol{k}}_j^*(\boldsymbol{p}_i^* - \boldsymbol{p}_j^*)\dot{\phi}_j^*,\end{aligned} \tag{2.8}$$

$$\boldsymbol{\omega}_i^* = \boldsymbol{\omega}_0 + \sum_{j=1}^{i}\boldsymbol{k}_j^*\dot{\phi}_j^*. \tag{2.9}$$

In a similar manner, the linear velocity and angular velocity for the center of mass for link i^* and both end-tips based on Equation (2.7) become

$$\dot{\boldsymbol{r}}_i = \dot{\boldsymbol{r}}_0 - (\tilde{\boldsymbol{r}}_i^* - \tilde{\boldsymbol{r}}_0)\boldsymbol{\omega}_0 + \sum_{j=1}^{i}\tilde{\boldsymbol{k}}_j^*(\boldsymbol{r}_i^* - \boldsymbol{p}_j^*)\dot{\phi}_j^*, \tag{2.10}$$

$$\dot{\boldsymbol{p}}_e^* = \dot{\boldsymbol{r}}_0 - (\tilde{\boldsymbol{p}}_e^* - \tilde{\boldsymbol{r}}_0)\boldsymbol{\omega}_0 + \sum_{j=1}^{n^*}\tilde{\boldsymbol{k}}_j^*(\boldsymbol{p}_e^* - \boldsymbol{p}_j^*)\dot{\phi}_j^*, \tag{2.11}$$

and,

$$\boldsymbol{\omega}_e^* = \boldsymbol{\omega}_0 + \sum_{j=1}^{n^*}\boldsymbol{k}_j^*\dot{\phi}_j^*. \tag{2.12}$$

The kinematic and momentum equations can be determined based on the aforementioned equations.

First, based on Equations (2.11) and (2.12), the relationship between the linear and angular velocity vector for both end-tips $\boldsymbol{\nu}_e^* = [(\dot{\boldsymbol{p}}_e^*)^T,\ (\boldsymbol{\omega}_e^*)^T]^T$, the linear and angular velocity vector of robot base $\boldsymbol{\nu}_0 = [\dot{\boldsymbol{r}}_0^T,\ \boldsymbol{\omega}_0^T]^T$ and angular velocity vector of each joint for both arms $\dot{\boldsymbol{\phi}}^* = [\dot{\phi}_1^*, \dot{\phi}_2^*,\ \cdots,\ \dot{\phi}_{n^*}^*]^T$ can be expressed with

$$\boldsymbol{\nu}_e^* = \boldsymbol{A}^*\boldsymbol{\nu}_0 + \boldsymbol{B}^*\dot{\boldsymbol{\phi}}^* \qquad (* = \mathrm{R}, \mathrm{L}), \tag{2.13}$$

where

$$\boldsymbol{A}^* = \begin{bmatrix} \boldsymbol{E}_3 & -(\tilde{\boldsymbol{p}}_e^* - \tilde{\boldsymbol{r}}_0) \\ \boldsymbol{0} & \boldsymbol{E}_3 \end{bmatrix},$$
$$\boldsymbol{B}^* = \begin{bmatrix} \boldsymbol{b}_1^* & \boldsymbol{b}_2^* & \cdots & \boldsymbol{b}_n^* \end{bmatrix},$$
$$\boldsymbol{b}_i^* = [\{\tilde{\boldsymbol{k}}_i^*(\boldsymbol{p}_e^* - \boldsymbol{p}_i^*)\}^T,\ (\boldsymbol{k}_i^*)^T]^T.$$

Moreover, based on Equation (2.13), linear and angular velocity vector for both end-tips $\boldsymbol{\nu}_e = [(\boldsymbol{\nu}_e^{\mathrm{R}})^T,\ (\boldsymbol{\nu}_e^{\mathrm{L}})^T]^T$, linear and angular velocity vector for robot base $\boldsymbol{\nu}_0 = [\dot{\boldsymbol{r}}_0^T,\ \boldsymbol{\omega}_0^T]^T$ and angular velocity of each joint on both arms $\dot{\boldsymbol{\phi}} = [(\dot{\boldsymbol{\phi}}^{\mathrm{R}})^T,\ (\dot{\boldsymbol{\phi}}^{\mathrm{L}})^T]^T$ can be summarized into a single kinematic equation as

$$\boldsymbol{\nu}_e = \boldsymbol{A}\boldsymbol{\nu}_0 + \boldsymbol{B}\dot{\boldsymbol{\phi}}, \tag{2.14}$$

where

$$\boldsymbol{A} = \begin{bmatrix} \boldsymbol{A}^{\mathrm{R}} \\ \boldsymbol{A}^{\mathrm{L}} \end{bmatrix},$$
$$\boldsymbol{B} = \begin{bmatrix} \boldsymbol{B}^{\mathrm{R}} & \boldsymbol{0} \\ \boldsymbol{0} & \boldsymbol{B}^{\mathrm{L}} \end{bmatrix}.$$

2.2.2 Momentum equation

In this section, the linear momentum of the robot overall system $\boldsymbol{\eta}$ and angular momentum around the center of mass of the robot base $\boldsymbol{\mu}$ containing hydrodynamic added mass ${}^{i}\boldsymbol{M}_{a_i}^{*}$ and added inertia moment ${}^{i}\boldsymbol{I}_{a_i}^{*}$ are determined. Here, the linear momentum of the robot overall system $\boldsymbol{\eta}$ is considered to consist of linear momentum of the robot base $\boldsymbol{\eta}_0$, linear momentum of the right arm $\boldsymbol{\eta}^{\mathrm{R}}$ and linear momentum of the left arm $\boldsymbol{\eta}^{\mathrm{L}}$. Similarly, the angular momentum around the center of mass of the robot base $\boldsymbol{\mu}$ is also considered to consist of angular momentum of the robot base $\boldsymbol{\mu}_0$, angular momentum of right arm $\boldsymbol{\mu}^{\mathrm{R}}$ and angular momentum of left arm $\boldsymbol{\mu}^{\mathrm{L}}$.

Therefore, linear momentum $\boldsymbol{\eta}$ and angular momentum $\boldsymbol{\mu}$ are expressed as

$$\begin{aligned}\boldsymbol{\eta} &= \boldsymbol{\eta}_0 + \boldsymbol{\eta}^{\mathrm{R}} + \boldsymbol{\eta}^{\mathrm{L}} \\ &= \boldsymbol{M}_{T_0}\,\dot{\boldsymbol{r}}_0 + \boldsymbol{\eta}^{\mathrm{R}} + \boldsymbol{\eta}^{\mathrm{L}},\end{aligned} \tag{2.15}$$

$$\begin{aligned}\boldsymbol{\mu} &= \boldsymbol{\mu}_0 + \boldsymbol{\mu}^{\mathrm{R}} + \boldsymbol{\mu}^{\mathrm{L}} - \boldsymbol{r}_0 \times \boldsymbol{\eta} \\ &= \boldsymbol{I}_{T_0}\,\boldsymbol{\omega}_0 + \boldsymbol{r}_0 \times \boldsymbol{M}_{T_0}\dot{\boldsymbol{r}}_0 + \boldsymbol{\mu}^{\mathrm{R}} + \boldsymbol{\mu}^{\mathrm{L}} - \boldsymbol{r}_0 \times \boldsymbol{\eta},\end{aligned} \tag{2.16}$$

where

$$\begin{aligned}\boldsymbol{\eta}^{*} &= \sum_{i=1}^{n^{*}} \boldsymbol{M}_{T_i}^{*}\dot{\boldsymbol{r}}_i^{*}, \\ \boldsymbol{\mu}^{*} &= \sum_{i=1}^{n^{*}} \boldsymbol{I}_{T_i}^{*}\boldsymbol{\omega}_i^{*} + \tilde{\boldsymbol{r}}_i^{*}\boldsymbol{M}_{T_i}^{*}\dot{\boldsymbol{r}}_i^{*}, \\ \boldsymbol{M}_{T_0} &= m_0\boldsymbol{E}_3 + {}^{I}\boldsymbol{R}_0\,{}^{0}\boldsymbol{M}_{a_0}\,{}^{0}\boldsymbol{R}_I, \\ \boldsymbol{I}_{T_0} &= {}^{I}\boldsymbol{R}_0({}^{0}\boldsymbol{I}_0 + {}^{0}\boldsymbol{I}_{a_0})^{0}\boldsymbol{R}_I, \\ \boldsymbol{M}_{T_i}^{*} &= m_i^{*}\boldsymbol{E}_3 + {}^{I}\boldsymbol{R}_i^{*\,i}\boldsymbol{M}_{a_i}^{*}\,{}^{i}\boldsymbol{R}_I^{*}, \\ \boldsymbol{I}_{T_i}^{*} &= {}^{I}\boldsymbol{R}_i^{*}({}^{i}\boldsymbol{I}_i^{*} + {}^{i}\boldsymbol{I}_{a_i}^{*})^{i}\boldsymbol{R}_I^{*}.\end{aligned}$$

Consequently, by applying Equations (2.9) and (2.10) into Equations (2.15) and (2.16), linear velocity of robot base $\dot{\boldsymbol{r}}_0$, angular velocity of robot base $\boldsymbol{\omega}_0$ and angular velocity for the arm joint $\dot{\boldsymbol{\phi}}_i^{*}$ can be summarized into linear momentum $\boldsymbol{\eta}$ and angular

momentum $\boldsymbol{\mu}$ that can be described as

$$
\begin{aligned}
\boldsymbol{\eta} &= \boldsymbol{M}_{T_0}\dot{\boldsymbol{r}}_0 + \sum_{i=1}^{n^{\mathrm{R}}} \boldsymbol{M}_{T_i}^{\mathrm{R}}\dot{\boldsymbol{r}}_i^{\mathrm{R}} + \sum_{i=1}^{n^{\mathrm{L}}} \boldsymbol{M}_{T_i}^{\mathrm{L}}\dot{\boldsymbol{r}}_i^{\mathrm{L}} \\
&= \boldsymbol{M}_{T_0}\dot{\boldsymbol{r}}_0 + \boldsymbol{M}_{T_i}^{\mathrm{R}} \left\{ \dot{\boldsymbol{r}}_0 - (\tilde{\boldsymbol{r}}_i^{\mathrm{R}} - \tilde{\boldsymbol{r}}_0)\boldsymbol{\omega}_0 + \sum_{j=1}^{i} \tilde{\boldsymbol{k}}_j^{\mathrm{R}}(\boldsymbol{r}_i^{\mathrm{R}} - \boldsymbol{p}_j^{\mathrm{R}})\dot{\phi}_j^{\mathrm{R}} \right\} \\
&\quad + \boldsymbol{M}_{T_i}^{\mathrm{L}} \left\{ \dot{\boldsymbol{r}}_0 - (\tilde{\boldsymbol{r}}_i^{\mathrm{L}} - \tilde{\boldsymbol{r}}_0)\boldsymbol{\omega}_0 + \sum_{j=1}^{i} \tilde{\boldsymbol{k}}_j^{\mathrm{L}}(\boldsymbol{r}_i^{\mathrm{L}} - \boldsymbol{p}_j^{\mathrm{L}})\dot{\phi}_j^{\mathrm{L}} \right\} \\
&= \left\{ \boldsymbol{M}_{T_0} + \sum_{i=1}^{n^{\mathrm{R}}} \boldsymbol{M}_{T_i}^{\mathrm{R}} + \sum_{i=1}^{n^{\mathrm{L}}} \boldsymbol{M}_{T_i}^{\mathrm{L}} \right\} \dot{\boldsymbol{r}}_0 \\
&\quad - \left\{ \sum_{i=1}^{n^{\mathrm{R}}} \boldsymbol{M}_{T_i}^{\mathrm{R}}(\tilde{\boldsymbol{r}}_i^{\mathrm{R}} - \tilde{\boldsymbol{r}}_0) - \sum_{i=1}^{n^{\mathrm{L}}} \boldsymbol{M}_{T_i}^{\mathrm{L}}(\tilde{\boldsymbol{r}}_i^{\mathrm{L}} - \tilde{\boldsymbol{r}}_0) \right\} \boldsymbol{\omega}_0 \\
&\quad + \sum_{i=1}^{n^{\mathrm{R}}} \sum_{j=i}^{n^{\mathrm{R}}} \boldsymbol{M}_{T_i}^{*} \tilde{\boldsymbol{k}}_i^{\mathrm{R}}(\boldsymbol{r}_j^{\mathrm{R}} - \boldsymbol{p}_i^{\mathrm{R}})\dot{\phi}_i^{\mathrm{R}} + \sum_{i=1}^{n^{\mathrm{L}}} \sum_{j=i}^{n^{\mathrm{L}}} \boldsymbol{M}_{T_i}^{*} \tilde{\boldsymbol{k}}_i^{\mathrm{L}}(\boldsymbol{r}_j^{\mathrm{L}} - \boldsymbol{p}_i^{\mathrm{L}})\dot{\phi}_i^{\mathrm{L}},
\end{aligned} \tag{2.17}
$$

$$
\begin{aligned}
\boldsymbol{\mu} &= \boldsymbol{I}_{T_0}\boldsymbol{\omega}_0 + \boldsymbol{r}_0 \times \boldsymbol{M}_{T_0}\dot{\boldsymbol{r}}_0 + \sum_{i=1}^{n^{\mathrm{R}}} \left(\boldsymbol{I}_{T_i}^{\mathrm{R}}\boldsymbol{\omega}_i^{\mathrm{R}} + \tilde{\boldsymbol{r}}_i^{\mathrm{R}}\boldsymbol{M}_{T_i}^{\mathrm{R}}\dot{\boldsymbol{r}}_i^{\mathrm{R}} \right) + \sum_{i=1}^{n^{\mathrm{L}}} \left(\boldsymbol{I}_{T_i}^{\mathrm{L}}\boldsymbol{\omega}_i^{\mathrm{L}} + \tilde{\boldsymbol{r}}_i^{\mathrm{L}}\boldsymbol{M}_{T_i}^{\mathrm{L}}\dot{\boldsymbol{r}}_i^{\mathrm{L}} \right) \\
&\quad - \boldsymbol{r}_0 \times \left\{ \boldsymbol{M}_{T_0}\dot{\boldsymbol{r}}_0 + \sum_{i=1}^{n^{\mathrm{R}}} \boldsymbol{M}_{T_i}^{\mathrm{R}}\dot{\boldsymbol{r}}_i^{\mathrm{R}} + \sum_{i=1}^{n^{\mathrm{L}}} \boldsymbol{M}_{T_i}^{\mathrm{L}}\dot{\boldsymbol{r}}_i^{\mathrm{L}} \right\} \\
&= \boldsymbol{I}_{T_0}\boldsymbol{\omega}_0 + \sum_{i=1}^{n^{\mathrm{R}}} \left\{ \boldsymbol{I}_{T_i}^{\mathrm{R}}\boldsymbol{\omega}_i^{\mathrm{R}} + (\tilde{\boldsymbol{r}}_i^{\mathrm{R}} - \tilde{\boldsymbol{r}}_0)\boldsymbol{M}_{T_i}^{\mathrm{R}}\dot{\boldsymbol{r}}_i^{\mathrm{R}} \right\} + \sum_{i=1}^{n^{\mathrm{L}}} \left\{ \boldsymbol{I}_{T_i}^{\mathrm{L}}\boldsymbol{\omega}_i^{\mathrm{L}} + (\tilde{\boldsymbol{r}}_i^{\mathrm{L}} - \tilde{\boldsymbol{r}}_0)\boldsymbol{M}_{T_i}^{\mathrm{L}}\dot{\boldsymbol{r}}_i^{\mathrm{L}} \right\} \\
&= \left\{ \sum_{i=1}^{n^{\mathrm{R}}} (\tilde{\boldsymbol{r}}_i^{\mathrm{R}} - \tilde{\boldsymbol{r}}_0)\boldsymbol{M}_{T_i}^{\mathrm{R}} + \sum_{i=1}^{n^{\mathrm{L}}} (\tilde{\boldsymbol{r}}_i^{\mathrm{L}} - \tilde{\boldsymbol{r}}_0)\boldsymbol{M}_{T_i}^{\mathrm{L}} \right\} \dot{\boldsymbol{r}}_0 \\
&\quad + \left\{ \boldsymbol{I}_{T_0} + \sum_{i=1}^{n^{\mathrm{R}}} \left\{ \boldsymbol{I}_{T_i}^{\mathrm{R}} - (\tilde{\boldsymbol{r}}_i^{\mathrm{R}} - \tilde{\boldsymbol{r}}_0)\boldsymbol{M}_{T_i}^{\mathrm{R}}(\tilde{\boldsymbol{r}}_i^{\mathrm{R}} - \tilde{\boldsymbol{r}}_0) \right\} + \sum_{i=1}^{n^{\mathrm{L}}} \left\{ \boldsymbol{I}_{T_i}^{\mathrm{L}} - (\tilde{\boldsymbol{r}}_i^{\mathrm{L}} - \tilde{\boldsymbol{r}}_0)\boldsymbol{M}_{T_i}^{\mathrm{L}}(\tilde{\boldsymbol{r}}_i^{\mathrm{L}} - \tilde{\boldsymbol{r}}_0) \right\} \right\} \boldsymbol{\omega}_0 \\
&\quad + \sum_{i=1}^{n^{\mathrm{R}}} \sum_{j=i}^{n^{\mathrm{R}}} \left\{ \boldsymbol{I}_{T_j}^{\mathrm{R}} - (\tilde{\boldsymbol{r}}_j^{\mathrm{R}} - \tilde{\boldsymbol{r}}_0)\boldsymbol{M}_{T_j}^{\mathrm{R}}(\tilde{\boldsymbol{r}}_j^{\mathrm{R}} - \tilde{\boldsymbol{p}}_i^{\mathrm{R}}) \right\} \boldsymbol{k}_i^{\mathrm{R}}\dot{\phi}_i^{\mathrm{R}} \\
&\quad + \sum_{i=1}^{n^{\mathrm{L}}} \sum_{j=i}^{n^{\mathrm{L}}} \left\{ \boldsymbol{I}_{T_j}^{\mathrm{L}} - (\tilde{\boldsymbol{r}}_j^{\mathrm{L}} - \tilde{\boldsymbol{r}}_0)\boldsymbol{M}_{T_j}^{\mathrm{L}}(\tilde{\boldsymbol{r}}_j^{\mathrm{L}} - \tilde{\boldsymbol{p}}_i^{\mathrm{L}}) \right\} \boldsymbol{k}_i^{\mathrm{L}}\dot{\phi}_i^{\mathrm{L}}.
\end{aligned} \tag{2.18}
$$

Thus, based on Equations (2.17) and (2.18), the following momentum equation can be obtained:

$$\boldsymbol{s} = \begin{bmatrix} \boldsymbol{\eta} \\ \boldsymbol{\mu} \end{bmatrix} = \boldsymbol{C}\boldsymbol{\nu}_0 + \boldsymbol{D}\dot{\boldsymbol{\phi}}, \tag{2.19}$$

where

$$\boldsymbol{C} = \begin{bmatrix} \boldsymbol{c}_{11} & \boldsymbol{c}_{12} \\ \boldsymbol{c}_{21} & \boldsymbol{c}_{22} \end{bmatrix},$$

$$\boldsymbol{D} = \begin{bmatrix} \boldsymbol{d}_{11}^{\mathrm{R}} & \boldsymbol{d}_{12}^{\mathrm{R}} & \cdots & \boldsymbol{d}_{1n^{\mathrm{R}}}^{\mathrm{R}} & \boldsymbol{d}_{11}^{\mathrm{L}} & \boldsymbol{d}_{12}^{\mathrm{L}} & \cdots & \boldsymbol{d}_{1n^{\mathrm{L}}}^{\mathrm{L}} \\ \boldsymbol{d}_{21}^{\mathrm{R}} & \boldsymbol{d}_{22}^{\mathrm{R}} & \cdots & \boldsymbol{d}_{2n^{\mathrm{R}}}^{\mathrm{R}} & \boldsymbol{d}_{21}^{\mathrm{L}} & \boldsymbol{d}_{22}^{\mathrm{L}} & \cdots & \boldsymbol{d}_{2n^{\mathrm{L}}}^{\mathrm{L}} \end{bmatrix},$$

$$\boldsymbol{c}_{11} = \boldsymbol{M}_{T_0} + \sum_{i=1}^{n^{\mathrm{R}}} \boldsymbol{M}_{T_i}^{\mathrm{R}} + \sum_{i=1}^{n^{\mathrm{L}}} \boldsymbol{M}_{T_i}^{\mathrm{L}},$$

$$\boldsymbol{c}_{12} = -\sum_{i=1}^{n^{\mathrm{R}}} \boldsymbol{M}_{T_i}^{\mathrm{R}}(\tilde{\boldsymbol{r}}_i^{\mathrm{R}} - \tilde{\boldsymbol{r}}_0) - \sum_{i=1}^{n^{\mathrm{L}}} \boldsymbol{M}_{T_i}^{\mathrm{L}}(\tilde{\boldsymbol{r}}_i^{\mathrm{L}} - \tilde{\boldsymbol{r}}_0),$$

$$\boldsymbol{c}_{21} = -\tilde{\boldsymbol{r}}_0\boldsymbol{M}_{T_0} + \sum_{i=1}^{n^{\mathrm{R}}} \tilde{\boldsymbol{r}}_i^{\mathrm{R}}\boldsymbol{M}_{T_i}^{\mathrm{R}} + \sum_{i=1}^{n^{\mathrm{L}}} \tilde{\boldsymbol{r}}_i^{\mathrm{L}}\boldsymbol{M}_{T_i}^{\mathrm{L}},$$

$$\boldsymbol{c}_{22} = \boldsymbol{I}_{T_0} + \sum_{i=1}^{n^{\mathrm{R}}} \boldsymbol{I}_{T_i}^{\mathrm{R}} - \sum_{i=1}^{n^{\mathrm{R}}} (\tilde{\boldsymbol{r}}_i^* - \tilde{\boldsymbol{r}}_0)\boldsymbol{M}_{T_i}^{\mathrm{R}}(\tilde{\boldsymbol{r}}_i^{\mathrm{R}} - \tilde{\boldsymbol{r}}_0)$$
$$+ \sum_{i=1}^{n^{\mathrm{L}}} \boldsymbol{I}_{T_i}^{\mathrm{L}} - \sum_{i=1}^{n^{\mathrm{L}}} (\tilde{\boldsymbol{r}}_i^* - \tilde{\boldsymbol{r}}_0)\boldsymbol{M}_{T_i}^{\mathrm{L}}(\tilde{\boldsymbol{r}}_i^{\mathrm{L}} - \tilde{\boldsymbol{r}}_0),$$

$$\boldsymbol{d}_{1i}^* = \sum_{j=i}^{n^*} \boldsymbol{M}_{T_i}^* \tilde{\boldsymbol{k}}_i^* (\boldsymbol{r}_j^* - \boldsymbol{p}_i^*),$$

$$\boldsymbol{d}_{2i}^* = \sum_{j=i}^{n^*} \boldsymbol{I}_{T_j}^* \boldsymbol{k}_i^* + (\tilde{\boldsymbol{r}}_i^* - \tilde{\boldsymbol{r}}_0)\boldsymbol{M}_{T_j}^* \tilde{\boldsymbol{k}}_i^* (\boldsymbol{r}_j^* - \boldsymbol{p}_i^*).$$

2.2.3 Drag forces and buoyant forces

The hydrodynamic drag forces, drag moment and buoyant forces acting on an object that moves in 3-dimensional space are described in this section. Drag force on x_i axis direction element ${}^i f_x^*$, and drag moment ${}^i \boldsymbol{n}_{f_x}^*$ generated by ${}^i f_x^*$ that acted on link i^* can be expressed as follows [77]:

$${}^i f_x^* = \frac{\rho}{2} C_{D_i}^* \int_{-l_{z2}}^{l_{z1}} \int_{-l_{y2}}^{l_{y1}} w_{i_x}^* |w_{i_x}^*| dy_i dz_i, \tag{2.20}$$

$$ {}^{i}\boldsymbol{n}^{*}_{f_x} = \frac{\rho}{2} C^{*}_{D_i} \int_{-l_{z2}}^{l_{z1}} \int_{-l_{y2}}^{l_{y1}} \begin{bmatrix} 0 \\ z_i \\ -y_i \end{bmatrix} w^{*}_{i_x} |w^{*}_{i_x}| dy_i dz_i, \tag{2.21} $$

where

$$ \boldsymbol{w}^{*} = \begin{bmatrix} w^{*}_{i_x}, & w^{*}_{i_y}, & w^{*}_{i_z} \end{bmatrix} = {}^{i}\dot{\boldsymbol{p}}^{*}_{i} + {}^{i}\tilde{\boldsymbol{\omega}}^{*}_{i} \boldsymbol{s}_i, $$

$$ \begin{aligned} \boldsymbol{s}_i &= \begin{bmatrix} x_i, & y_i, & z_i \end{bmatrix}, \\ {}^{i}\dot{\boldsymbol{p}}^{*}_{i} &= {}^{i}\boldsymbol{R}^{*}_{I} \dot{\boldsymbol{p}}^{*}_{i}, \\ {}^{i}\boldsymbol{\omega}^{*}_{i} &= {}^{i}\boldsymbol{R}^{*}_{I} \boldsymbol{\omega}^{*}_{i}. \end{aligned} $$

$\boldsymbol{s}_i$ is consists of arbitrary position vector element of x_i axis direction on the surface of the link. ${}^{i}\dot{\boldsymbol{p}}^{*}_{i}$ and ${}^{i}\boldsymbol{\omega}^{*}_{i}$ are the linear and angular velocity of the Σ^{*}_{i} origin with respect to Σ^{*}_{i}. Similarly, drag force elements ${}^{i}f^{*}_{y}$ and ${}^{i}f^{*}_{z}$ acting on the link on y_i and z_i axes, respectively, and drag moments ${}^{i}\boldsymbol{n}^{*}_{f_y}$ and ${}^{i}\boldsymbol{n}^{*}_{f_z}$ caused by ${}^{i}f^{*}_{y}$ and ${}^{i}f^{*}_{z}$, respectively, are expressed as

$$ {}^{i}f^{*}_{y} = \frac{\rho}{2} C^{*}_{D_i} \int_{-l_{x2}}^{l_{x1}} \int_{-l_{z2}}^{l_{z1}} w^{*}_{i_y} |w^{*}_{i_y}| dz_i dx_i, \tag{2.22} $$

$$ {}^{i}f^{*}_{x} = \frac{\rho}{2} C^{*}_{D_i} \int_{-l_{y2}}^{l_{y1}} \int_{-l_{x2}}^{l_{x1}} w^{*}_{i_z} |w^{*}_{i_x}| dz_i dy_i, \tag{2.23} $$

$$ {}^{i}\boldsymbol{n}^{*}_{f_y} = \frac{\rho}{2} C^{*}_{D_i} \int_{-l_{x2}}^{l_{x1}} \int_{-l_{z2}}^{l_{z1}} \begin{bmatrix} -z_i \\ 0 \\ x_i \end{bmatrix} w^{*}_{i_y} |w^{*}_{i_y}| dz_i dx_i, \tag{2.24} $$

$$ {}^{i}\boldsymbol{n}^{*}_{f_z} = \frac{\rho}{2} C^{*}_{D_i} \int_{-l_{y2}}^{l_{y1}} \int_{-l_{x2}}^{l_{x1}} \begin{bmatrix} y_i \\ -x_i \\ 0 \end{bmatrix} w^{*}_{i_z} |w^{*}_{i_z}| dx_i dy_i. \tag{2.25} $$

Therefore, based on (2.20) to (2.25), drag forces and drag moment acting on link i^{*} with respect to Σ_I are expressed as

$$ {}^{i}\boldsymbol{f}^{*}_{d_i} = \begin{bmatrix} {}^{i}f^{*}_{x}, & {}^{i}f^{*}_{y}, & {}^{i}f^{*}_{z} \end{bmatrix}^{T}, \tag{2.26} $$

$$ {}^{i}\boldsymbol{n}^{*}_{d_i} = {}^{i}\boldsymbol{n}^{*}_{f_x} + {}^{i}\boldsymbol{n}^{*}_{f_y} + {}^{i}\boldsymbol{n}^{*}_{f_z}. \tag{2.27} $$

Additionally, gravitational force and buoyant force acting on link i^{*} that produced additional force and torque acting on joint i^{*} can be written as

$$ {}^{i}\boldsymbol{f}^{*}_{g_i} = {}^{i}\boldsymbol{R}^{*}_{I}(\rho V^{*}_{i} - m^{*}_{i})\boldsymbol{g}, \tag{2.28} $$

$$ {}^{i}\boldsymbol{n}_{g_i}^{*} = {}^{i}\boldsymbol{R}_{I}^{*}(\tilde{\boldsymbol{a}}_{b_i}^{*}\rho V_i^{*} - \tilde{\boldsymbol{a}}^{*}\boldsymbol{\prime}_{g_i} m_i^{*})\boldsymbol{g}, \tag{2.29} $$

where $\boldsymbol{a}_{g_i}^{*}$ and $\boldsymbol{a}_{b_i}^{*}$ are the position vectors from joint i^{*} to the center of mass and buoyancy for link i^{*}, respectively. Thus, drag and buoyant forces acting on each link of both arms have been described. Moreover, drag and buoyant forces acting on link 0 which is the robot base can also be derived using the similar method.

2.2.4 Equation of motion

The equation of motion for an underwater robot by considering hydrodynamic forces described above, can be obtained using recursive Newton-Euler formulation containing forward recursion and backward recursion [78, 80].

As a first step, in order to calculate the forces and moments acting on each link of the arms, the required angular velocity, angular acceleration and linear acceleration of each joint, and the acceleration of the center of mass of each link are defined as follows

$$ {}^{i}\boldsymbol{\omega}_{i}^{*} = {}^{i}\boldsymbol{R}_{i-1}^{*}\,{}^{i-1}\boldsymbol{\omega}_{i-1}^{*} + {}^{i}\boldsymbol{k}_{i}^{*}\dot{\phi}_{i}^{*}, \tag{2.30} $$

$$ {}^{i}\dot{\boldsymbol{\omega}}_{i}^{*} = {}^{i}\boldsymbol{R}_{i-1}^{*}\,{}^{i-1}\dot{\boldsymbol{\omega}}_{i-1}^{*} + {}^{i}\boldsymbol{k}_{i}^{*}\ddot{\phi}_{i}^{*} + {}^{i}\boldsymbol{\omega}_{i}^{*} \times {}^{i}\boldsymbol{k}_{i}^{*}\dot{\phi}_{i}^{*}, \tag{2.31} $$

$$ {}^{i}\ddot{\boldsymbol{p}}_{i}^{*} = {}^{i}\boldsymbol{R}_{i-1}^{*}\left\{{}^{i-1}\ddot{\boldsymbol{p}}_{i-1}^{*} + {}^{i-1}\boldsymbol{\omega}_{i-1}^{*} \times {}^{i-1}\boldsymbol{l}_{i-1}^{*} + {}^{i-1}\boldsymbol{\omega}_{i-1}^{*} \times ({}^{i-1}\boldsymbol{\omega}_{i-1}^{*} \times {}^{i-1}\boldsymbol{l}_{i-1}^{*})\right\}, \tag{2.32} $$

$$ {}^{i}\ddot{\boldsymbol{r}}_{i}^{*} = {}^{i}\ddot{\boldsymbol{p}}_{i}^{*} + {}^{i}\boldsymbol{\omega}_{i}^{*} \times {}^{i}\boldsymbol{a}_{g_i}^{*} + {}^{i}\boldsymbol{\omega}_{i}^{*} \times ({}^{i}\boldsymbol{\omega}_{i}^{*} \times {}^{i}\boldsymbol{a}_{g_i}^{*}), \tag{2.33} $$

where calculations are done sequentially based on $i^{*} = 1,\ 2,\ \cdots,\ n^{*}$ in forward recursion of Newton-Euler formulation. Here, the boundary conditions are set as ${}^{0}\boldsymbol{\omega}_{0} = {}^{0}\boldsymbol{k}_{0}\dot{\phi}_{0}$, ${}^{0}\dot{\boldsymbol{\omega}}_{0} = {}^{0}\boldsymbol{k}_{0}\ddot{\phi}_{0}$ and ${}^{0}\ddot{\boldsymbol{p}}_{0} = {}^{0}\ddot{\boldsymbol{r}}_{0} = {}^{0}\boldsymbol{R}_{I}\ddot{r}_{0}$.

Then, in backward recursion, the force ${}^{i}\hat{\boldsymbol{f}}_{i}^{*}$ and moment ${}^{i}\hat{\boldsymbol{n}}_{i}^{*}$ acting on the center of mass of each link i^{*}, and the force ${}^{i}\boldsymbol{f}_{i}^{*}$ and moment ${}^{i}\boldsymbol{n}_{i}^{*}$ acting on joint i are written as

$$ {}^{i}\hat{\boldsymbol{f}}_{i}^{*} = (m_i^{*}\boldsymbol{E}_3 + {}^{i}\boldsymbol{M}_{a_i}^{*})\,{}^{i}\ddot{\boldsymbol{r}}_{i}^{*}, \tag{2.34} $$

$$ {}^{i}\hat{\boldsymbol{n}}_{i}^{*} = ({}^{i}\boldsymbol{I}_{I}^{*} + {}^{i}\boldsymbol{I}_{a_i}^{*})\,{}^{i}\dot{\boldsymbol{\omega}}_{i}^{*} + {}^{i}\dot{\boldsymbol{\omega}}_{i}^{*} \times \left\{({}^{i}\boldsymbol{I}_{i}^{*} + {}^{i}\boldsymbol{I}_{a_i}^{*})\,{}^{i}\boldsymbol{\omega}_{i}^{*}\right\}, \tag{2.35} $$

$$ {}^{i}\boldsymbol{f}_{i}^{*} = {}^{i}\boldsymbol{R}_{i+1}^{*}\,{}^{i+1}\boldsymbol{f}_{i+1}^{*} + {}^{i}\hat{\boldsymbol{f}}_{i}^{*} + {}^{i}\boldsymbol{f}_{d_i}^{*} + {}^{i}\boldsymbol{f}_{g_i}^{*}, \tag{2.36} $$

$$ {}^{i}\boldsymbol{n}_{i}^{*} = {}^{i}\boldsymbol{R}_{i+1}^{*}\,{}^{i+1}\boldsymbol{n}_{i+1}^{*} + {}^{i}\hat{\boldsymbol{n}}_{i}^{*} + {}^{i}\boldsymbol{a}_{g_i}^{*} \times ({}^{i}\boldsymbol{R}_{i+1}^{*}\,{}^{i+1}\boldsymbol{f}_{i+1}^{*}) + {}^{i}\boldsymbol{r}_{i}^{*} \times {}^{i}\hat{\boldsymbol{f}}_{i}^{*} + {}^{i}\boldsymbol{n}_{d_i}^{*} + {}^{i}\boldsymbol{n}_{g_i}^{*}, \tag{2.37} $$

where calculations are done sequentially based on $i^{*} = n^{*},\ \cdots,\ 2,\ 1,\ 0$ in backward recursion. Here, the boundary conditions for both arms are set as ${}^{n^{*}-1}\boldsymbol{R}_{n^{*}}^{*} = 0$, ${}^{n^{*}}\boldsymbol{f}_{n^{*}}^{*} = 0$ and ${}^{n^{*}}\boldsymbol{n}_{n^{*}}^{*} = 0$. Furthermore, the forces generated from both arms acting on the robot base can be summarized as

$$ \boldsymbol{f}_0 = \begin{bmatrix} f_{0_x} & f_{0_y} & f_{0_z} \end{bmatrix}^{T} = {}^{I}\boldsymbol{R}_{0}\,{}^{0}\boldsymbol{f}_0, \tag{2.38} $$

$$ \boldsymbol{n}_0 = \begin{bmatrix} n_{0_x} & n_{0_y} & n_{0_z} \end{bmatrix}^{T} = {}^{I}\boldsymbol{R}_{0}\,{}^{0}\boldsymbol{n}_0, \tag{2.39} $$

which are the force and torque vector of the robot base with respect to Σ_I, and

$$\tau_i^* = ({}^i\boldsymbol{k}_i^*)^T {}^i\boldsymbol{n}_i^* \ (i^* = 1,\ 2,\ \cdots,\ n^*) \tag{2.40}$$

is the joint torque vector of the arm. In addition, the subscript i^* on the vectors in Equations (2.30) to (2.40) denotes the component of the vector with respect to coordinate frame Σ_i^*.

Thus, based on the recursive Newton-Euler formulation considering the hydrodynamic forces explained above, the following equation of motion for an underwater robot can be obtained [80] :

$$\boldsymbol{M}(\boldsymbol{q})\dot{\boldsymbol{\zeta}} + \boldsymbol{N}(\boldsymbol{q},\boldsymbol{\zeta})\boldsymbol{\zeta} + \boldsymbol{f}_D = \boldsymbol{u}, \tag{2.41}$$

where $\boldsymbol{q} = [\boldsymbol{r}_0^T,\ \boldsymbol{\psi}_0^T,\ \boldsymbol{\phi}^T]^T$ and $\boldsymbol{\zeta} = [\boldsymbol{\nu}_0^T,\ \dot{\boldsymbol{\phi}}^T]^T$, $\boldsymbol{M}(\boldsymbol{q})$ is the inertia matrix consists of added mass $\boldsymbol{M}_{a_i}^*$ and added inertia moment $\boldsymbol{I}_{a_i}^*$, $\boldsymbol{N}(\boldsymbol{q},\boldsymbol{\zeta})\boldsymbol{\zeta}$ is the vector of Coriolis and centrifugal forces, $\boldsymbol{f}_D$ is the vector consists of drag, gravitational and buoyant forces and moments. $\boldsymbol{u} = [\boldsymbol{u}_B, \boldsymbol{u}_M]^T$ is the input vector consisting of force and torque vectors provided by thrusters and joint torques. $\boldsymbol{u}_B = [\boldsymbol{f}_0^T,\ \boldsymbol{n}_0^T]^T$ and $\boldsymbol{u}_M = [\tau_1^{\mathrm{R}},\ \tau_2^{\mathrm{R}},\ \cdots,\ \tau_{n^{\mathrm{R}}}^{\mathrm{R}},\ \tau_1^{\mathrm{L}},\ \tau_2^{\mathrm{L}},\ \cdots,\ \tau_{n^{\mathrm{L}}}^{\mathrm{L}}]^T$.

Additionally, by using roll-pitch-yaw attitude vectors $\boldsymbol{\psi}_0 = [\psi_{r_0},\ \psi_{p_0},\ \psi_{y_0}]^T$ and $\boldsymbol{\psi}_e^* = [\psi_{r_e}^*,\ \psi_{p_e}^*,\ \psi_{y_e}^*]^T$, angular velocity of the robot base $\boldsymbol{\omega}_0$ and angular velocity of both end-tip of the arms $\boldsymbol{\omega}_e^*$ can be expressed as

$$\boldsymbol{\omega}_0 = \boldsymbol{S}_{\psi_0}\dot{\boldsymbol{\psi}}_{\boldsymbol{0}}, \tag{2.42}$$

$$\boldsymbol{\omega}_e^* = \boldsymbol{S}_{\psi_e}^*\dot{\boldsymbol{\psi}}_{\boldsymbol{e}}^*, \tag{2.43}$$

where

$$\boldsymbol{S}_{\psi_0} = \begin{bmatrix} \cos\psi_{p_0}\cos\psi_{p_0} & -\sin\psi_{y_0} & 0 \\ \cos\psi_{p_0}\sin\psi_{p_0} & \cos\psi_{y_0} & 0 \\ \sin\psi_{p_0} & 0 & 1 \end{bmatrix},$$

$$\boldsymbol{S}_{\psi_e}^* = \begin{bmatrix} \cos\psi_{p_e}^*\cos\psi_{p_e}^* & -\sin\psi_{y_e}^* & 0 \\ \cos\psi_{p_e}^*\sin\psi_{p_e}^* & \cos\psi_{y_e}^* & 0 \\ \sin\psi_{p_e}^* & 0 & 1 \end{bmatrix}.$$

Therefore, the relationship between $\dot{\boldsymbol{q}}$ and $\boldsymbol{\zeta}$ is described as

$$\boldsymbol{\zeta} = \boldsymbol{S}\dot{\boldsymbol{q}},$$

where

$$\boldsymbol{S} = \begin{bmatrix} \boldsymbol{E}_3 & \boldsymbol{0} & \boldsymbol{0} \\ \boldsymbol{0} & \boldsymbol{S}_{\psi_0} & \boldsymbol{0} \\ \boldsymbol{0} & \boldsymbol{0} & \boldsymbol{E}_{(n^{\mathrm{R}}+n^{\mathrm{L}})} \end{bmatrix}.$$

2.3 Resolved acceleration control method

Resolved acceleration control (RAC) method for UVMS is a unique control method that enables coordinated motion control of an underwater vehicle and the end-tips of the arm. RAC method that was introduced in [77] showed that in spite of large position and attitude errors of the underwater vehicle, good control performances of the end-tip of a single arm to follow a pre-planned trajectory can be achieved. The method utilizes the kinematic and momentum equations using feedback of task space signals consisting of the position and attitude of vehicle and end-tips, and also linear and angular velocities of the vehicle and end-tips. In this work, for ease of explanation, RAC method for an underwater vehicle equipped with dual-arm will be described based on the work done by [77].

First, by differentiating both sides of the kinematic and momentum equations described in Equations (2.14) and (2.19) with respect to time, the following equations can be obtained:

$$\boldsymbol{A}\dot{\boldsymbol{\nu}}_0 + \boldsymbol{B}\ddot{\boldsymbol{\phi}} = \dot{\boldsymbol{\nu}}_e - (\dot{\boldsymbol{A}}\boldsymbol{\nu}_0 + \dot{\boldsymbol{B}}\dot{\boldsymbol{\phi}}), \tag{2.44}$$

$$\boldsymbol{H}\dot{\boldsymbol{\nu}}_0 + \boldsymbol{D}\ddot{\boldsymbol{\phi}} = \dot{\boldsymbol{\nu}}_0 + \dot{\boldsymbol{s}} - (\dot{\boldsymbol{C}}\boldsymbol{\nu}_0 + \dot{\boldsymbol{D}}\dot{\boldsymbol{\phi}}), \tag{2.45}$$

where

$$\boldsymbol{H} = \boldsymbol{C} + \boldsymbol{E}_6.$$

The equation that shows the relationship between the desired acceleration of the robot base and arm's end-tips $\boldsymbol{\beta}(t)$, and the required linear and angular acceleration of the robot base and each joint $\boldsymbol{\alpha}(t)$ can be expressed by combining Equations (2.44) and (2.45). As a result, the following equation can be obtained:

$$\boldsymbol{W}(t)\boldsymbol{\alpha}(t) = \boldsymbol{\beta}(t) + \boldsymbol{f}(t) - \dot{\boldsymbol{W}}(t)\boldsymbol{\upsilon}(t), \tag{2.46}$$

where

$$\boldsymbol{W}(t) = \begin{bmatrix} \boldsymbol{H} & \boldsymbol{D} \\ \boldsymbol{A} & \boldsymbol{B} \end{bmatrix}, \quad \boldsymbol{f}(t) = \begin{bmatrix} \dot{\boldsymbol{s}} \\ \boldsymbol{0} \end{bmatrix}, \quad \boldsymbol{\alpha}(t) = \begin{bmatrix} \dot{\boldsymbol{\nu}}_0 \\ \ddot{\boldsymbol{\phi}} \end{bmatrix}, \quad \boldsymbol{\beta}(t) = \begin{bmatrix} \dot{\boldsymbol{\nu}}_0 \\ \dot{\boldsymbol{\nu}}_e \end{bmatrix}, \quad \boldsymbol{\upsilon}(t) = \begin{bmatrix} \boldsymbol{\nu}_0 \\ \dot{\boldsymbol{\phi}} \end{bmatrix}.$$

Here, $\boldsymbol{\nu}_e = [(\boldsymbol{\nu}_e^{\mathrm{R}})^T,\ (\boldsymbol{\nu}_e^{\mathrm{L}})^T]^T$ is the velocities of the end-tips, $\boldsymbol{\phi} = [(\boldsymbol{\phi}^{\mathrm{R}})^T,\ (\boldsymbol{\phi}^{\mathrm{L}})^T]^T$ is the velocities of the joints on both arms, and $\dot{\boldsymbol{s}}$ is the hydrodynamic force acting on the UVMS.

Furthermore, the control inputs for robot base $\boldsymbol{u}_B$ and joints $\boldsymbol{u}_M$ are represented by the coefficient matrices and vectors of Equation (2.41) in the form of block matrix as

$$\boldsymbol{M} = \begin{bmatrix} \boldsymbol{M}_{BB} & \boldsymbol{M}_{BM} \\ \boldsymbol{M}_{MB} & \boldsymbol{M}_{MM} \end{bmatrix}, \quad \boldsymbol{N} = \begin{bmatrix} \boldsymbol{N}_{BB} & \boldsymbol{N}_{BM} \\ \boldsymbol{N}_{MB} & \boldsymbol{N}_{MM} \end{bmatrix}, \quad \boldsymbol{f} = \begin{bmatrix} \boldsymbol{f}_B \\ \boldsymbol{f}_M \end{bmatrix}, \quad \boldsymbol{u} = \begin{bmatrix} \boldsymbol{u}_B \\ \boldsymbol{u}_M \end{bmatrix}.$$

Based on these, the following equation of motion with respect to the control input of the robot base is obtained:

$$\boldsymbol{M}_{BB}\dot{\boldsymbol{\nu}}_0 + \boldsymbol{M}_{BM}\ddot{\boldsymbol{\phi}} + \boldsymbol{N}_{BB}\boldsymbol{\nu}_0 + \boldsymbol{N}_{BM}\dot{\boldsymbol{\phi}} + \boldsymbol{f}_B = \boldsymbol{u}_B. \tag{2.47}$$

Comparing Equation (2.45) with Equation (2.47), $\boldsymbol{C} = \boldsymbol{M}_{BB}$, $\boldsymbol{D} = \boldsymbol{M}_{BM}$, $\dot{\boldsymbol{C}} = \boldsymbol{N}_{BB}$, $\dot{\boldsymbol{D}} = \boldsymbol{M}_{BB}$ and $\dot{\boldsymbol{s}} = \boldsymbol{u}_B - \boldsymbol{f}_B$ are obtained. Moreover,

$$\dot{\boldsymbol{A}} = \begin{bmatrix} \dot{\boldsymbol{A}}^R \\ \dot{\boldsymbol{A}}^L \end{bmatrix}, \quad \dot{\boldsymbol{A}}^* = \begin{bmatrix} 0 & -(\tilde{\dot{\boldsymbol{p}}}_e - \tilde{\dot{\boldsymbol{r}}}_0) \\ 0 & 0 \end{bmatrix},$$

$$\dot{\boldsymbol{B}} = \begin{bmatrix} \dot{\boldsymbol{B}}^R & 0 \\ 0 & \dot{\boldsymbol{B}}^L \end{bmatrix}, \quad \dot{\boldsymbol{B}}^* = \begin{bmatrix} \boldsymbol{b}_1^* & \boldsymbol{b}_2^* & \cdots & \boldsymbol{b}_n^* \\ \boldsymbol{\omega}_1^* \times \boldsymbol{k}_1^* & \boldsymbol{\omega}_2^* \times \boldsymbol{k}_2^* & \cdots & \boldsymbol{\omega}_1^* \times \boldsymbol{k}_n^* \end{bmatrix},$$

where $\boldsymbol{b}_i^* = (\boldsymbol{\omega}_i^* \times \boldsymbol{k}_i^*) \times (\boldsymbol{p}_e^* - \boldsymbol{p}_i^*) + \tilde{\boldsymbol{k}}_i^* (\dot{\boldsymbol{p}}_e^* - \dot{\boldsymbol{p}}_e^*)$. Therefore, all elements of $\boldsymbol{W}$ and $\dot{\boldsymbol{W}}$ in Equation (3.7) can be calculated.

Then, Equation (2.46) is discretized with sampling period T, and applying accelerations of robot base and both arm's end-tips $\boldsymbol{\beta}(t)$ and differentiated inertia matrix $\dot{\boldsymbol{W}}(t)$ to the backward Euler approximation, the following equation is obtained:

$$\boldsymbol{W}(k)\boldsymbol{\alpha}(k-1) = \frac{1}{T}[\boldsymbol{\nu}(k) - \boldsymbol{\nu}(k-1) + T\boldsymbol{f}(k) - \{\boldsymbol{W}(k) - \boldsymbol{W}(k-1)\}\boldsymbol{v}(k)], \tag{2.48}$$

where

$$\boldsymbol{\nu} = \begin{bmatrix} \boldsymbol{\nu}_0^T & \boldsymbol{\nu}_{\boldsymbol{e}}^{\mathrm{R}T} & \boldsymbol{\nu}_{\boldsymbol{e}}^{\mathrm{L}T} \end{bmatrix}^T.$$

Note that a computational time delay is introduced into Equation (2.48), and discrete time kT is abbreviated to k. Therefore, the desired linear and angular accelerations (resolved acceleration) for robot base and each joint of both arms that utilized velocity feedback $\boldsymbol{\alpha}_d(k)$ is defined as follows:

$$\boldsymbol{\alpha}_d(k) = \frac{1}{T}\boldsymbol{W}^{\#}(k)\left\{\boldsymbol{\nu}_d(k+1) - \boldsymbol{\nu}_d(k) + \boldsymbol{\Lambda}\boldsymbol{e}_\nu(k-1) + T\boldsymbol{f}(k)\right\}, \tag{2.49}$$

where

$$\boldsymbol{e}_\nu(k) = \boldsymbol{\nu}_d(k) - \boldsymbol{\nu}(k),$$

and $\boldsymbol{\nu}_d(k)$ is the desired value of $\boldsymbol{\nu}(k)$, $\boldsymbol{\Lambda}$ =diag$\{\lambda_i\}$ (i =1, $\cdots$, 18) is the velocity feedback gain matrix. Furthermore, $\boldsymbol{W}^{\#}(k)$ is the pseudoinverse of $\boldsymbol{W}(k)$ that can be defined as

$$\boldsymbol{W}^{\#}(k) = \boldsymbol{W}^T(k)\left\{\boldsymbol{W}(k)\boldsymbol{W}^T(k)\right\}^{-1}.$$

From Equations (2.48) and (2.49), the error equation for the linear and angular accelerations for robot base and each joint of both arms is defined as follows:

$$\begin{aligned} \boldsymbol{W}(k)\boldsymbol{e}_\alpha(k-1) = \frac{1}{T}[&\boldsymbol{e}_\nu(k) - \boldsymbol{e}_\nu(k-1) - T\left\{\boldsymbol{f}(k) - \boldsymbol{f}(k-1)\right\} \\ &+ \boldsymbol{\Lambda}\boldsymbol{e}_\nu(k-1) + \{\boldsymbol{W}(k) - \boldsymbol{W}(k-1)\}\boldsymbol{v}(k)], \end{aligned} \tag{2.50}$$

where

$$\boldsymbol{e}_\alpha(k) = \boldsymbol{\alpha}_d(k) - \boldsymbol{\alpha}(k).$$

Here, assuming the changes of $\boldsymbol{W}(k)$ and $\boldsymbol{f}(k)$ to $\boldsymbol{W}(k) \approx \boldsymbol{W}(k-1)$ and $\boldsymbol{f}(k) \approx \boldsymbol{f}(k-1)$, respectively, are small for one sampling period, Equation (2.50) can be rewritten as

$$\boldsymbol{W}(k+1)\boldsymbol{e}_{\alpha}(k) = \frac{1}{T}\left\{(q-1)\boldsymbol{E} + \boldsymbol{\Lambda}\right\}\boldsymbol{e}_{\nu}(k), \tag{2.51}$$

where q is the forward shift operator. Since all elements of $\boldsymbol{W}(k)$ are bounded, if λ_i is selected to satisfy $0 < \lambda_i < 1$, during $\boldsymbol{e}_{\alpha}(k) \to \boldsymbol{0}$, $\boldsymbol{e}_{\nu}(k) \to \boldsymbol{0}$ $(k \to \infty)$ can be ensured from Equation (2.51).

Moreover, the desired linear and angular velocities for robot base and each end-tip of both arms that utilized position feedback $\boldsymbol{\nu}_d(k)$ is defined as follows:

$$\boldsymbol{\nu}_d(k) = \frac{\boldsymbol{S}_{0e}}{T}\left\{\boldsymbol{x}_d(k) - \boldsymbol{x}_d(k-1) + \boldsymbol{\Gamma}\boldsymbol{e}_x(k-1)\right\}, \tag{2.52}$$

where

$$\boldsymbol{e}_x(k) = \boldsymbol{x}_d(k) - \boldsymbol{x}(k),$$

and $\boldsymbol{x}_d$ is the desired value of $\boldsymbol{x}(k) = [\boldsymbol{x}_0^T(k),\ \boldsymbol{x}_e^{\mathrm{R}T}(k),\ \boldsymbol{x}_e^{\mathrm{L}T}(k)]^T$. Furthermore,

$$\boldsymbol{S}_{0e} = \begin{bmatrix} \boldsymbol{S}_{\boldsymbol{\psi}_0} & \boldsymbol{0} & \boldsymbol{0} \\ \boldsymbol{0} & \boldsymbol{S}_{\boldsymbol{\psi}_e}^{\mathrm{R}} & \boldsymbol{0} \\ \boldsymbol{0} & \boldsymbol{0} & \boldsymbol{S}_{\boldsymbol{\psi}_e}^{\mathrm{L}} \end{bmatrix},$$

$$\boldsymbol{S}_{\boldsymbol{\psi}_e}^{*} = \begin{bmatrix} \boldsymbol{E}_3 & \boldsymbol{0} \\ \boldsymbol{0} & \boldsymbol{S}_e^{*} \end{bmatrix}$$

and $\boldsymbol{\Gamma}$ =diag$\{\gamma_i\}$ $(i$ =1, $\cdots$, 18) is the position error feedback gain matrix. From Equation (2.3) and Equation (2.52), the following error equation can be obtained:

$$\boldsymbol{e}_{\nu}(k) = \frac{\boldsymbol{S}_{0e}}{T}\left\{\boldsymbol{E}_{18} - (\boldsymbol{E}_{18} - \boldsymbol{\Gamma})\boldsymbol{q}^{-1}\right\}\boldsymbol{e}_x(k), \tag{2.53}$$

where $\boldsymbol{\nu}(k)$ is applied to the backward Euler approximation. From Equation (2.53), if γ_i is selected to satisfy $0 < \gamma_i < 1$, during $\boldsymbol{e}_{\nu}(k) \to \boldsymbol{0}(k \to \infty)$, position and angular error of the robot base and end-tips of both arms $\boldsymbol{e}_x(k) \to \boldsymbol{0}$ can be ensured. The configuration of the control system described in this section is shown in Fig. 2.2.

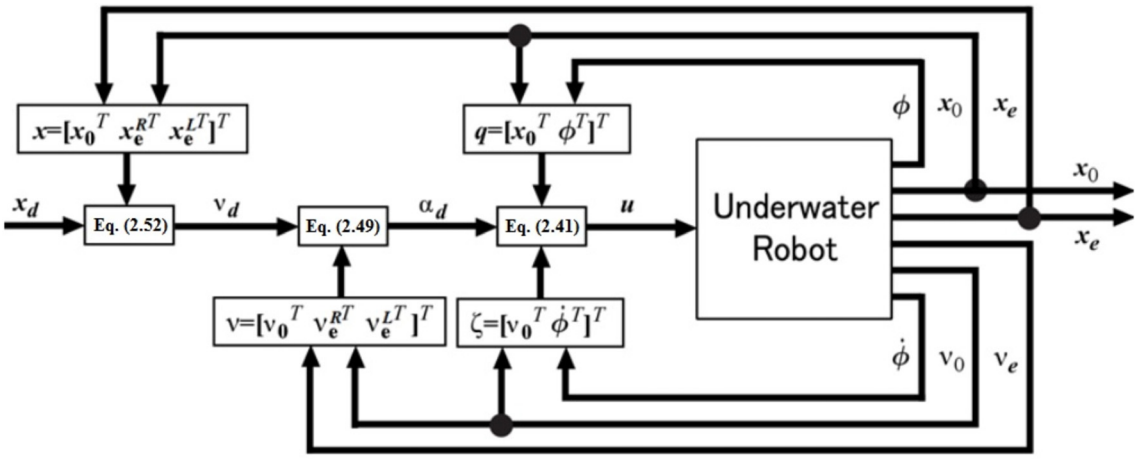

Fig. 2.2: Configuration of control system

Chapter 3

Experiment on a 2-link dual-arm UVMS using RAC method

3.1 Introduction

In Chapter 2, the theoretical work describing a Resolved Acceleration Control (RAC) method for autonomous coordinated motion control of an underwater vehicle and multiple arms has been proposed. The main objective of this chapter is to demonstrate the effectiveness of the proposed RAC method described in Chapter 2 through actual experiment using an underwater vehicle equipped with a 2-link planar dual-arm. First, the main components of the UVMS such as the structure, propulsion system and on-board control system are described. Furthermore, the design of the 2-link planar dual-arm that utilize magnetic coupling mechanism is presented. Then, a RAC method for coordinated motion control of an underwater vehicle equipped with a 2-link planar dual-arm is proposed. Finally, the effectiveness of the developed RAC method is demonstrated through an experiment on using an actual underwater vehicle equipped with the developed 2-link planar dual-arm.

3.2 Dual-arm UVMS

First, in this section, the developed dual-arm UVMS is described. Fig. 3.1 shows the actual image of the developed dual-arm UVMS consists of two units of 2-link dual-arm attached on a semi-autonomous underwater vehicle (robot base). Table 3.1 shows the physical parameters of the dual-arm UVMS. Both of the arms move in horizontal plane, driven by two rotational joints containing servo actuators and magnetic coupling mechanisms.

The robot base has an open-frame structure that is made of lightweight and anti-corrosive Bosch Rexroth's aluminum frames. In addition, the vehicle is attached with floats on several locations to produce equilibrium state between the gravitational and

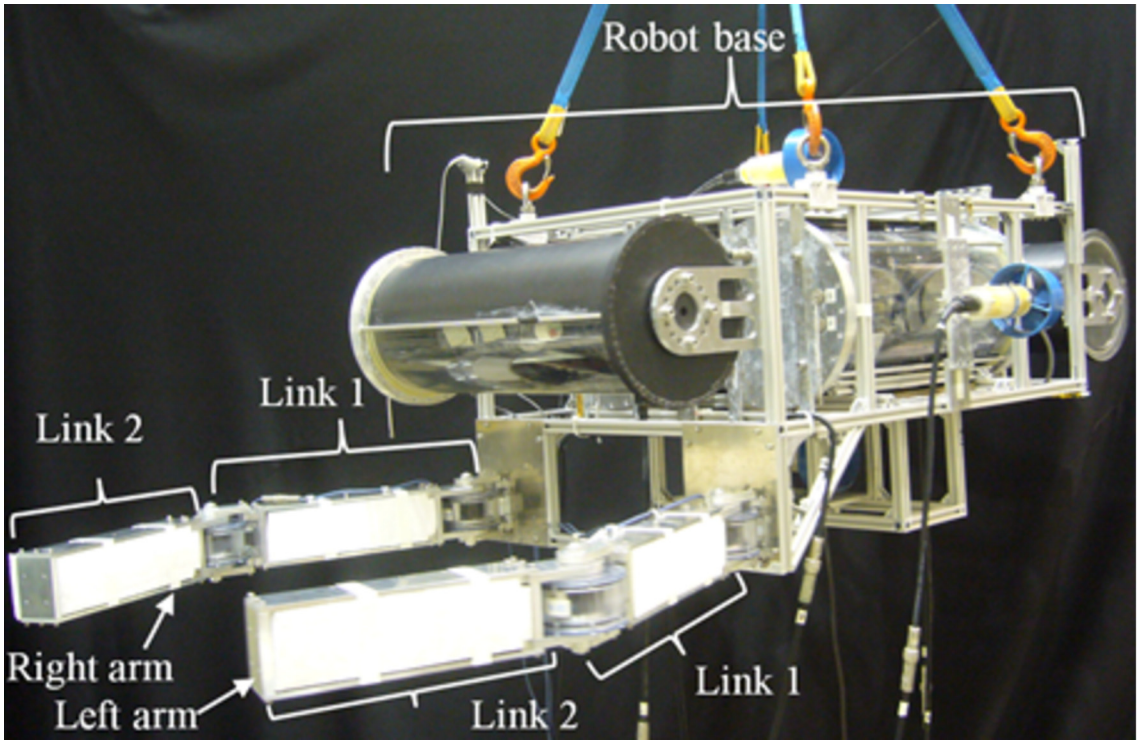

Fig. 3.1: 2-link dual-arm UVMS

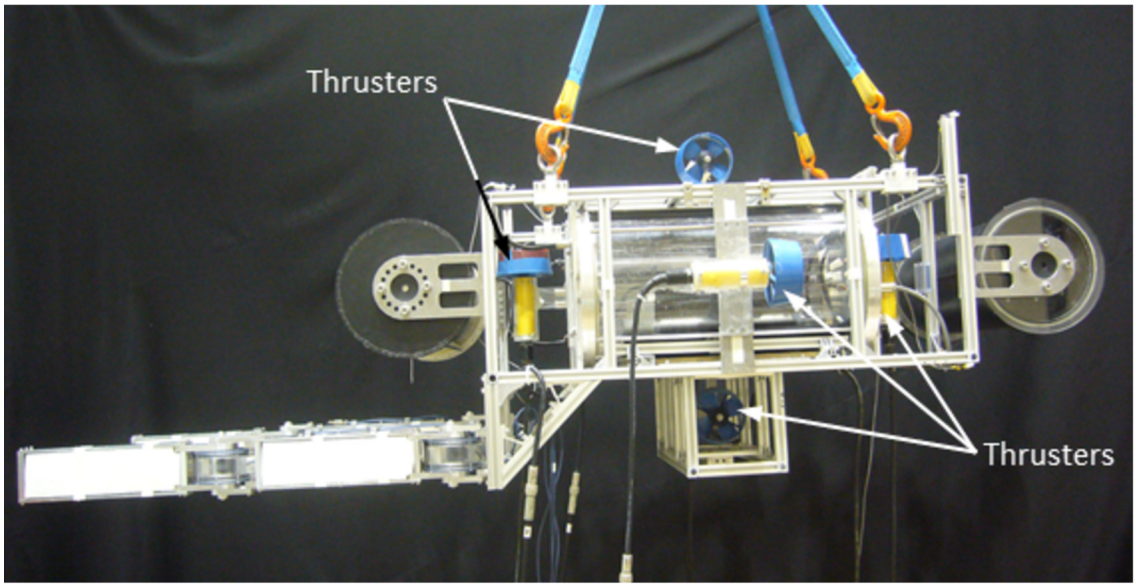

Fig. 3.2: Thrusters positioning on the UVMS

Table 3.1: Physical parameters of underwater robot

	Base	Link 1	Link 2
Mass [kg]	104.520	1.900	1.090
Volume [$\times 10^{-3}$ m^3]	106.214	0.974	1.169
Moment of inertia (x axis) [kgm^2]	2.4	2.71 $\times 10^{-3}$	1.79 $\times 10^{-3}$
Moment of inertia (y axis) [kgm^2]	2.4	49.73 $\times 10^{-3}$	20.85 $\times 10^{-3}$
Moment of inertia (z axis) [kgm^2]	2.4	48.26 $\times 10^{-3}$	19.77 $\times 10^{-3}$
Link length (x axis) [m]	0.870	0.400	0.337
Link length (y axis) [m]	0.640	-	-
Link length (z axis) [m]	0.335	-	-
Link width[m]	-	0.060	0.060
Added mass(x) [kg]	73.19	0.0740	0.0740
Added mass(y) [kg]	30.57	0.814	0.814
Added mass(z) [kg]	99.54	0.384	0.384
Added moment of inertia (x axis) [kgm^2]	0.640	0.002	0.002
Added moment of inertia (y axis) [kgm^2]	1.280	0.040	0.040
Added moment of inertia (z axis) [kgm^2]	0.640	0.040	0.040
Drag coefficient(x)	1.2	0	0
Drag coefficient(y)	1.2	1.0	1.0
Drag coefficient(z)	1.2	1.0	1.0

Fig. 3.3: Single-propeller thruster

buoyant force.

The underwater vehicle is equipped with six units of single-propeller commercial thrusters from Mitsui Engineering and Shipbuilding that allow for linear and angular movements in 3-dimensional space. Fig. 3.2 shows the view from left side of the UVMS showing the positions of 5 from 6 units of thrusters attached on it. Another unit of the thruster is attached on the right side. Fig. 3.3 shows the single-propeller thrusters that is used in this work. The thrusters are installed in the vertical(z-axis), horizontal(x-axis) and lateral(y-axis) directions on the vehicle in pairs. These thrusters provide propulsion for controlling

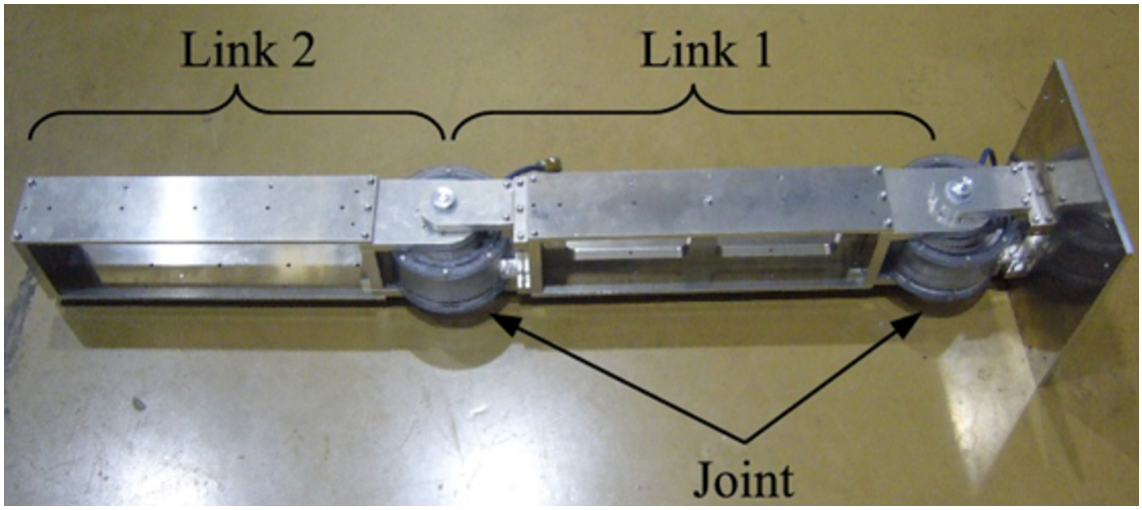

Fig. 3.4: 2-link underwater arm [81]

Table 3.2: Physical parameters of the joint prototype

Height [mm]	138
Width [mm]	113.3
Cylinder diameter [mm]	6
Cylinder thickness [mm]	6
Weight [g]	825

the position and attitude angle of the underwater vehicle. Each of these 40[W] thrusters is capable of producing maximum thrust of about 15[N] at 1400[rpm] (clockwise) and 9.7[N] at 1450[rpm] (counter-clockwise) [79].

3.3 Structure of the 2-link dual-arm

In order to realize a dual-arm UVMS for experimentation purposes, two units of 2-link arm have been designed [81,82]. Fig. 3.1 shows the actual image of the developed dual-arm UVMS consists of two units of 2-link manipulator attached on an underwater robot. Both of the arms move in horizontal plane, driven by two rotational joints containing servo actuators and magnetic coupling mechanisms.

Fig. 3.4 shows an image of the developed 2-link arm utilizing two units of joint prototype. Fig. 3.5(a) shows an image of the developed joint prototype. Fig. 3.6(a) to (c) show the cross-sectional view, side view and an enlarged cross-sectional view of the prototype joint, respectively. While Table 3.2 shows the physical parameters of the joint prototype.

The joint prototype is consists of 2 parts: a waterproof cylindrical case attached to a

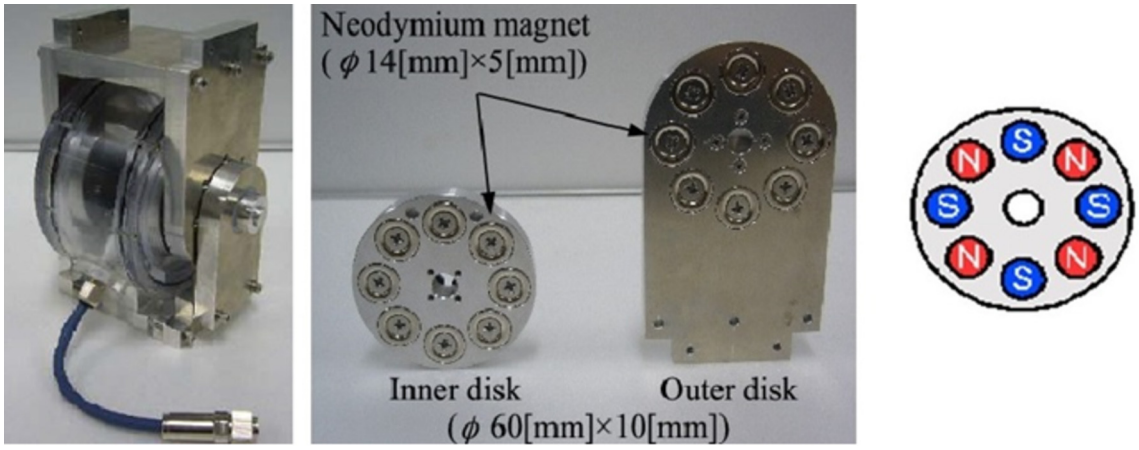

Fig. 3.5: (a) Joint prototype, (b) neodymium magnet coupling, (c) neodymium magnets configuration

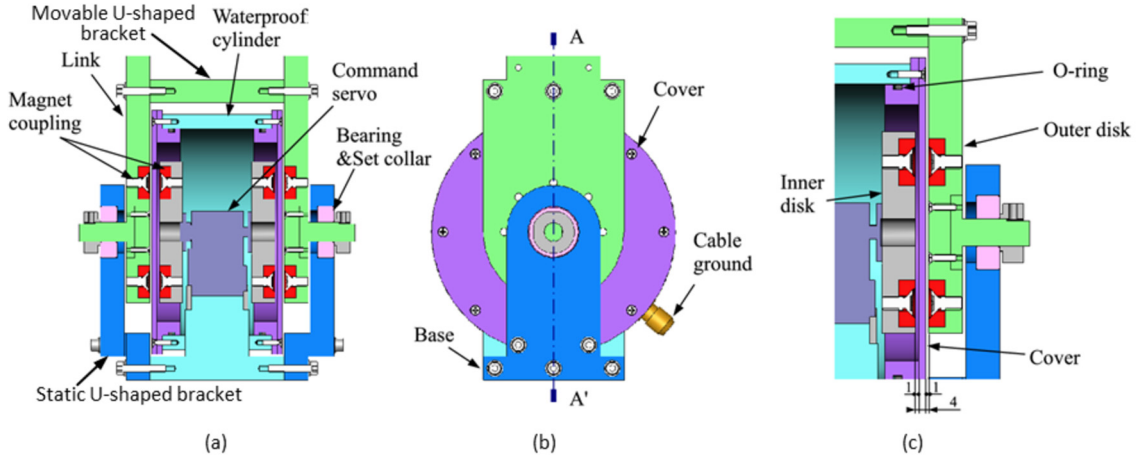

Fig. 3.6: (a) Front cross-section view. (b) Side view. (c) Enlarged view of the magnetic coupling

static U-shaped bracket and a movable U-shaped bracket as shown in Fig. 3.6(a). Both ends of the waterproof cylinder case are designed as lids which can be opened and closed. Waterproofing the internal of the cylinder case is achieved by positioning O-rings between the lids and inner side of the case secured by 8 screws. Both U-shaped brackets act as the joint pivot bracket which can be attached on robot arm's links. Using this prototype joint, a multi-joint robot manipulator design can be made possible by connecting the arm links to other similar joints.

Waterproofed manipulator joint designs without using oil seals are made possible by utilizing neodymium magnetic couplings. Fig. 3.5(b) shows a set of the designed magnetic coupling consists of inner and outer discs (each disc has a diameter of 60[mm] and thickness of 10[mm]). Fig. 3.6(c) shows an enlarged cross-sectional view of the discs location. Each disc is embedded with 8 pieces of neodymium permanent magnets. Each neodymium

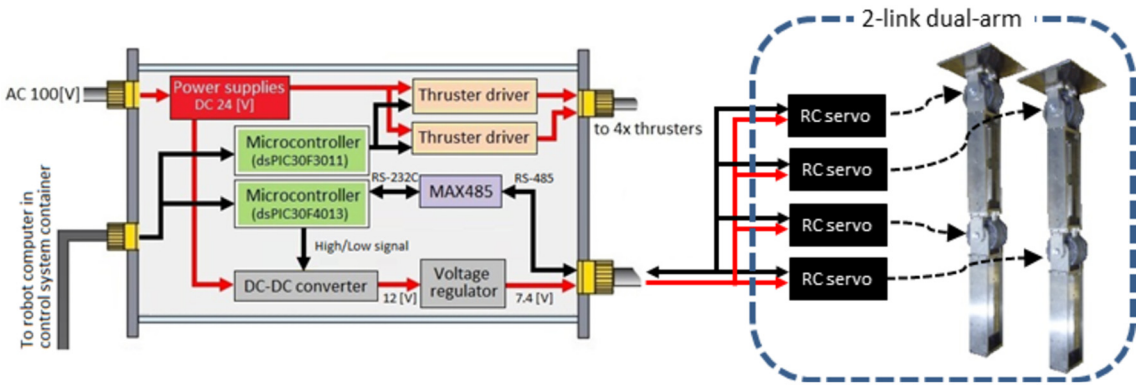

Fig. 3.7: Circuit configuration for the joint actuators

magnets have a diameter of 14[mm] and thickness of 5[mm]. Fig. 3.5(c) shows the magnetic poles arrangement patterns of the magnets. Based on plane air gap type of magnetic coupling mechanism [83], torque can be transmitted between the two discs due to the axially configured magnets, where the north pole of a magnet attracts the south pole of an opposite magnet and vice versa. In previous work, an earlier version of the joint prototype have been developed and showed the maximum performance of torque transmission and comparison of various magnet arrangement patterns [81].

As shown in Fig. 3.6(a), the joint's waterproof cylindrical case contains a Futaba RS301CR electric servo motors as actuators. Fig. 3.7 shows the circuit configuration for the joint actuators. Based on the figure, all RC servos are connected to a servo driver circuit via a single RS-485 serial communication cable. The actuators are command-type RC servos that are controlled via RS-485 communication protocol. The servo driver circuit is consists of a dSPIC30F4013 microcontroller, a DC-DC converter, a voltage regulator and a MAX485 chip. The dsPIC30F4013 microcontroller is connected to the robot computer via RS-232c cables. The microcontroller is used to process the required angle input command from the robot main computer to each joint's command servos. MAX485 transceiver from MAXIM is applied in serial connection between the microcontroller and command servos to allow interface between RS-232c and RS-485 cables.

By utilizing RS-485 communication, the circuits wiring between the robot computer and actuators can be simplified into a single. Steady voltage level is supplied from a voltage stabilizer power supply into a DC-DC converter which converts 24[V] of direct current (DC) to 12[V] for better power efficiency.

Low power consumption is considered by using LM338T 3-terminal voltage regulator which converts the 12[V] to 7.4[V] to power the RC servo motors. Each actuator produces a maximum torque of 7.1[kg·cm] when supplied with 7.4[V] of voltage supply. Joints input commands can be controlled by human through a surface computer connected with the robot main computer via LAN cable.

3.4 RAC method for a 2-link dual-arm UVMS

The RAC method for a 2-link planar dual-arm UVMS described in this section is based on the work done in Chapter 2. Due to this reason, the symbols related to the design of the controller are basically similar to that described in section 2.2. However, an additional assumption is added into the existing assumptions in section 2.2, where the robot motion is limited within a 2-dimensional plane only.

As shown in Fig. 3.1, the UVMS utilized in this work is consists of two units of 2-link planar robotic arms where the motions of both arms are limited only in the x-y plane. Due to this reason, both arm's end-tips are controlled in x and y directions only because the positions in z direction and attitudes (roll-pitch-yaw) of both end-tips rely on the motions of the robot base. Thus, the dimensions of the vectors in kinematic equation, dynamic equation and equation of motion expressed in Equation (2.14), (2.19) and (2.41) can be reduced. These equations can be re-written as

$$\dot{\boldsymbol{x}}_e = \boldsymbol{A}_s \boldsymbol{\nu}_0 + \boldsymbol{B}_s \dot{\boldsymbol{\phi}}, \tag{3.1}$$

$$\boldsymbol{s}_s = \boldsymbol{C}_s \dot{\boldsymbol{x}}_0 + \boldsymbol{D}_s \dot{\boldsymbol{\phi}}, \tag{3.2}$$

$$\boldsymbol{M}(\boldsymbol{q})\dot{\boldsymbol{\zeta}} + \boldsymbol{N}(\boldsymbol{q}, \boldsymbol{\zeta})\boldsymbol{\zeta} + \boldsymbol{f}_D = \boldsymbol{u}, \tag{3.3}$$

where $\boldsymbol{x}_e = [p_{e_x}^{\mathrm{R}}, p_{e_y}^{\mathrm{R}}, p_{e_x}^{\mathrm{L}}, p_{e_y}^{\mathrm{L}}]^T$, $\boldsymbol{\phi} = [\phi_1^{\mathrm{R}}, \phi_2^{\mathrm{R}}, \phi_1^{\mathrm{L}}, \phi_2^{\mathrm{L}}]^T$, $\boldsymbol{q} = [\boldsymbol{r}_0^T, \boldsymbol{\psi}_0^T, \boldsymbol{\phi}^T]^T$, $\boldsymbol{\zeta} = [\boldsymbol{\nu}_0^T, \dot{\boldsymbol{\phi}}^T]^T$ and $\boldsymbol{u} = [{f_0}^T, {n_0}^T, {\boldsymbol{\tau}^{\mathrm{R}}}^T, {\boldsymbol{\tau}^{\mathrm{L}}}^T]^T$. Furthermore, $\boldsymbol{A}_s \in R^{4\times 6}$, $\boldsymbol{B}_s \in R^{4\times 4}$, $\boldsymbol{C}_s \in R^{6\times 6}$, $\boldsymbol{D}_s \in R^{6\times 4}$, $\boldsymbol{M} \in \boldsymbol{R}^{10\times 10}$, $\boldsymbol{N} \in \boldsymbol{R}^{10\times 10}$ and $\boldsymbol{f} \in \boldsymbol{R}^{10\times 1}$ are matrices and vectors.

Furthermore, the control inputs for robot base $\boldsymbol{u}_B = [{\boldsymbol{f}_0}^T, {\boldsymbol{n}_0}^T]^T$ and joints $\boldsymbol{u}_M = [{\boldsymbol{\tau}^{\mathrm{R}}}^T, {\boldsymbol{\tau}^{\mathrm{L}}}^T]^T$ are represented by the coefficient matrices and vectors of Equation (3.3) in the form of block matrix as

$$\boldsymbol{M} = \begin{bmatrix} \boldsymbol{M}_{BB} & \boldsymbol{M}_{BM} \\ \boldsymbol{M}_{MB} & \boldsymbol{M}_{MM} \end{bmatrix},\ \boldsymbol{N} = \begin{bmatrix} \boldsymbol{N}_{BB} & \boldsymbol{N}_{BM} \\ \boldsymbol{N}_{MB} & \boldsymbol{N}_{MM} \end{bmatrix},\ \boldsymbol{f} = \begin{bmatrix} \boldsymbol{f}_B \\ \boldsymbol{f}_M \end{bmatrix},\ \boldsymbol{u} = \begin{bmatrix} \boldsymbol{u}_B \\ \boldsymbol{u}_M \end{bmatrix}.$$

Based on these, the following equation of motion with respect to the control input of the robot base is obtained:

$$\boldsymbol{M}_{BB}\dot{\boldsymbol{\nu}}_0 + \boldsymbol{M}_{BM}\ddot{\boldsymbol{\phi}} + \boldsymbol{N}_{BB}\boldsymbol{\nu}_0 + \boldsymbol{N}_{BM}\dot{\boldsymbol{\phi}} + \boldsymbol{f}_B = \boldsymbol{u}_B. \tag{3.4}$$

Then, by differentiating Equations (3.1) and (3.2) with respect to time, the following equations can be obtained:

$$\ddot{\boldsymbol{x}}_e = \boldsymbol{A}_s\dot{\boldsymbol{\nu}}_0 + \boldsymbol{B}_s\ddot{\boldsymbol{\phi}} + \dot{\boldsymbol{A}}_s\boldsymbol{\nu}_0 + \dot{\boldsymbol{B}}_s\dot{\boldsymbol{\phi}}, \tag{3.5}$$

$$\dot{\boldsymbol{s}}_s = \boldsymbol{C}_s\dot{\boldsymbol{\nu}}_0 + \boldsymbol{D}_s\ddot{\boldsymbol{\phi}} + \dot{\boldsymbol{C}}_s\boldsymbol{\nu}_0 + \dot{\boldsymbol{D}}_s\dot{\boldsymbol{\phi}}. \tag{3.6}$$

Equations (3.5) and (3.6) are summarized by the following single equation:

$$\boldsymbol{W}_s(t)\boldsymbol{\alpha}_s(t) = \boldsymbol{\beta}_s(t) + \boldsymbol{f}_s(t) - \dot{\boldsymbol{W}}_s(t)\boldsymbol{\upsilon}_s(t), \tag{3.7}$$

where,

$$\boldsymbol{W}_s(t) = \begin{bmatrix} \boldsymbol{C}_s + \boldsymbol{E}_6 & \boldsymbol{D}_s \\ \boldsymbol{A}_s & \boldsymbol{B}_s \end{bmatrix},\ \boldsymbol{f}_s(t) = \begin{bmatrix} \dot{\boldsymbol{s}}_s \\ \boldsymbol{0} \end{bmatrix},\ \boldsymbol{\alpha}_s(t) = \begin{bmatrix} \dot{\boldsymbol{\nu}}_0 \\ \ddot{\boldsymbol{\phi}} \end{bmatrix},$$
$$\boldsymbol{\beta}_s(t) = \begin{bmatrix} \dot{\boldsymbol{\nu}}_0 \\ \dot{\boldsymbol{\nu}}_e \end{bmatrix},\ \boldsymbol{\upsilon}_s(t) = \begin{bmatrix} \boldsymbol{\nu}_0 \\ \dot{\boldsymbol{\phi}} \end{bmatrix}.$$

All elements of $\boldsymbol{W}_s$ and $\dot{\boldsymbol{W}}_s$ in Equation (3.7) can be calculated similar to the method described in Section 2.3.

Then, Equation (3.7) is discretized with sampling period T to obtain the following equation:

$$\boldsymbol{W}_s(k)\boldsymbol{\alpha}_s(k-1) = \frac{1}{T}[\boldsymbol{\nu}_s(k) - \boldsymbol{\nu}_s(k-1) + T\boldsymbol{f}_s(k) - \{\boldsymbol{W}_s(k) - \boldsymbol{W}_s(k-1)\}\boldsymbol{\upsilon}_s(k)], \quad (3.8)$$

where $\boldsymbol{\nu}_s = \left[\boldsymbol{\nu}_0^T, {\boldsymbol{\nu}^{\mathrm{R}}}_e^T, {\boldsymbol{\nu}^{\mathrm{L}}}_e^T\right]^T$ and $\boldsymbol{\beta}_s(t)$ and $\dot{\boldsymbol{W}}_s(t)$ are applied to the backward Euler approximation to produce the following equations:

$$\boldsymbol{\beta}_s(k) = \frac{\boldsymbol{\nu}_s(k) - \boldsymbol{\nu}_s(k-1)}{T}, \quad \dot{\boldsymbol{W}}_s(k) = \frac{\boldsymbol{W}_s(k) - \boldsymbol{W}_s(k-1)}{T},$$

Note that computational time delay is introduced to Equation (3.8), and the discrete time kT is abbreviated to k.

From Equation (3.8) the desired acceleration (resolved acceleration) for the robot base and desired angular of both arm's joints $\boldsymbol{\alpha}_s(k)$ is defined as follows:

$$\boldsymbol{\alpha}_s(k) = \frac{1}{T}\boldsymbol{W}_s(k)^{\#}\left\{\boldsymbol{\nu}_s(k+1) - \boldsymbol{\nu}_s(k) + \boldsymbol{\Lambda}\boldsymbol{e}_\nu(k) + T\boldsymbol{f}_s(k)\right\}. \quad (3.9)$$

Moreover, the desired velocity for the robot base and both arm's end-tips $\boldsymbol{\nu}_s(k)$ is defined as follows:

$$\boldsymbol{\nu}_s(k) = \frac{\boldsymbol{S}_{0e}}{T}\left\{\boldsymbol{x}_s(k) - \boldsymbol{x}_s(k-1) + \boldsymbol{\Gamma}\boldsymbol{e}_x(k-1)\right\}, \quad (3.10)$$

where $\boldsymbol{e}_\nu(k) = \boldsymbol{\nu}_s(k) - \boldsymbol{\nu}(k)$, $\boldsymbol{e}_x(k) = \boldsymbol{x}_s(k) - \boldsymbol{x}(k)$ and $\boldsymbol{x}_s = [\boldsymbol{x}_0^T, {\boldsymbol{x}^{\mathrm{R}}}_e^T, {\boldsymbol{x}^{\mathrm{L}}}_e^T]^T$. $\boldsymbol{\Lambda} = \mathrm{diag}\{\Lambda_i\}$ and $\boldsymbol{\Gamma} = \mathrm{diag}\{\Gamma_i\}$ (i =1, $\cdots$, 10) are the velocity and the position feedback gain matrices. T is a sampling period and transformation matrix $\boldsymbol{S}_{0e} = \mathrm{blockdiag}\{\boldsymbol{E}_3, \boldsymbol{S}_{\psi 0}, \boldsymbol{E}_2, \boldsymbol{E}_2\}$, where

$$\boldsymbol{S}_{\boldsymbol{\psi}_0} = \begin{bmatrix} \cos\psi_{p_0}\cos\psi_{p_0} & -\sin\psi_{y_0} & 0 \\ \cos\psi_{p_0}\sin\psi_{p_0} & \cos\psi_{y_0} & 0 \\ \sin\psi_{p_0} & 0 & 1 \end{bmatrix}.$$

Furthermore, $\boldsymbol{W}^{\#}$ is the pseudoinverse of $\boldsymbol{W}$, i.e. $\boldsymbol{W}^{\#} = \boldsymbol{W}^T(\boldsymbol{W}\boldsymbol{W}^T)^{-1}$.

From Equations (3.8), (3.9) and (3.10), if λ_i and γ_i are selected to satisfy $0 < \lambda_i < 1$ and $0 < \gamma_i < 1$, respectively, and the convergence of the acceleration error, $\boldsymbol{e}_\alpha(k) = \boldsymbol{\alpha}_s(k) - \boldsymbol{\alpha}(k)$, tends to zero as k tends to infinity, then the convergence of $\boldsymbol{e}_\nu(k)$ and $\boldsymbol{e}_x(k)$ to zero as k tends to infinity can be ensured.

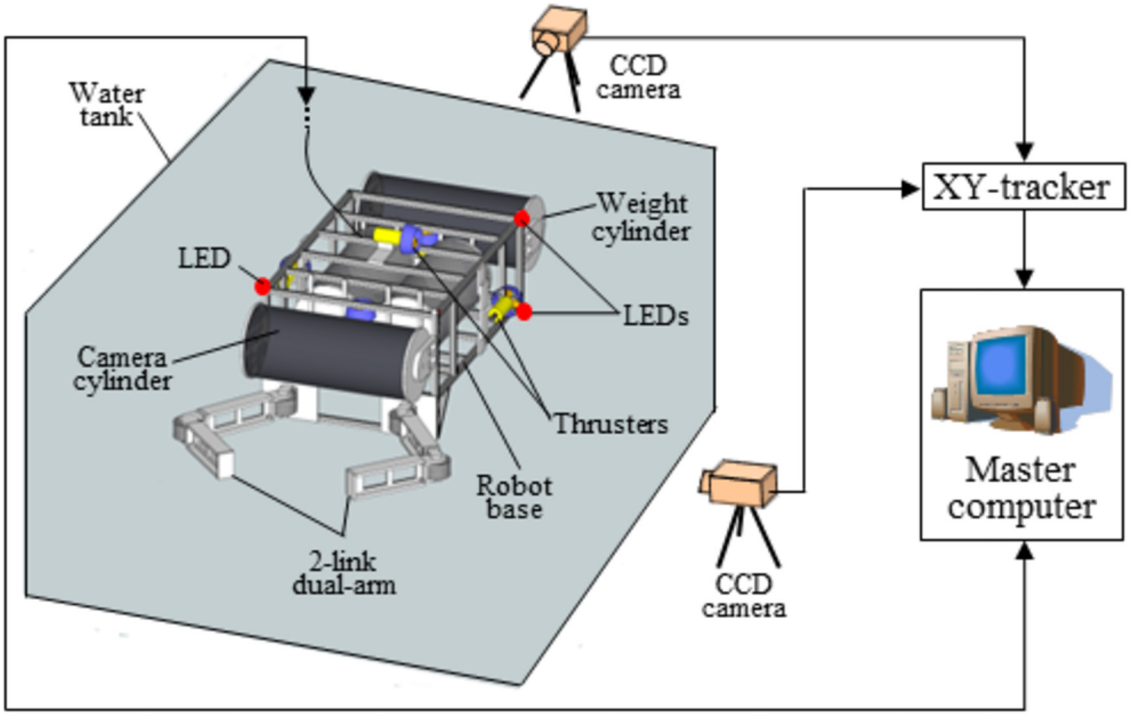

Fig. 3.8: Experimental setup

3.5 Experimental setup

Fig. 3.8 shows an illustration of the experimental setup. The experiment was carried out in a water tank with a length of 2[m], width of 3[m] and depth of 2[m]. Fig. 3.9 shows an image showing the actual condition of the dual-arm UVMS inside the water tank.

The position and attitude of the robot can be calculated by monitoring the movement of three LEDs light sources via CCD cameras. The three LEDs light sources also can be seen in Fig. 3.9. Based on the images captured by the CCD cameras, the coordinates of these LEDs light sources are tracked by the XY-tracker with a processing speed of 1/60[s]. Then, these three coordinates are sent to a surface master computer via a GPIB communication line. Using these coordinates, the position, attitude and speed of the robot base are calculated by the master computer.

Furthermore, the angular values of the joints are obtained from the encoders inside the servo motors, and sent to the master computer. The master computer uses the obtained data of the robot position and attitude of the robot base, and also the angular value of the joints to calculate the control input for the proposed RAC method to control the underwater vehicle, and provide the required commands for each joint actuator. Finally, the master computer sends the desired informations to a robot computer via LAN cable.

A robot computer utilizing a MI953 Mini-ITX motherboard (Intel Core i5 at 2.66GHz with 4GB of memory) is connected to the other on-board vehicle subsystems such as thrusters and servo actuators on the arms. Similar to the surface master computer, the

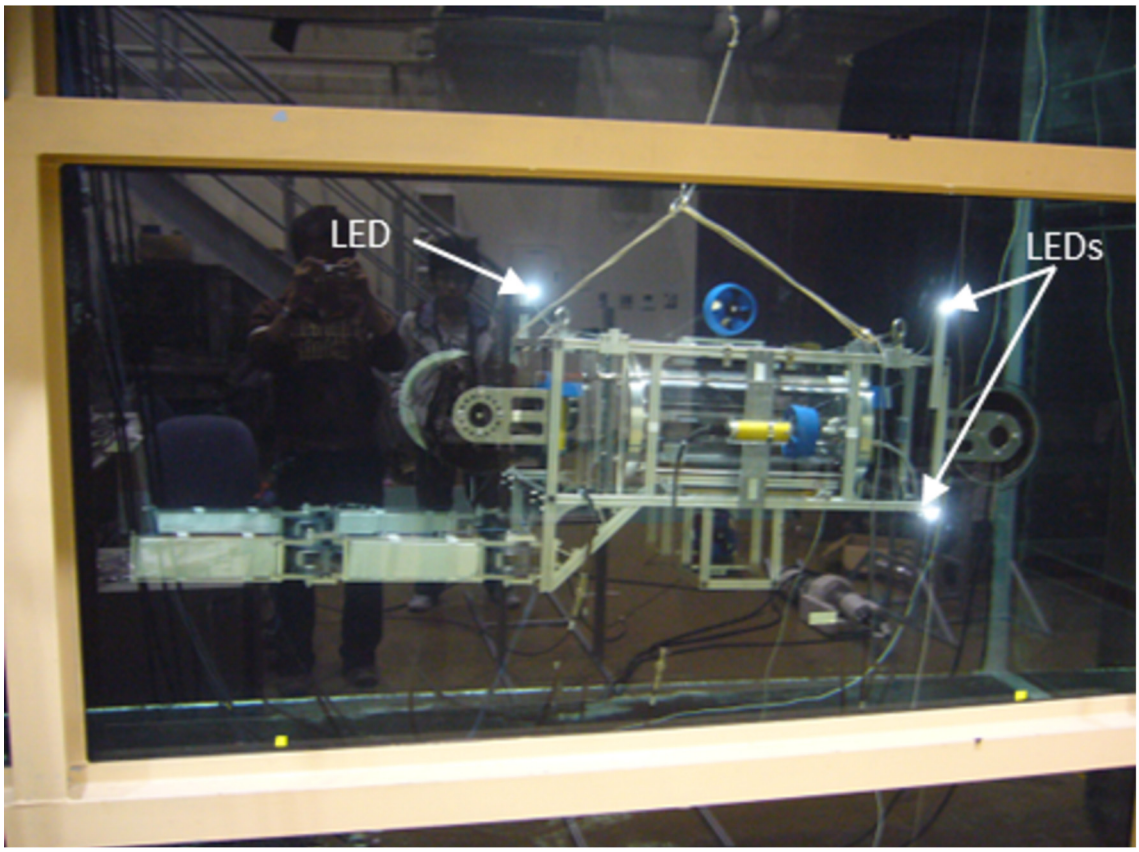

Fig. 3.9: Dual-arm UVMS attached with 3 LEDs light sources for position and attitude measurements

control software for the robot computer is computed using GCC compiler in Debian 6.0 operating system. As described previously, this on-board vehicle control system receives real-time commands and input parameters from the master computer via LAN cable, and controls various subsystems by executing calculations of robot position and attitude using pre-programmed RAC method introduced in section 3.4. Moreover, the calculated position, attitude and various other data from on-board vehicle subsystems are transfered to the surface computer for real-time monitoring and data logging.

3.6 Experimental conditions

In the experiment, both end-tips were controlled to move from initial positions to desired positions along straight paths in a horizontal plane. At the same time, the desired position and attitude of the robot base were similar to the initial values.

The initial position and attitude of the robot base were

$$\begin{aligned}
&\text{initial position } [x,\ y,\ z][\text{m}] \quad : \ [0,0,0][\text{m}],\\
&\text{initial attitude [roll, pitch, yaw][deg]} \quad : \ [0,0,0][\text{deg}],
\end{aligned}$$

and the initial angle for the joints on both arms were

$$\begin{aligned}
\phi_1^{\mathrm{R}} &= -45[\text{deg}], \qquad \phi_2^{\mathrm{R}} = 90[\text{deg}],\\
\phi_1^{\mathrm{L}} &= 45[\text{deg}], \qquad \phi_2^{\mathrm{L}} = -90[\text{deg}].
\end{aligned}$$

As the robot base needed to be in station keeping condition during the experiment, the desired position and attitude of the robot base were the same as the initial position and attitude. However, the desired end-tip positions were

$$\begin{aligned}
&\text{right arm's end-tip} \quad : \ [0, 0.135, 0][\text{m}] \ \text{ from initial position},\\
&\text{left arm's end-tip} \quad : \ [0, -0.135, 0][\text{m}] \ \text{ from initial position}.
\end{aligned}$$

Here, the movements of both end-tips are set up along a straight path from the initial positions to the desired positions. The data sampling period was $T = 1/60[\text{s}]$.

The velocity error feedback gains $\boldsymbol{\Lambda}$ and position and attitude error feedback gains $\boldsymbol{\Gamma}$ for the robot base and both arm's end-tips were

$$\begin{aligned}
\boldsymbol{\Lambda} &= \mathrm{diag}\left\{ \Lambda_{bxyz} \ \ \Lambda_{brpy} \ \ \Lambda_{exyz}^{\mathrm{R}} \ \ \Lambda_{exyz}^{\mathrm{L}} \right\},\\
\boldsymbol{\Gamma} &= \mathrm{diag}\left\{ \Gamma_{bxyz} \ \ \Gamma_{brpy} \ \ \Gamma_{exyz}^{\mathrm{R}} \ \ \Gamma_{exyz}^{\mathrm{L}} \right\},
\end{aligned}$$

where

$$\Lambda_{bxyz} = \begin{bmatrix} 0.15 & 0 & 0 \\ 0 & 0.20 & 0 \\ 0 & 0 & 0.15 \end{bmatrix}, \quad \Lambda_{brpy} = \begin{bmatrix} 0.6 & 0 & 0 \\ 0 & 0.5 & 0 \\ 0 & 0 & 0.5 \end{bmatrix},$$

$$\Lambda_{exyz}^{R} = \begin{bmatrix} 0.6 & 0 \\ 0 & 0.6 \end{bmatrix}, \quad \Lambda_{exyz}^{L} = \begin{bmatrix} 0.6 & 0 \\ 0 & 0.6 \end{bmatrix},$$

$$\Gamma_{bxyz} = \begin{bmatrix} 0.004 & 0 & 0 \\ 0 & 0.010 & 0 \\ 0 & 0 & 0.008 \end{bmatrix}, \quad \Gamma_{brpy} = \begin{bmatrix} 0.05 & 0 & 0 \\ 0 & 0.10 & 0 \\ 0 & 0 & 0.05 \end{bmatrix},$$

$$\Gamma_{exyz}^{R} = \begin{bmatrix} 0.6 & 0 \\ 0 & 0.6 \end{bmatrix}, \quad \Gamma_{exyz}^{L} = \begin{bmatrix} 0.6 & 0 \\ 0 & 0.6 \end{bmatrix}.$$

3.7 Experimental results and discussions

Fig. 3.10 shows the trajectories of the the robot base and both arms at 0[s], 5[s] and 30[s]. Fig. 3.11 to Fig. 3.15 show the experimental results of the performance of the proposed control method.

First, Fig. 3.10 shows the motions of the UVMS in x-y, x-z and y-z planes. The figures show that each end-tip moved towards the desired position in a straight path. At the same time, the robot base was able to maintain it position similar to the initial condition.

Next, Fig. 3.11(a) shows the robot base position errors on x, y and z axes during the movement of both arms. The figure shows that the robot base was able to maintain position errors within ± 0.02[m]. Fig. 3.11(b) shows the robot base attitude errors. The figure shows significantly larger movements on the rotational motion of the robot especially on yaw direction. However, the robot was still able to maintain attitude errors within ± 0.04[rad]. Furthermore, 15[s] after the start of the experiment, the error on yaw direction began to decrease gradually. The recorded attitude errors are considered to be acceptable, considering the large size of the robot base. These results demonstrate that the robot was controlled but the responses to reduce the errors on both the position and attitude were quite slow because the motion of the robot was controlled by the thrusters. Fig. 3.12(a) and (b) show the thrusters control inputs for the robot base translational and rotational motions.

The main purpose of the proposed RAC method is to control both end-tips of the manipulators to move to desired positions despite large motions of robot base. Fig. 3.13 shows the time histories of the desired positions of both arm's end-tips. The figure shows that both arms moving toward the desired positions along the y direction, while maintaining the positions on the x direction. Based on this figure, both arm's reached the target positions in about 8[s], and then maintained its positions for the rest of the time.

Fig. 3.14(a) and (b) shows the time histories of the position error of the both arm's end-tips during the end-tips motions toward the desired positions. The figures demonstrate that although the robot base was excited on both x and y directions, and the robot base yaw angle drifted significantly as shown in Fig. 3.11, both end-tips were able to be controlled on both x and y directions to reach the desired position with relatively small end-tips position errors within the range of ± 0.02[m] to ± 0.03[m]. Furthermore, the errors were instantaneously reduced compared to the position and attitude errors of robot base motions shown in Fig. 3.11. The figures show that the RAC method achieved its purpose, where the end-tips were still able to follow the desired trajectories in spite of the influence from the hydrodynamic forces due to the coupled effects of robot base and manipulators. Fig. 3.15(a) and (b) show the control inputs for the arm's joints that were required to move both end-tips to the desired positions.

3.8 Conclusions

This chapter presented a theoretical works related to a Resolved Acceleration Control (RAC) method for autonomous control of an underwater vehicle equipped with dual-arm. An actual UVMS equipped with newly developed 2-link dual-arm has been used to demonstrate the effectiveness of the proposed method via experimental results.

At the beginning of the chapter, a brief description of the experimental UVMS has been described. The 2-link arm developed in this work consists of joints that utilized magnetic coupling mechanism driven by servo motors. Then, based on the work done in Chapter 2, the theoretical works of the proposed RAC method for a 2-link dual-arm UVMS have been described. Furthermore, the experimental system to verify the effectiveness of the developed RAC method consisting of an underwater vehicle and 2 units of 2-link planar arm have been presented in detail.

To date, this is the first time the effectiveness of a control method for a dual-arm UVMS was verified experimentally using an actual dual-arm UVMS. Based on the experimental results, significantly large motions of the robot base have been indicated on x and y directions. The robot base also drifted significantly in the yaw angle. The translational and rotational motions of the robot base were excited due to the effect caused by the motions of both manipulators and the thrusters performances. However, the proposed method allows both end-tips to be controlled along the desired trajectories despite significantly large motions of the robot base. Thus, the experiment results showed the effectiveness and encouraging results of the proposed RAC method.

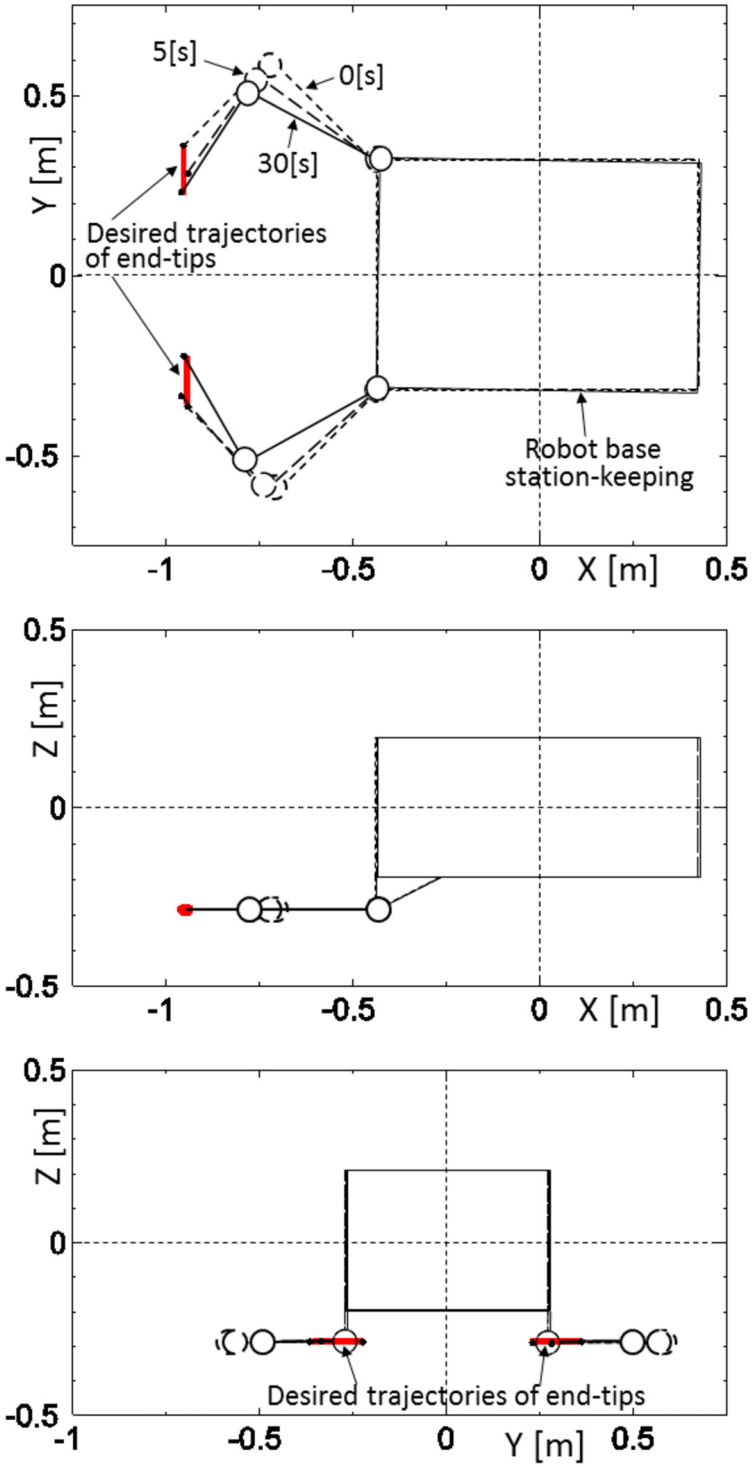

Fig. 3.10: UVMS motion during experiment

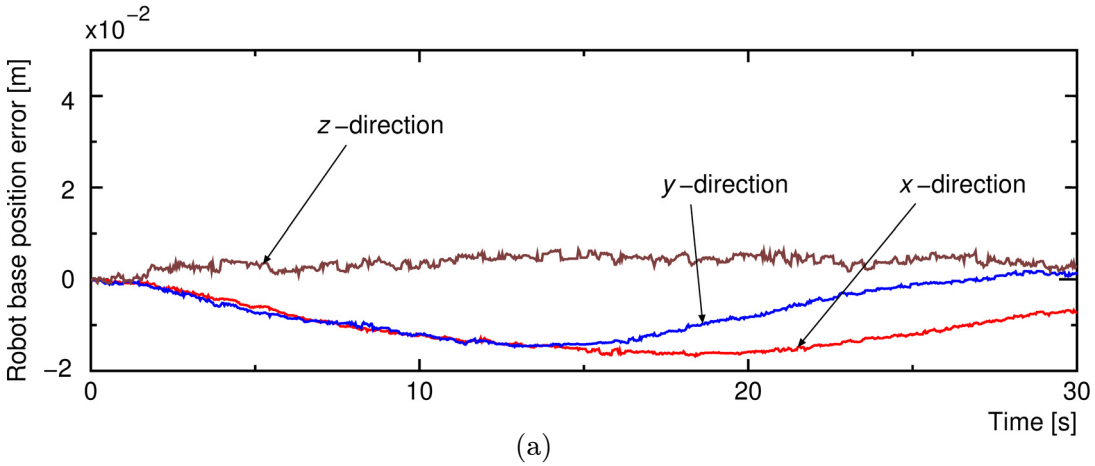

(a)

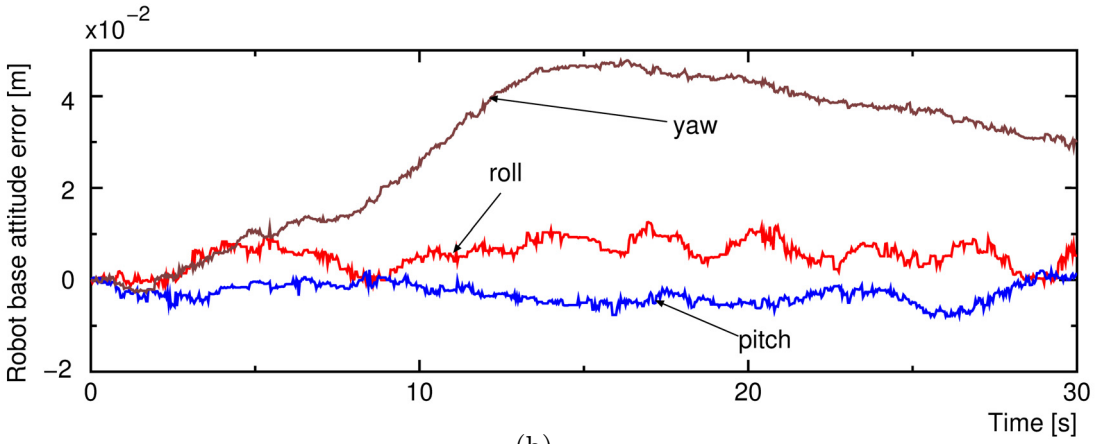

(b)

Fig. 3.11: Robot base position and attitude errors

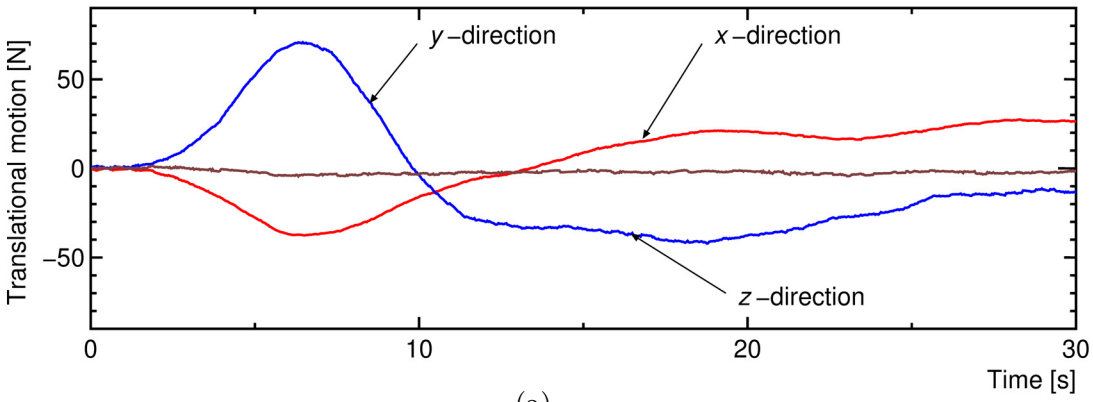

(a)

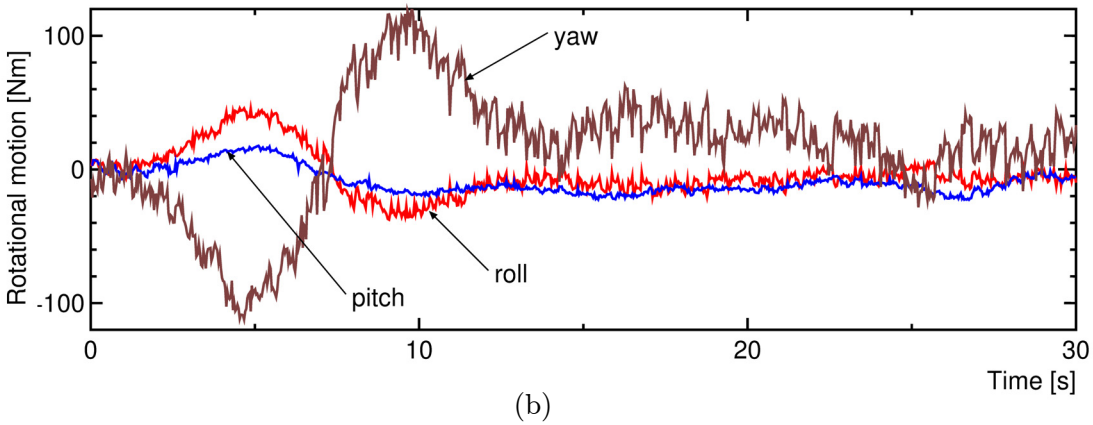

(b)

Fig. 3.12: Control input for robot base

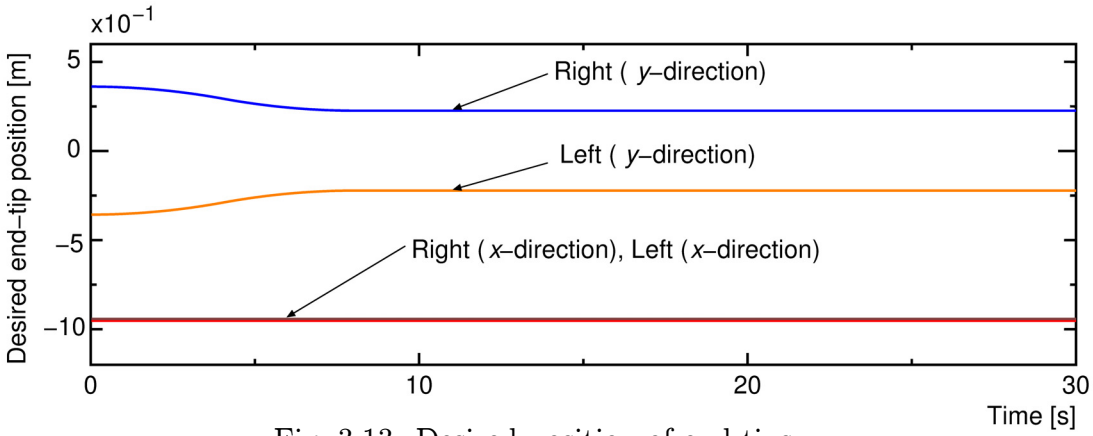

Fig. 3.13: Desired position of end-tips

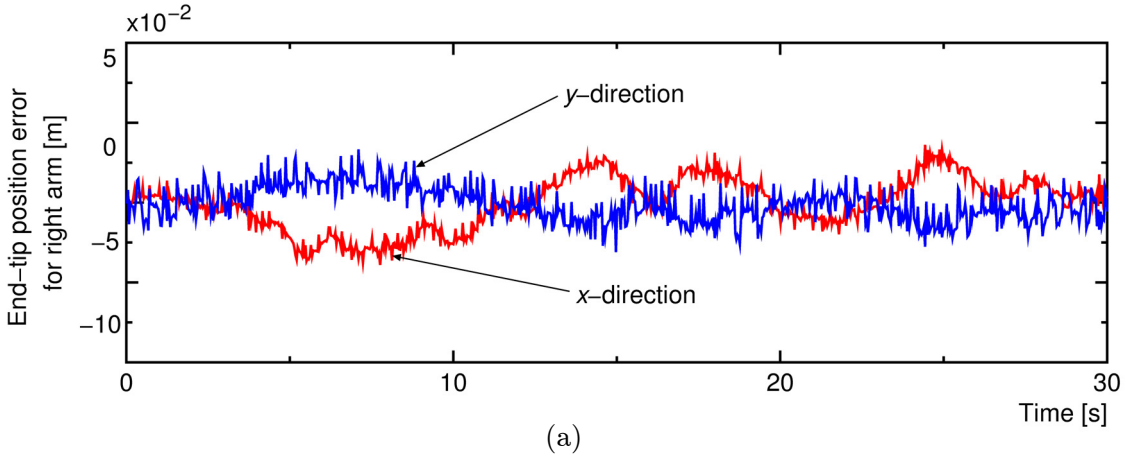

(a)

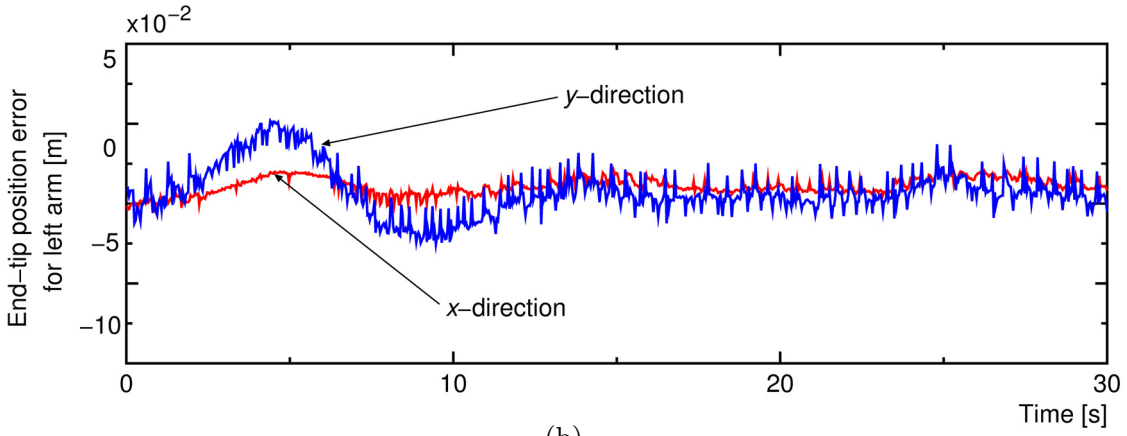

(b)

Fig. 3.14: Position error for arm's end-tips

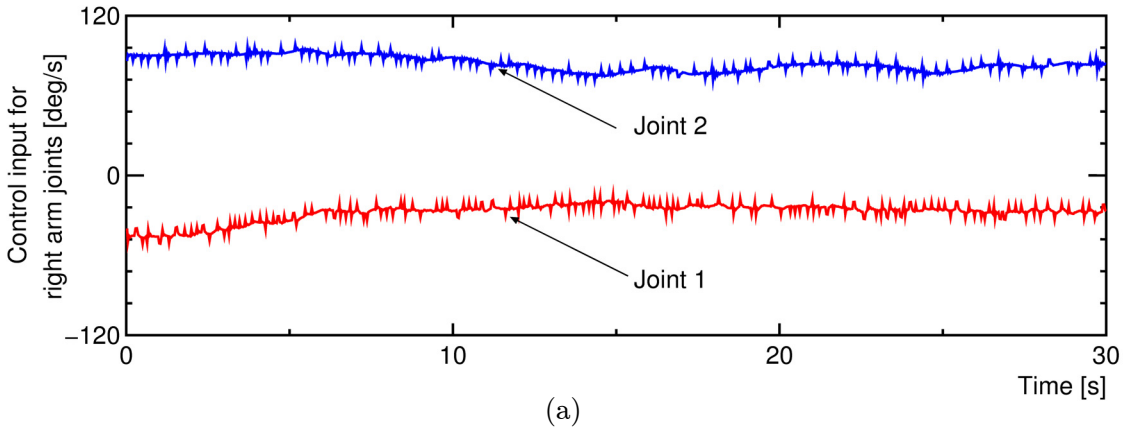

(a)

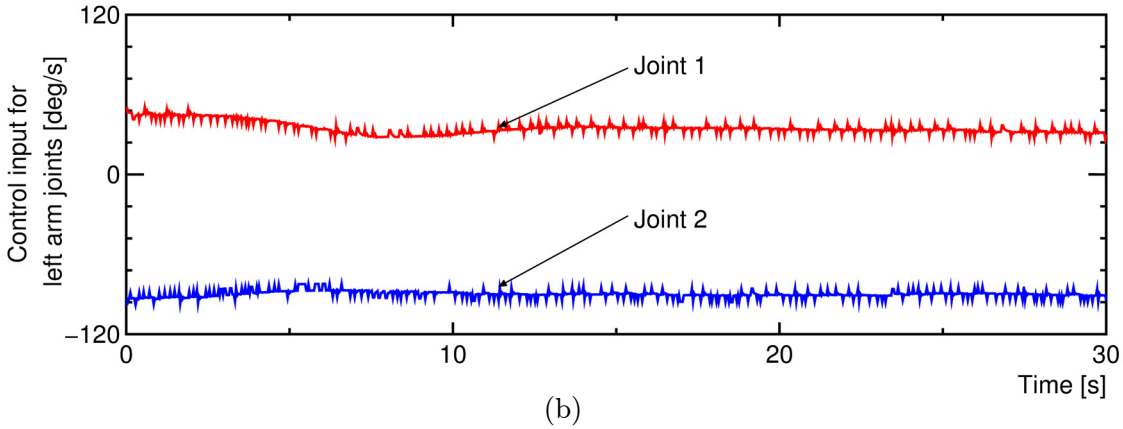

(b)

Fig. 3.15: Control input for both arm's joints

Chapter 4

Experiment on a 3-link dual-arm UVMS using RAC method

4.1 Introduction

The Resolved Acceleration Control (RAC) method described in the previous chapter can be applied on a multiple-link dual-arm UVMS. Therefore, this chapter describes the effectiveness of the proposed Resolved Acceleration Control (RAC) method on controlling a 3-link dual-arm UVMS through experimental results in actual underwater environment.

In the previous chapter, the effectiveness of RAC method has been verified using an underwater vehicle equipped with 2-link planar dual-arm. As both arms were only capable of moving within a plane only (x-y plane), it is impossible to simultaneously control the end-tips to different desired positions in 3-dimensional space (within x-y, x-z or y-z planes). In addition, the joints of the 2-link planar dual-arm utilized magnet coupling mechanism driven by servo actuators. However, problems such as the ability of magnetic coupling to only transfer small amount of torque and slip occurrence during high torque are some of the disadvantages of the design [84, 85].

In this work, a new joint design for 3-link dual-arm that can move in 3-dimensional space has been developed to solve these problems. The developed joints are based on conventional electric motor-driven arm, where torque is directly transmitted from the actuator inside a waterproofed case through drive shaft, O-rings and oil seals to enable the movement of joint and links [86–88]. Detail structure and electrical circuitry of the newly developed joint are described. Then, a RAC method for a 3-link dual-arm UVMS is proposed. Two cases of experiments to demonstrate the performance of the RAC method in controlling both arm's end-tips to move in 3-dimensional space are prepared. At the end of this chapter, based on the experimental results of both cases, the effectiveness of the proposed RAC method for coordinated motion of the AUV and 3-link dual-arm are presented and discussed.

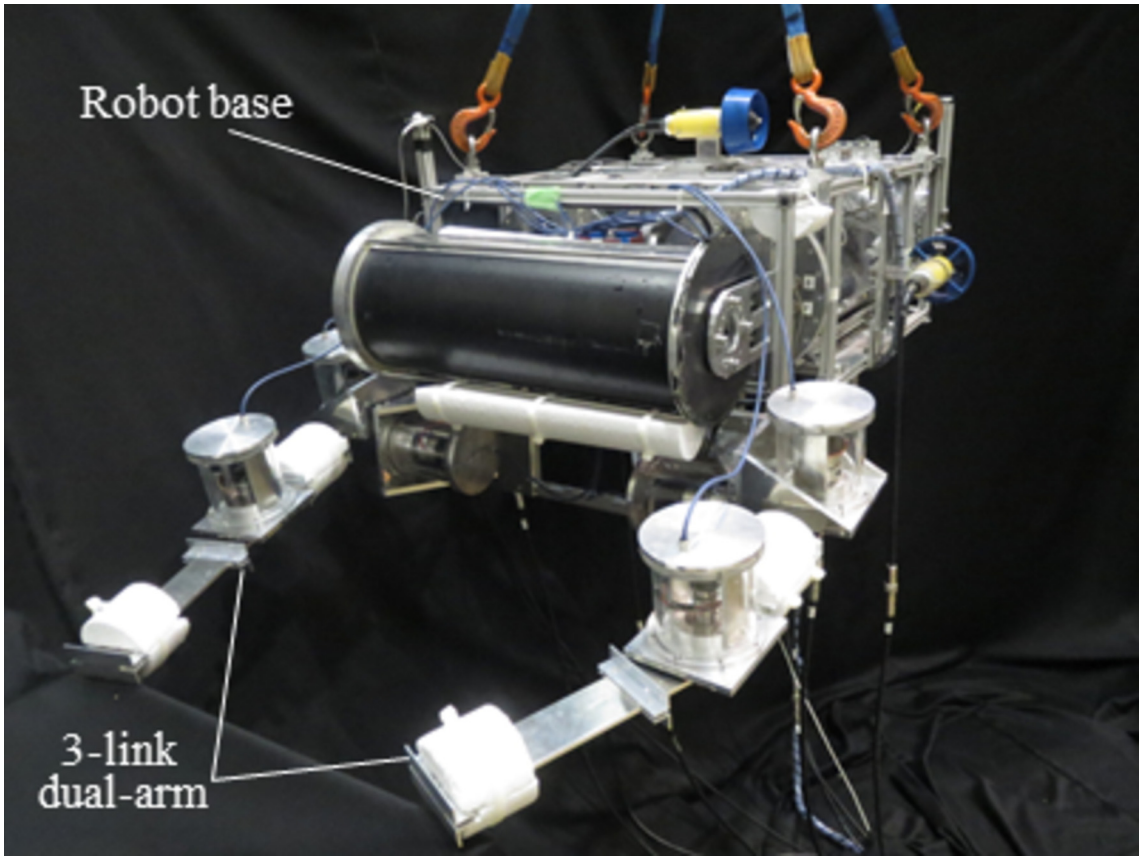

Fig. 4.1: Perspective view of 3-link dual-arm UVMS

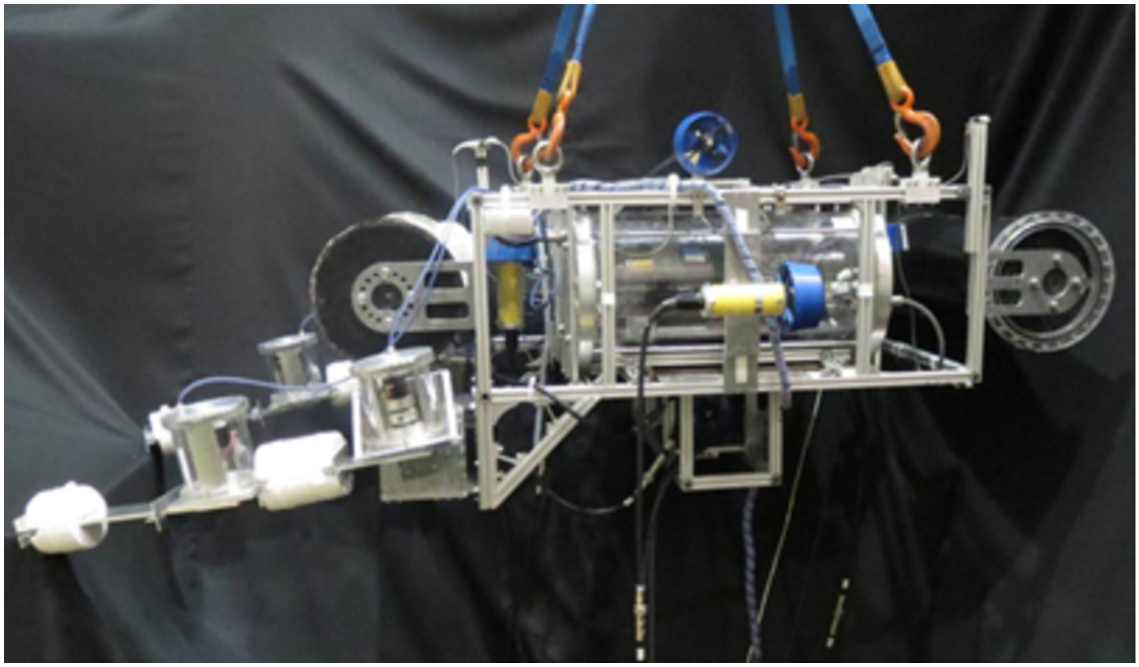

Fig. 4.2: Side view of 3-link dual-arm UVMS

Table 4.1: Physical parameters of underwater robot

	Base	Link 1	Link 2	Link 3
Mass [kg]	104.52	5.90	2.86	1.40
Moment of inertia (x axis) [kgm^2]	2.4	7.933×10^{-3}	3.575×10^{-3}	1.75×10^{-3}
Moment of inertia (y axis) [kgm^2]	2.4	7.933×10^{-3}	23.24×10^{-3}	13.97×10^{-3}
Moment of inertia (z axis) [kgm^2]	2.4	7.368×10^{-3}	23.24×10^{-3}	13.97×10^{-3}
Link length (x axis) [m]	0.870	0.093	0.305	0.335
Link length (y axis) [m]	0.640	-	-	-
Link length (z axis) [m]	0.335	-	-	-
Link diameter[m]	-	0.10	0.10	0.10
Added mass(x) [kg]	73.19	0.730	0.333	0.333
Added mass(y) [kg]	30.57	0.730	2.356	2.631
Added mass(z) [kg]	99.54	0.333	2.356	2.631
Added moment of inertia (x) [kgm^2]	0.64	0.077×10^{-3}	2.454×10^{-3}	2.454×10^{-3}
Added moment of inertia (y) [kgm^2]	1.28	0.077×10^{-3}	27×10^{-3}	46.88×10^{-3}
Added moment of inertia (z) [kgm^2]	0.64	2.4×10^{-3}	27×10^{-3}	46.88×10^{-3}
Drag coefficient(x)	1.2	1.0	1.0	1.0
Drag coefficient(y)	1.2	1.0	1.0	1.0
Drag coefficient(z)	1.2	1.0	1.0	1.0

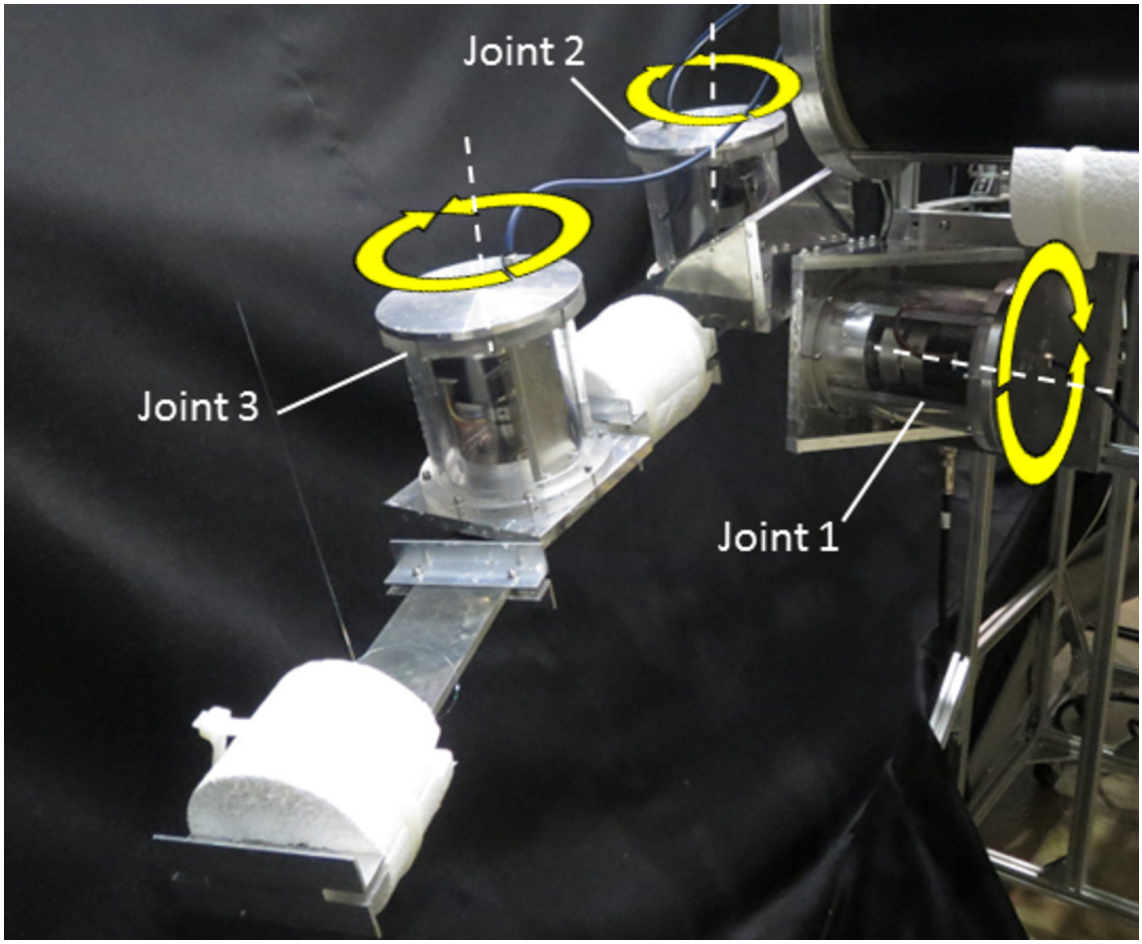

Fig. 4.3: 3-link arm

4.2 Structure of the 3-link dual-arm

4.2.1 Mechanical design of the joint

Fig. 4.1 and Fig. 4.2 show the actual images of the developed dual-arm UVMS consists of two units of 3-link dual-arm attached on an AUV (robot base) from the perspective and side views. Table 4.1 shows the physical parameters of the 3-link dual-arm UVMS.

Fig. 4.3 shows an image of the developed 3-link arm consists of 3 links connected by 3 joints. Fig. 4.4 shows an image of the developed joint consists of a waterproofed cylindrical container that was designed by taking account of the joint's overall weight, ease of manufacturing and protection against corrosion by using acrylic resin and duralumin. Furthermore, at both ends of the cylindrical container are duralumin lids which can be opened and closed. Waterproofing the internal of the cylinder container is achieved by positioning two pieces of O-rings between the lids and the cylindrical container secured by screws. Moreover, oil seals are used to prevent water leaking into the cylindrical container through the output shaft that is connected with the actuator via a disc-type coupling.

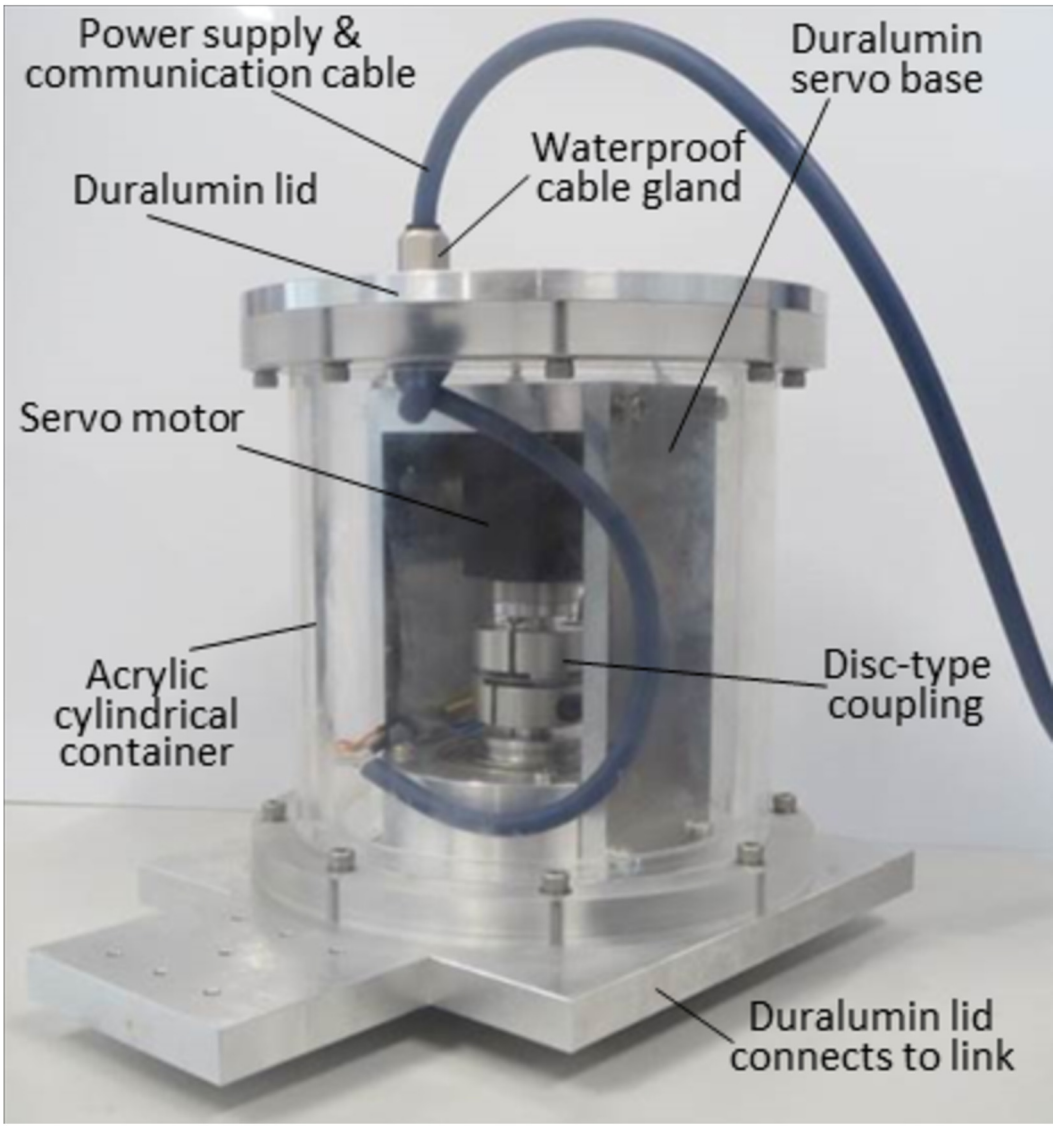

Fig. 4.4: Developed joint for 3-link dual-arm

The power supply and communication cables are connected to the internal parts of the waterproof container via waterproof cable gland.

4.2.2 Joint actuator

Referring to Fig. 4.3, the actuator located inside the waterproof container of Joint 1 is a command-type servo motor (Kondo Kagaku Co. Ltd. B3M-SC-117-A) with a maximum torque of 7.6[Nm]. While Joint 2 and Joint 3 use command-type servo motors (Kondo Kagaku Co. Ltd. B3M-SB-1040-A) with a maximum torque of 4.1[Nm] for each servo. For Joint 1 on both arms, actuators with larger torque are required to move the loads consist of Joint 2, Joint 3 and links. This command-type servo motor adopted RS-485 communication protocol where several units of servo motors can be controlled simultaneously via

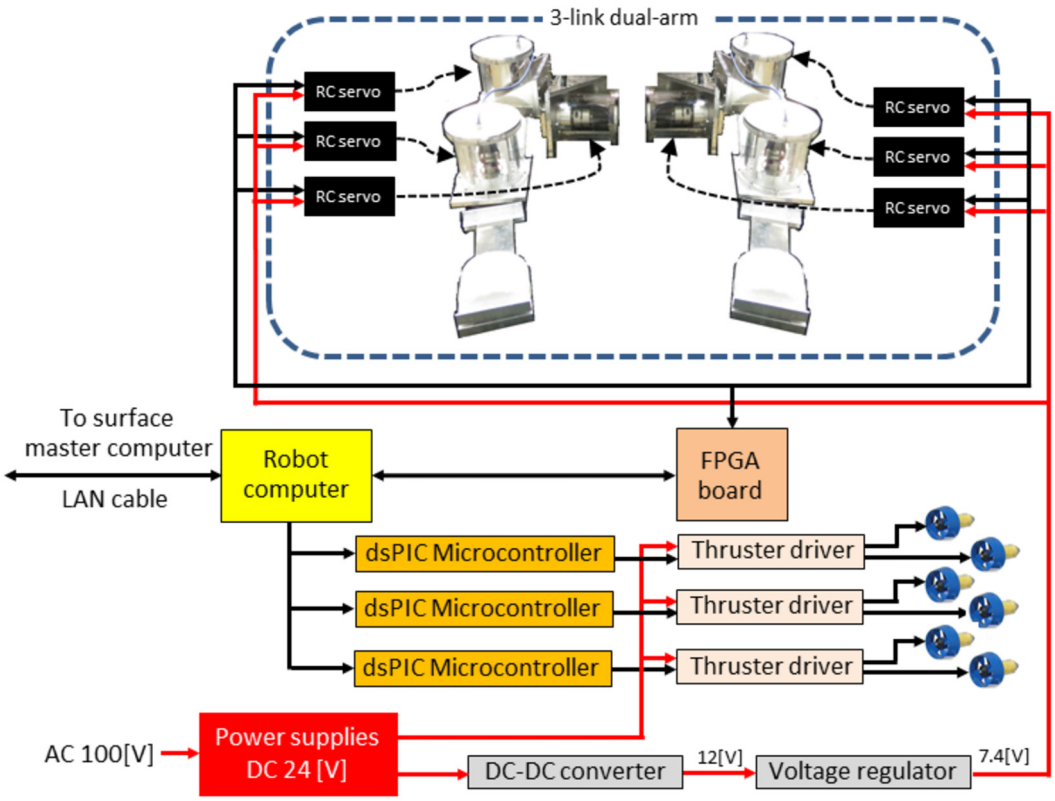

Fig. 4.5: Circuit configuration for the joint actuators

multidrop network by utilizing ID (Identification Data) of each servo motor. Transmission or reception of data can be switched alternately using RS-485 communication line.

Fig. 4.5 shows the circuit configuration for the joint actuators. Based on the figure, the servo motors are connected to the surface master computer via FPGA board. The servo motors communicates with the FPGA board via RS-485 communication line. While the FPGA board communicates with the surface master computer via RS-232C communication line.

Furthermore, an advantage of the command-type servo motors is the user can select the mode of input for the controller inside the servo motor from torque input control mode, velocity input control mode or position input control mode. In addition, the parameters for the controller can be modified according to the required specification.

In the experiment, the controller type and internal parameters of the servo motors are set as velocity input control mode. This is another advantage of the current joint design compared to the previous 2-link joint design. In the 2-link joint design, angular position of joint's actuators are differentiated to derive the angular velocity which can produce calculation errors. However, by utilizing velocity input control mode, this step is not needed. Thus, the calculation errors can be reduced and faster calculation speed can be achieved.

4.3 RAC method for a 3-link dual-arm UVMS

The RAC method for a 3-link planar dual-arm UVMS described in this section is based on the work done in Chapter 2. Due to this, the assumptions and symbols related to the design of the controller are basically similar to that described in section 2.2.

As shown in Fig. 4.3, the UVMS utilized in this work is consists of two units of 3-link robotic arms, where both arms can move in 3-dimensional space. By using 3-link robotic arms, the end-tips of both arm can be controlled to move in x, y and z directions. However, the attitude (roll-pitch-yaw) of both end-tips rely on the motions of the robot base. Thus, the dimensions of the vectors in kinematic equation, dynamic equation and equation of motion expressed in Equation (2.14), (2.19) and (2.41) can be re-written as

$$\dot{\boldsymbol{x}}_e = \boldsymbol{A}_s\boldsymbol{\nu}_0 + \boldsymbol{B}_s\dot{\boldsymbol{\phi}}, \tag{4.1}$$

$$\boldsymbol{s}_s = \boldsymbol{C}_s\dot{\boldsymbol{x}}_0 + \boldsymbol{D}_s\dot{\boldsymbol{\phi}}, \tag{4.2}$$

$$\boldsymbol{M}(\boldsymbol{q})\dot{\boldsymbol{\zeta}} + \boldsymbol{N}(\boldsymbol{q},\boldsymbol{\zeta})\boldsymbol{\zeta} + \boldsymbol{f}_D = \boldsymbol{u}, \tag{4.3}$$

where $\boldsymbol{x}_e = [p_{e_x}^{\mathrm{R}}, p_{e_y}^{\mathrm{R}}, p_{e_z}^{\mathrm{R}}, p_{e_x}^{\mathrm{L}}, p_{e_y}^{\mathrm{L}}, p_{e_z}^{\mathrm{L}}]^T$, $\boldsymbol{\phi} = [\phi_1^{\mathrm{R}}, \phi_2^{\mathrm{R}}, \phi_3^{\mathrm{R}}, \phi_1^{\mathrm{L}}, \phi_2^{\mathrm{L}}, \phi_3^{\mathrm{L}}]^T$, $\boldsymbol{q} = [\boldsymbol{r}_0^T, \boldsymbol{\psi}_0^T, \boldsymbol{\phi}^T]^T$, $\boldsymbol{\zeta} = [\boldsymbol{\nu}_0^T, \dot{\boldsymbol{\phi}}^T]^T$ and $\boldsymbol{u} = [{f_0}^T, {n_0}^T, {\boldsymbol{\tau}^{\mathrm{R}}}^T, {\boldsymbol{\tau}^{\mathrm{L}}}^T]^T$. Furthermore, $\boldsymbol{A}_s \in R^{6\times6}$, $\boldsymbol{B}_s \in R^{6\times6}$, $\boldsymbol{C}_s \in R^{6\times6}$, $\boldsymbol{D}_s \in R^{6\times6}$, $\boldsymbol{M} \in \boldsymbol{R}^{12\times12}$, $\boldsymbol{N} \in \boldsymbol{R}^{12\times12}$ and $\boldsymbol{f} \in \boldsymbol{R}^{12\times1}$ are matrices and vectors.

Furthermore, the control inputs for robot base $\boldsymbol{u}_B = [{\boldsymbol{f}_0}^T, {\boldsymbol{n}_0}^T]^T$ and joints $\boldsymbol{u}_M = [{\boldsymbol{\tau}^{\mathrm{R}}}^T, {\boldsymbol{\tau}^{\mathrm{L}}}^T]^T$ are represented by the coefficient matrices and vectors of Equation (4.3) in the form of block matrix as

$$\boldsymbol{M} = \begin{bmatrix} \boldsymbol{M}_{BB} & \boldsymbol{M}_{BM} \\ \boldsymbol{M}_{MB} & \boldsymbol{M}_{MM} \end{bmatrix}, \quad \boldsymbol{N} = \begin{bmatrix} \boldsymbol{N}_{BB} & \boldsymbol{N}_{BM} \\ \boldsymbol{N}_{MB} & \boldsymbol{N}_{MM} \end{bmatrix}, \quad \boldsymbol{f} = \begin{bmatrix} \boldsymbol{f}_B \\ \boldsymbol{f}_M \end{bmatrix}, \quad \boldsymbol{u} = \begin{bmatrix} \boldsymbol{u}_B \\ \boldsymbol{u}_M \end{bmatrix}.$$

Based on these, the following equation of motion with respect to the control input of the robot base is obtained:

$$\boldsymbol{M}_{BB}\dot{\boldsymbol{\nu}}_0 + \boldsymbol{M}_{BM}\ddot{\boldsymbol{\phi}} + \boldsymbol{N}_{BB}\boldsymbol{\nu}_0 + \boldsymbol{N}_{BM}\dot{\boldsymbol{\phi}} + \boldsymbol{f}_B = \boldsymbol{u}_B. \tag{4.4}$$

Then, by differentiating Equations (4.1) and (2.19) with respect to time, the following equations can be obtained:

$$\ddot{\boldsymbol{x}}_e = \boldsymbol{A}_s\dot{\boldsymbol{\nu}}_0 + \boldsymbol{B}_s\ddot{\boldsymbol{\phi}} + \dot{\boldsymbol{A}}_s\boldsymbol{\nu}_0 + \dot{\boldsymbol{B}}_s\dot{\boldsymbol{\phi}}, \tag{4.5}$$

$$\dot{\boldsymbol{s}}_s = \boldsymbol{C}_s\dot{\boldsymbol{\nu}}_0 + \boldsymbol{D}_s\ddot{\boldsymbol{\phi}} + \dot{\boldsymbol{C}}_s\boldsymbol{\nu}_0 + \dot{\boldsymbol{D}}_s\dot{\boldsymbol{\phi}}. \tag{4.6}$$

Equations (4.5) and (4.6) are summarized by the following single equation:

$$\boldsymbol{W}_s(t)\boldsymbol{\alpha}_s(t) = \boldsymbol{\beta}_s(t) + \boldsymbol{f}_s(t) - \dot{\boldsymbol{W}}_s(t)\boldsymbol{\upsilon}_s(t), \tag{4.7}$$

where,

$$\boldsymbol{W}_s(t) = \begin{bmatrix} \boldsymbol{C}_s + \boldsymbol{E}_6 & \boldsymbol{D}_s \\ \boldsymbol{A}_s & \boldsymbol{B}_s \end{bmatrix}, \quad \boldsymbol{f}_s(t) = \begin{bmatrix} \dot{\boldsymbol{s}}_s \\ \boldsymbol{0} \end{bmatrix}, \quad \boldsymbol{\alpha}_s(t) = \begin{bmatrix} \dot{\boldsymbol{\nu}}_0 \\ \ddot{\boldsymbol{\phi}} \end{bmatrix},$$
$$\boldsymbol{\beta}_s(t) = \begin{bmatrix} \dot{\boldsymbol{\nu}}_0 \\ \dot{\boldsymbol{\nu}}_e \end{bmatrix}, \quad \boldsymbol{\upsilon}_s(t) = \begin{bmatrix} \boldsymbol{\nu}_0 \\ \dot{\boldsymbol{\phi}} \end{bmatrix}.$$

All elements of $\boldsymbol{W}_s$ and $\dot{\boldsymbol{W}}_s$ in Equation (4.7) can be calculated similar to the method described in section 3.4.

Then, Equation (4.7) is discretized with sampling period T to obtain the following equation:

$$\boldsymbol{W}_s(k)\boldsymbol{\alpha}_s(k-1) = \frac{1}{T}[\boldsymbol{\nu}_s(k) - \boldsymbol{\nu}_s(k-1) + T\boldsymbol{f}_s(k) - \{\boldsymbol{W}_s(k) - \boldsymbol{W}_s(k-1)\}\boldsymbol{\upsilon}_s(k)], \quad (4.8)$$

where $\boldsymbol{\nu}_s = \left[\boldsymbol{\nu}_0^T, {\boldsymbol{\nu}^{\mathrm{R}}}_e^T, {\boldsymbol{\nu}^{\mathrm{L}}}_e^T\right]^T$ and $\boldsymbol{\beta}_s(t)$ and $\dot{\boldsymbol{W}}_s(t)$ are applied to the backward Euler approximation to produce the following equations:

$$\boldsymbol{\beta}_s(k) = \frac{\boldsymbol{\nu}_s(k) - \boldsymbol{\nu}_s(k-1)}{T}, \quad \dot{\boldsymbol{W}}_s(k) = \frac{\boldsymbol{W}_s(k) - \boldsymbol{W}_s(k-1)}{T}.$$

Note that computational time delay is introduced to Equation (4.8), and the discrete time kT is abbreviated to k.

From Equation (4.8) the desired acceleration (resolved acceleration) for the robot base and desired angular of both arm's joints $\boldsymbol{\alpha}_s(k)$ is defined as follows:

$$\boldsymbol{\alpha}_s(k) = \frac{1}{T}\boldsymbol{W}_s(k)^{\#}\left\{\boldsymbol{\nu}_s(k+1) - \boldsymbol{\nu}_s(k) + \boldsymbol{\Lambda}\boldsymbol{e}_\nu(k) + T\boldsymbol{f}_s(k)\right\}. \quad (4.9)$$

Moreover, the desired velocity for the robot base and both arm's end-tips $\boldsymbol{\nu}_s(k)$ is defined as follows:

$$\boldsymbol{\nu}_s(k) = \frac{\boldsymbol{S}_{0e}}{T}\left\{\boldsymbol{x}_s(k) - \boldsymbol{x}_s(k-1) + \boldsymbol{\Gamma}\boldsymbol{e}_x(k-1)\right\}, \quad (4.10)$$

where $\boldsymbol{e}_\nu(k) = \boldsymbol{\nu}_s(k) - \boldsymbol{\nu}(k)$, $\boldsymbol{e}_x(k) = \boldsymbol{x}_s(k) - \boldsymbol{x}(k)$ and $\boldsymbol{x}_s = [\boldsymbol{x}_0^T, {\boldsymbol{x}^{\mathrm{R}}}_e^T, {\boldsymbol{x}^{\mathrm{L}}}_e^T]^T$. $\boldsymbol{\Lambda} = \mathrm{diag}\{\Lambda_i\}$ and $\boldsymbol{\Gamma} = \mathrm{diag}\{\Gamma_i\}$ (i =1, $\cdots$, 12) are the velocity and the position feedback gain matrices. T is a sampling period and transformation matrix $\boldsymbol{S}_{0e} = \mathrm{blockdiag}\{\boldsymbol{E}_3, \boldsymbol{S}_{\psi 0}, \boldsymbol{E}_3, \boldsymbol{E}_3\}$, where

$$\boldsymbol{S}_{\boldsymbol{\psi}_0} = \begin{bmatrix} \cos\psi_{p_0}\cos\psi_{p_0} & -\sin\psi_{y_0} & 0 \\ \cos\psi_{p_0}\sin\psi_{p_0} & \cos\psi_{y_0} & 0 \\ \sin\psi_{p_0} & 0 & 1 \end{bmatrix}.$$

Furthermore, $\boldsymbol{W}^{\#}$ is the pseudoinverse of $\boldsymbol{W}$, i.e. $\boldsymbol{W}^{\#} = \boldsymbol{W}^T(\boldsymbol{W}\boldsymbol{W}^T)^{-1}$.

From Equations (4.8), (4.9) and (4.10), if λ_i and γ_i are selected to satisfy $0 < \lambda_i < 1$ and $0 < \gamma_i < 1$, respectively, and the convergence of the acceleration error, $\boldsymbol{e}_\alpha(k) = \boldsymbol{\alpha}_s(k) - \boldsymbol{\alpha}(k)$, tends to zero as k tends to infinity, then the convergence of $\boldsymbol{e}_\nu(k)$ and $\boldsymbol{e}_x(k)$ to zero as k tends to infinity can be ensured.

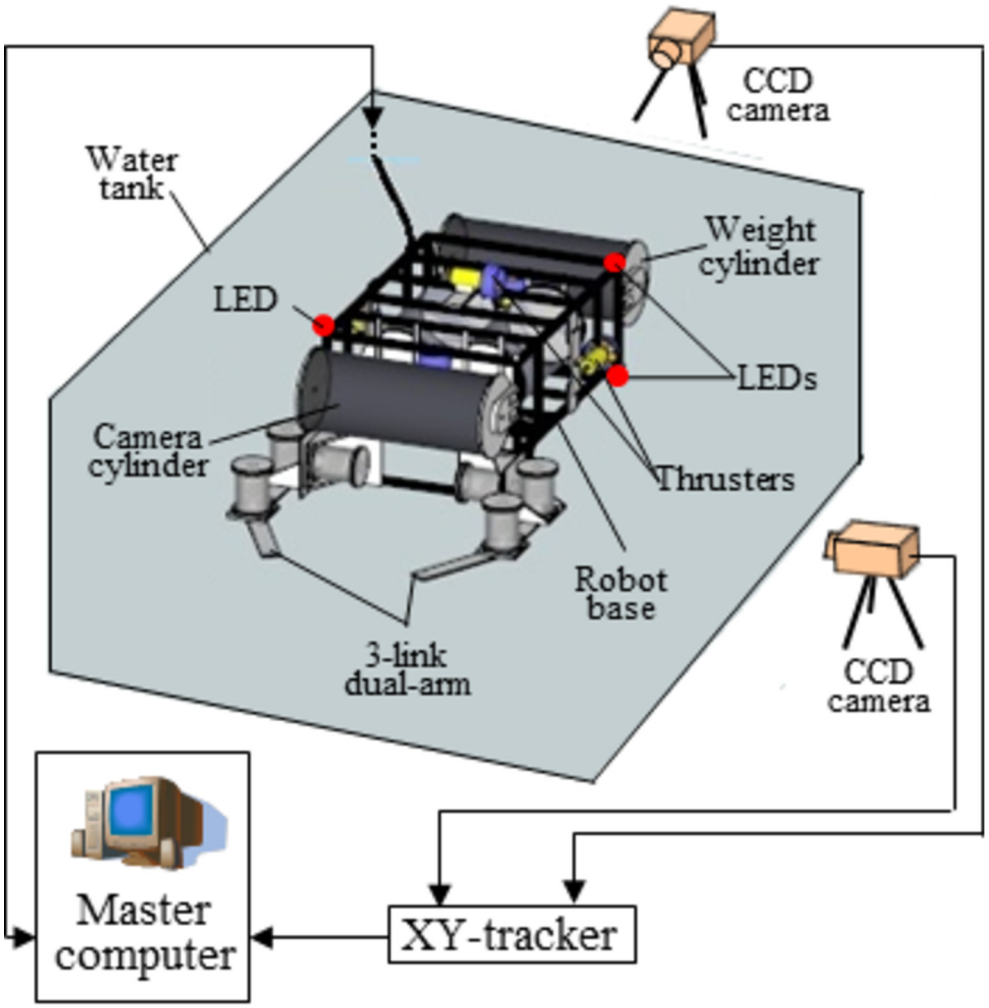

Fig. 4.6: Experimental setup

4.4 Experimental setup

Fig. 4.6 shows the experimental setup in this work. The setup is similar to the experimental setup for experimenting the effectiveness of RAC method using 2-link dual-arm UVMS described in section 3.5. The experiments were carried out in a water tank with a length of 2[m], width of 3[m] and depth of 2[m]. The water tank has glass windows on the front and side that enables researchers to view the condition of the UVMS during experiments. Fig. 4.7 shows an image of the actual 3-link dual-arm UVMS floating inside the water tank.

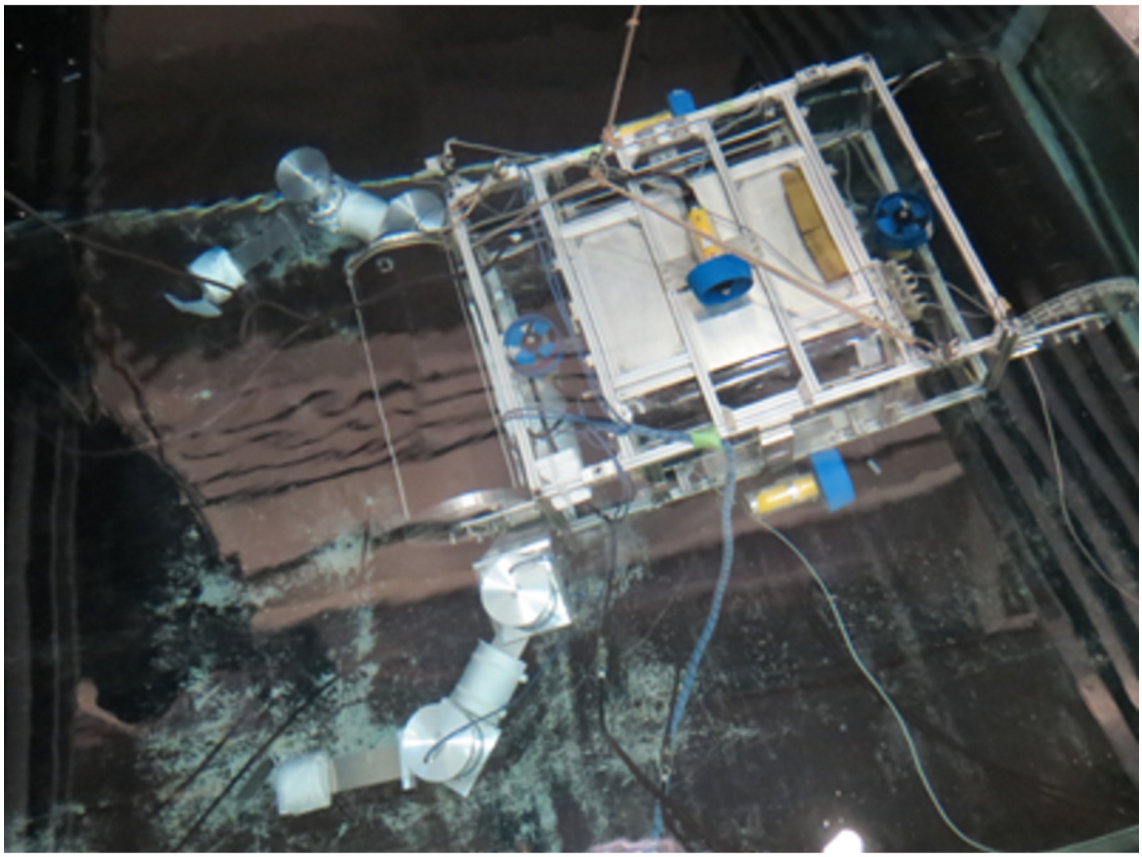

Fig. 4.7: 3-link dual-arm UVMS floating inside a water tank

4.5 Experimental conditions

There are two cases of experiments that were carried out in this work as shown in Fig. 4.8 and Fig. 4.9. The experiments were carried out under the following conditions. As the number of joints on each arm increased compared to the work done in Chapter 2, the amount of time needed for data transmission with all joints was also increased. Thus, in this work, the data sampling period was $T = 1/20$[s]. The robot base's maximum translational speed was set as 0.05[m/s], maximum rotational speed was $\pi/18$[rad/s], translational acceleration was 0.0083[m/s^2] and rotational acceleration was $\pi/72$[rad/s^2].

4.5.1 Case 1: Moving both end-tips to the desired positions

First, in case 1 shown in Fig. 4.8, both arms were controlled to move to the desired positions, as if it was reaching a target object in front of the robot. The desired end-tip positions were set up along a straight path from the initial positions to the desired positions. At the same time, the robot base was in station-keeping condition.

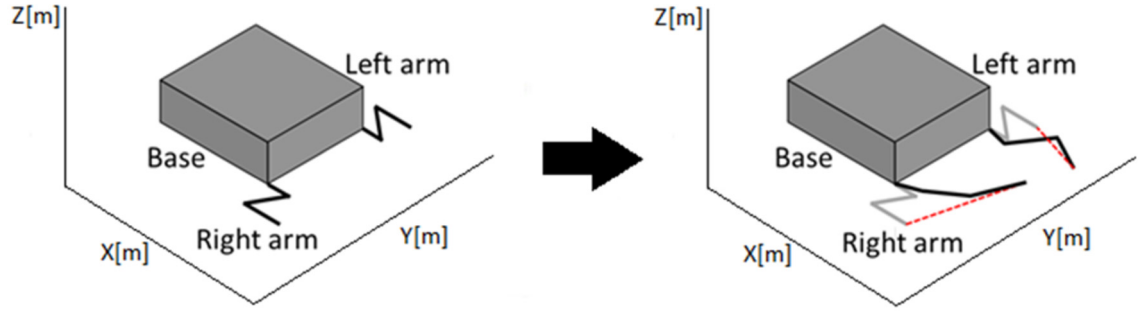

Fig. 4.8: Case 1: Moving both end-tips to desired positions. Initial position and attitude (left), and the desired position and attitude (right) of the robot and end-tips. Red dashed lines on animation (right) of both cases show the desired path of the end-tips

The initial position and attitude of the robot base were

$$\begin{aligned}&\text{initial position } [x,\ y,\ z][\text{m}] \ : \ [0,0,0][\text{m}],\\ &\text{initial attitude [roll, pitch, yaw][deg]} \ : \ [0,0,0][\text{deg}],\end{aligned}$$

and the initial angle ϕ_i^* for the first, second and third joints on both arms were

$$\begin{aligned}&\phi_1^{\mathrm{R}} = 0[\text{deg}], \quad \phi_2^{\mathrm{R}} = -100[\text{deg}], \quad \phi_3^{\mathrm{R}} = 100[\text{deg}],\\ &\phi_1^{\mathrm{L}} = 0[\text{deg}], \quad \phi_2^{\mathrm{L}} = 100[\text{deg}], \quad \phi_3^{\mathrm{L}} = -100[\text{deg}].\end{aligned}$$

As the robot base needed to be in station keeping condition during the experiment, the desired position and attitude of the robot base were the same as the initial position and attitude. However, the desired end-tip positions of both right and left manipulators were

$$\begin{aligned}&\text{right arm's end-tip} \ : \ [-0.2,-0.5,-0.3][\text{m}] \ \text{ from initial position,}\\ &\text{left arm's end-tip} \ : \ [-0.2,0.1,-0.2][\text{m}] \ \text{ from initial position.}\end{aligned}$$

The velocity error feedback gains $\boldsymbol{\Lambda}$ and position and attitude error feedback gains $\boldsymbol{\Gamma}$ for the robot base and manipulators were

$$\begin{aligned}\boldsymbol{\Lambda} &= \mathrm{diag}\left\{\Lambda_{bxyz}\ \Lambda_{brpy}\ \ \Lambda_{exyz}^{\mathrm{R}}\ \ \Lambda_{exyz}^{\mathrm{L}}\right\},\\ \boldsymbol{\Gamma} &= \mathrm{diag}\left\{\Gamma_{bxyz}\ \ \Gamma_{brpy}\ \ \Gamma_{exyz}^{\mathrm{R}}\ \ \Gamma_{exyz}^{\mathrm{L}}\right\},\end{aligned}$$

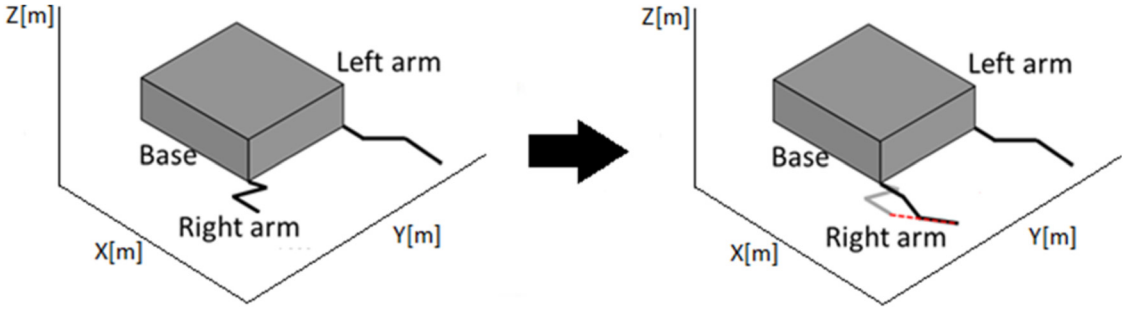

Fig. 4.9: Case 2: Moving right end-tip to a desired position, while maintaining left arm initial position. Initial position and attitude (left), and the desired position and attitude (right) of the robot and end-tips. Red dashed lines on animation (right) of both cases show the desired path of the end-tips

where

$$\Lambda_{bxyz} = \begin{bmatrix} 0.001 & 0 & 0 \\ 0 & 0.005 & 0 \\ 0 & 0 & 0.004 \end{bmatrix}, \quad \Lambda_{brpy} = \begin{bmatrix} 0.0025 & 0 & 0 \\ 0 & 0.004 & 0 \\ 0 & 0 & 0.005 \end{bmatrix},$$

$$\Lambda^R_{exyz} = \begin{bmatrix} 0.1 & 0 & 0 \\ 0 & 0.1 & 0 \\ 0 & 0 & 0.1 \end{bmatrix}, \quad \Lambda^L_{exyz} = \begin{bmatrix} 0.1 & 0 & 0 \\ 0 & 0.1 & 0 \\ 0 & 0 & 0.1 \end{bmatrix},$$

$$\Gamma_{bxyz} = \begin{bmatrix} 0.025 & 0 & 0 \\ 0 & 0.03 & 0 \\ 0 & 0 & 0.025 \end{bmatrix}, \quad \Gamma_{brpy} = \begin{bmatrix} 0.06 & 0 & 0 \\ 0 & 0.055 & 0 \\ 0 & 0 & 0.05 \end{bmatrix},$$

$$\Gamma^R_{exyz} = \begin{bmatrix} 0.06 & 0 & 0 \\ 0 & 0.06 & 0 \\ 0 & 0 & 0.06 \end{bmatrix}, \quad \Gamma^L_{exyz} = \begin{bmatrix} 0.06 & 0 & 0 \\ 0 & 0.06 & 0 \\ 0 & 0 & 0.06 \end{bmatrix}.$$

4.5.2 Case 2: Moving right end-tip to a desired position, while maintaining left arm initial position

Next, in case 2 shown in Fig. 4.9, while the left arm was holding its initial position, the right arm was controlled to move to a desired position, as if it was reaching a target object. The desired end-tip positions were set up along a straight path from the initial positions to the desired positions.

The initial position and attitude of the robot base were

$$\begin{aligned}&\text{initial position } [x,\ y,\ z][\text{m}] \ : \ [0,0,0][\text{m}],\\ &\text{initial attitude [roll, pitch, yaw][deg]} \ : \ [0,0,0][\text{deg}].\end{aligned}$$

The initial angle ϕ_i^* for the first, second and third joints on both arms were

$$\begin{aligned}\phi_1^{\mathrm{R}} = -30[\text{deg}], \quad \phi_2^{\mathrm{R}} = -100[\text{deg}], \quad \phi_3^{\mathrm{R}} = 100[\text{deg}],\\ \phi_1^{\mathrm{L}} = 0[\text{deg}], \quad \phi_2^{\mathrm{L}} = 45[\text{deg}], \quad \phi_3^{\mathrm{L}} = -60[\text{deg}].\end{aligned}$$

As the robot base needed to be in station keeping condition during the experiment, the desired position and attitude of the robot base were the same as the initial position and attitude. However, desired end-tip positions of both right and left arm's end-tips were

$$\begin{aligned}&\text{right arm's end-tip} \ : \ [-0.3,-0.3,-0.3][\text{m}] \ \text{ from initial position},\\ &\text{left arm's end-tip} \ : \ [0,0,0][\text{m}] \ \text{ from initial position}.\end{aligned}$$

Here, the movements of both end-tips are set up along a straight path from the initial positions to the desired positions. The data sampling period was $T = 1/20[\text{s}]$.

The velocity error feedback gains $\boldsymbol{\Lambda}$ and position and attitude error feedback gains $\boldsymbol{\Gamma}$ for the robot base and both arm's end-tips were

$$\begin{aligned}\boldsymbol{\Lambda} &= \mathrm{diag}\left\{\Lambda_{bxyz}\ \Lambda_{brpy}\ \ \Lambda_{exyz}^{\mathrm{R}}\ \ \Lambda_{exyz}^{\mathrm{L}}\right\},\\ \boldsymbol{\Gamma} &= \mathrm{diag}\left\{\Gamma_{bxyz}\ \ \Gamma_{brpy}\ \ \Gamma_{exyz}^{\mathrm{R}}\ \ \Gamma_{exyz}^{\mathrm{L}}\right\},\end{aligned}$$

where

$$\Lambda_{bxyz} = \begin{bmatrix}0.001 & 0 & 0\\ 0 & 0.005 & 0\\ 0 & 0 & 0.004\end{bmatrix}, \quad \Lambda_{brpy} = \begin{bmatrix}0.0025 & 0 & 0\\ 0 & 0.004 & 0\\ 0 & 0 & 0.005\end{bmatrix},$$

$$\Lambda_{exyz}^{R} = \begin{bmatrix}0.1 & 0 & 0\\ 0 & 0.1 & 0\\ 0 & 0 & 0.1\end{bmatrix}, \quad \Lambda_{exyz}^{L} = \begin{bmatrix}0.1 & 0 & 0\\ 0 & 0.1 & 0\\ 0 & 0 & 0.1\end{bmatrix},$$

$$\Gamma_{bxyz} = \begin{bmatrix}0.025 & 0 & 0\\ 0 & 0.03 & 0\\ 0 & 0 & 0.025\end{bmatrix}, \quad \Gamma_{brpy} = \begin{bmatrix}0.06 & 0 & 0\\ 0 & 0.055 & 0\\ 0 & 0 & 0.05\end{bmatrix},$$

$$\Gamma_{exyz}^{R} = \begin{bmatrix}0.06 & 0 & 0\\ 0 & 0.06 & 0\\ 0 & 0 & 0.06\end{bmatrix}, \quad \Gamma_{exyz}^{L} = \begin{bmatrix}0.06 & 0 & 0\\ 0 & 0.06 & 0\\ 0 & 0 & 0.06\end{bmatrix}.$$

4.6 Experimental results and discussions

This section presents the results from the coordinated motion control of an AUV and 3-link dual-arm experiments based on the two cases described in the previous section.

Case 1 results. Fig. 4.10 to Fig. 4.18 show the results related to the experiments for case 1 where both arms were controlled to move to the desired positions simultaneously.

Firstly, Fig. 4.10(a) and (b) show time histories of the robot base position and attitude errors during the motions of both arms towards the desired positions. From both figures, it can be seen that the robot base was clearly excited by the movements of both arms. In Fig. 4.10(a), the robot base position on x, y and z directions were clearly excited due to arms motion in the first 20[s] of the experiment. As the arm's reached the desired positions, the errors gradually decreased and stabilized after 20[s]. Similarly, the attitude of the robot base was also excited especially in the yaw angle as shown in Fig. 4.10(b). It can be seen from the result that the motions of the arms excited the robot base especially the yaw and pitch angles at the first 5[s] of the experiments. Moreover, even after 5[s], significantly larger error in yaw can be observed. The robot base drifted about 8[rad] in yaw before the robot thrusters were able to control the motion. These figures demonstrate that the motions of both arms have significant effect by destabilizing the motion of the robot base. Fig. 4.11 show the actual position and attitude during the arm's motions. Fig. 4.12 show the thruster's control inputs to produce the thrust forces that were required to counteract the forces generated from both arm movements.

The time history of the positions of the end-tips of both left and right arms moving from the initial positions to the desired positions are shown in Fig. 4.13 and Fig. 4.14, respectively. In this case, to demonstrate the performance of the proposed RAC method, both arms were controlled to move from the initial positions to the desired positions in 3-dimensional space (x, y and z directions) as shown in the figures. Both figures show that the right and left arm's end-tips reached the desired positions after about 15[s] and 10[s], respectively, from the start of the experiment.

Fig. 4.15 and Fig. 4.16 show the results of the end-tips position errors for both right and left arm during the motions toward the desired positions. It can be seen in the figures that the motions of both end-tips were excited within the early 20[s] of the experiment, which correspond to the actual position and attitude motions of the robot base as shown in Fig. 4.11. However, the excitation of both arms motions due to the motions of robot base were considerably reduced soon after it reached the desired positions. Moreover, although the robot base was significantly excited especially the attitude motions, the position error of the end-tips were successfully reduced to within ± 0.02[m]. Fig. 4.17 and Fig. 4.18 show the control input for the right arm and left arm joints. In this work, the arm joints required velocity input rather than position input in order to move the actuators. By using velocity input, the errors while calculating the desired acceleration can be reduced. Based on these results, the RAC method demonstrated good performance by showing that even though the robot base motions was under the influence of hydrodynamic forces due

to the coupled effects of robot base and dual-arm, both end-tips were able to follow the desired trajectories to reach the desired positions.

Case 2 results. Fig. 4.19 to Fig. 4.27 show the results related to the experiments for case 2. In this case, the performance of the proposed RAC method is tested based on a much more complicated motions of both arms. As explained in the subsection 4.5.2, in this case, while the left arm was holding its initial position, the right arm was controlled to move to a desired position, as if it was reaching a target object. At the same time, the AUV retains its initial position.

Firstly, Fig. 4.19(a) and (b) show the time histories of the position and attitude errors of the robot base. Fig. 4.20 show the actual position and attitude of the robot base during the arm's motions. These figures show that the robot base was clearly excited by the movements of both arms. The robot base was drifted in x and y directions and maintained about ± 0.02[m] and ± 0.05[m], respectively, from the initial position. This means that the robot base was drifting towards the left and front directions at the same time due to the effect of the right arm's motion. Fig. 4.21 show the thruster's control inputs to produce the thrust forces that were required to counteract the forces generated from both arm movements.

Next, Fig. 4.22 and Fig. 4.23 show the time histories of the actual positions of the end-tips of both left and right arms in 3-dimensional space, respectively. Fig. 4.22 shows that the right arm's end-tip was controlled to move to a desired position. The end-tips of the right arm reached the desired final position after 15[s]. On the other hand, Fig. 4.23 shows that the left arm was controlled to keep the initial position. In a real world intervention task, this case can be imagined as if the left arm is gripping on a fixed base, while the right arm reaching a target object.

Fig. 4.24 and Fig. 4.25 show the results of the end-tips position errors for both right and left arm during the experiment. It can be seen that similar to the motions of the robot base, both end-tips were excited within the early 20[s] of the experiment, and significantly reduced within ± 0.01[m] after reaching the desired position. Fig. 4.24 shows that the right arm was excited due to the effect of the robot base's motions, especially on the x and y directions which is similar to the motions of the robot base as shown in Fig. 4.11(a). However, the left arm only demonstrated small excitation on z direction in the first 5[s] of the experiment as shown in Fig. 4.25(c). After that, the left arm showed good performance in keeping the initial position until the end of experiment. Fig. 4.26 and Fig. 4.27 show the control input for the right arm and left arm joints. Based on these results, the RAC method demonstrated good performance by showing that even though the robot base motions was under the influence of hydrodynamic forces due to the coupled effects of robot base and dual-arm, the left arm was successfully controlled to keep its position and the right arm end-tips were able to follow the desired trajectory to reach the desired position.

4.7 Conclusions

In this chapter, coordinated motion control of an underwater vehicle equipped with 3-link dual-arm using Resolved Acceleration Control (RAC) method have been demonstrated. Based on two cases of experiment results, the proposed method was able to provide good control performances of the arm's end-tips to follow the pre-planned trajectories, in spite of hydrodynamic forces due to the coupled effects of robot base and dual-arm, and large position and attitude errors of the underwater vehicle. Compared to the experiments using 2-link dual-arm UVMS, by using 3-link dual-arm UVMS, it was possible to simultaneously control the end-tips to different desired positions within x-y, x-z or y-z planes. Moreover, the RAC method showed better control performances of the end-tips by utilizing servo motors with larger torque and the ability to be controlled using velocity control, compared to the results that utilized smaller torque with position control as shown in Fig. 3.14 in Chapter 3.

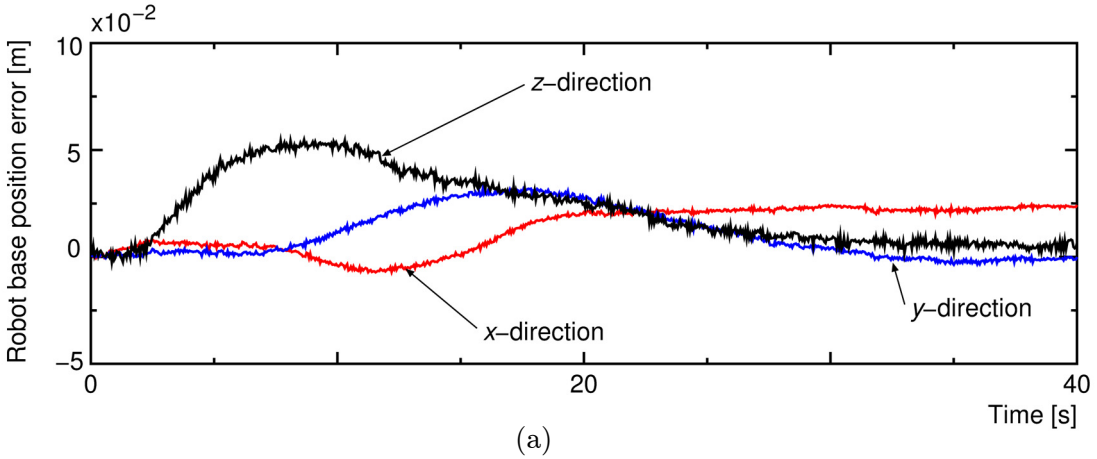

(a)

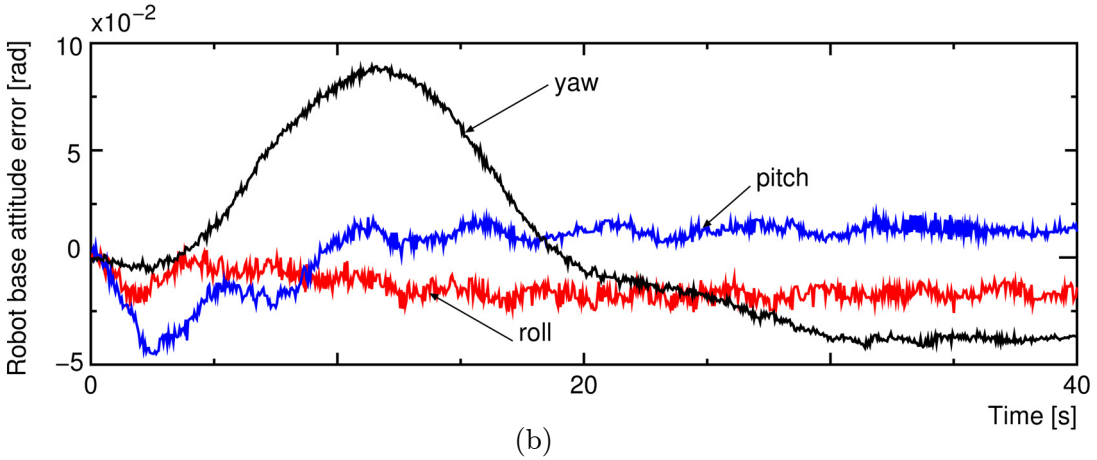

(b)

Fig. 4.10: Experimental results for case 1: Robot base position and attitude errors

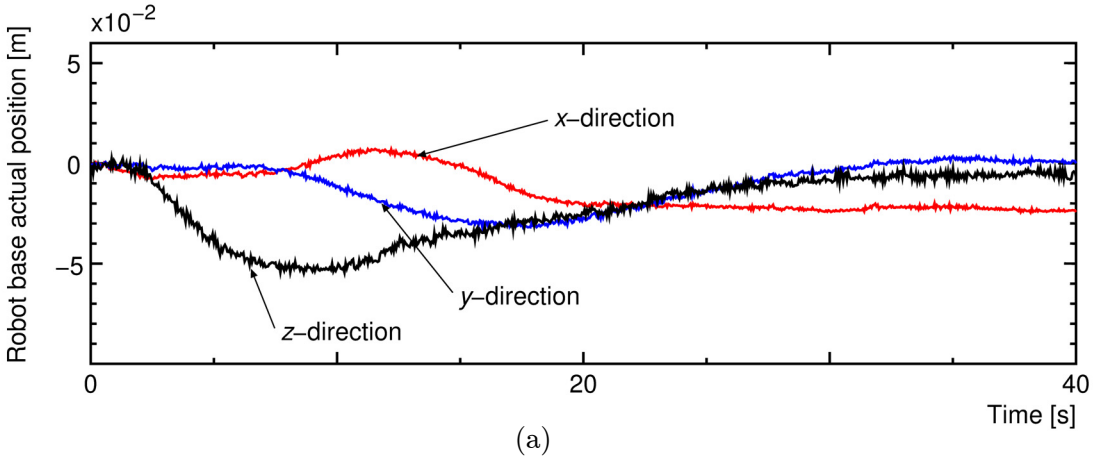

(a)

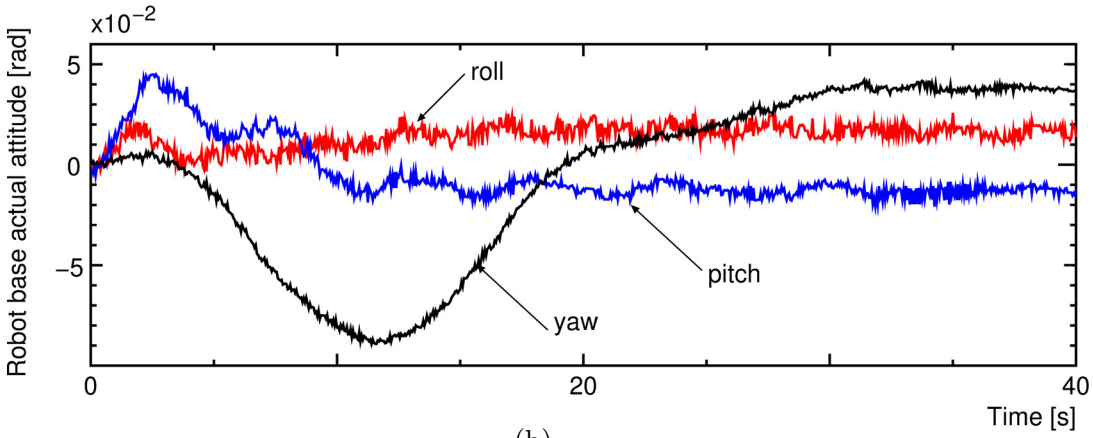

(b)

Fig. 4.11: Experimental results for case 1: Robot base actual position and attitude

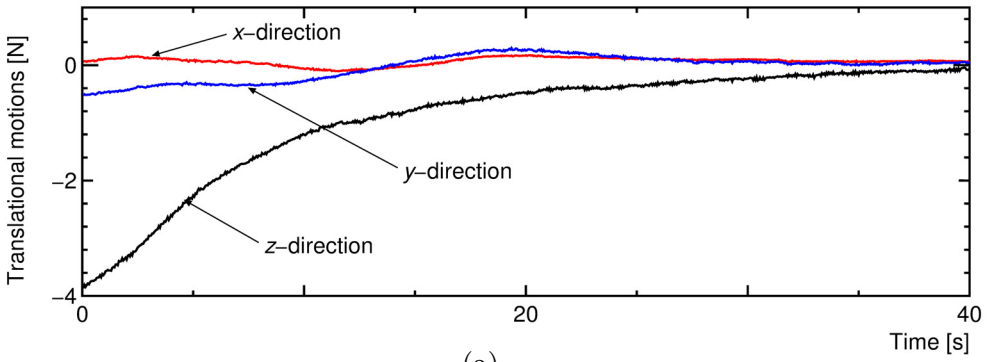

(a)

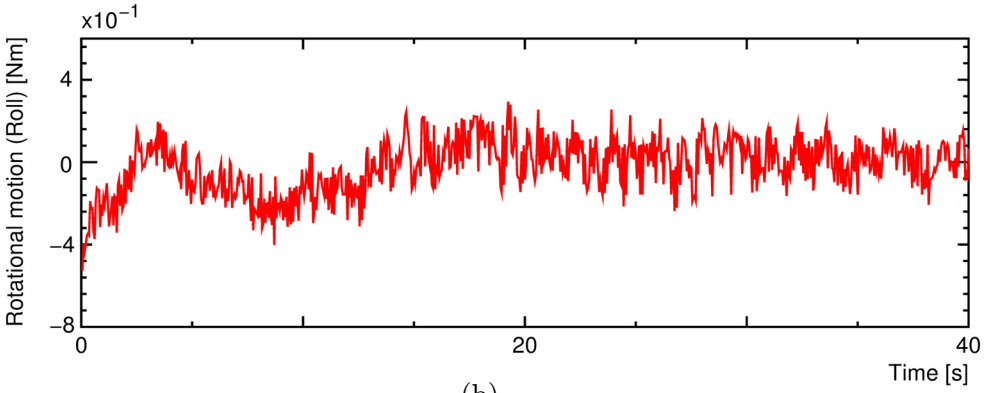

(b)

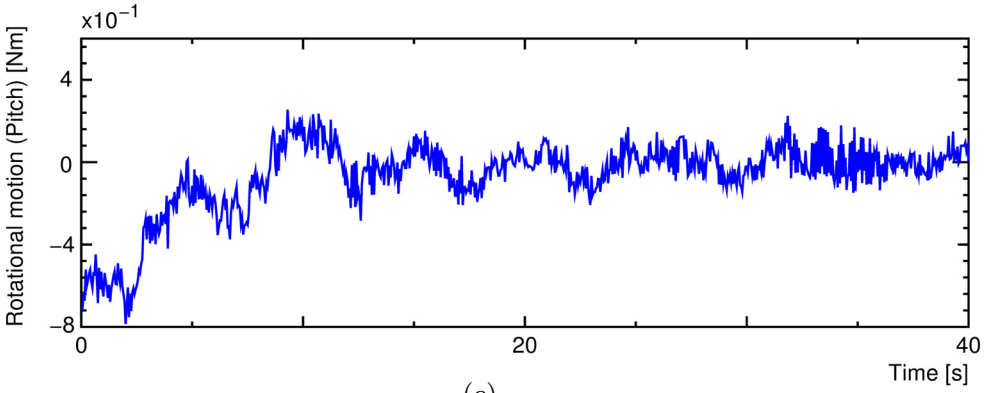

(c)

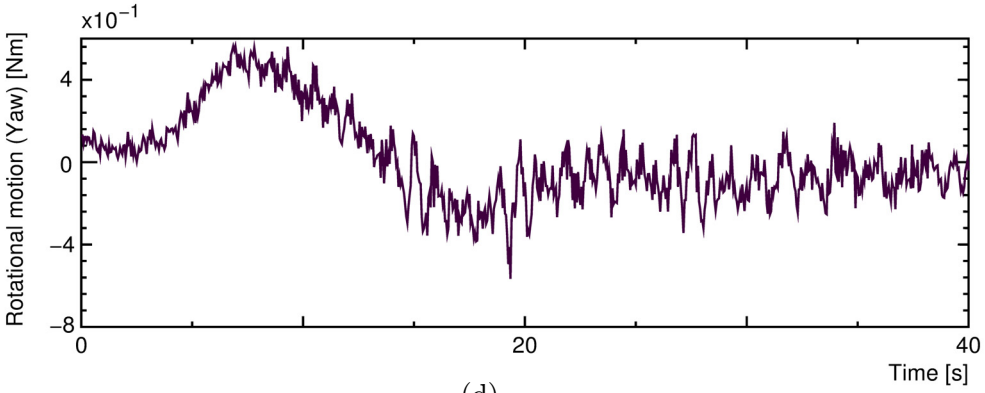

(d)

Fig. 4.12: Experimental results for case 1: Control inputs for robot base

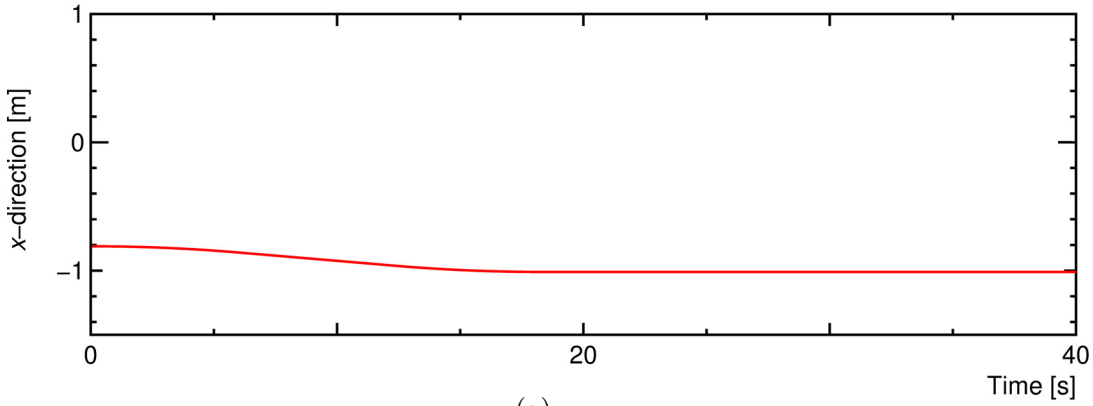

(a)

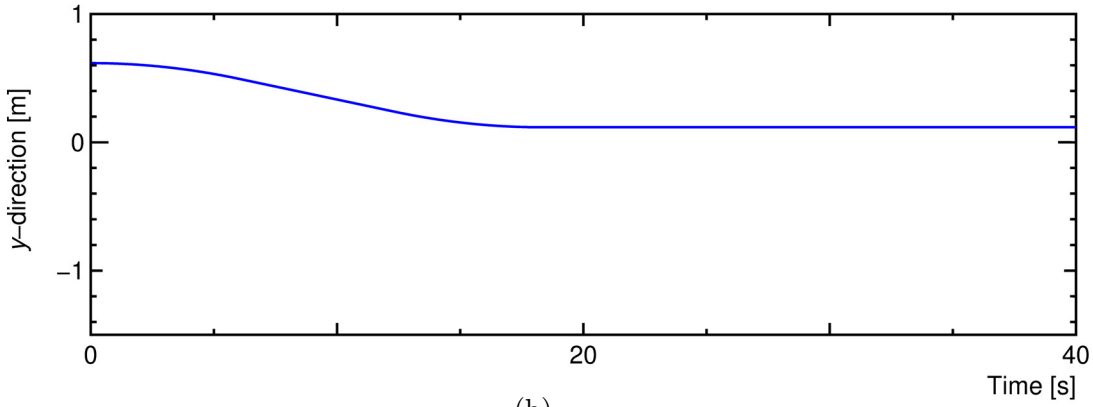

(b)

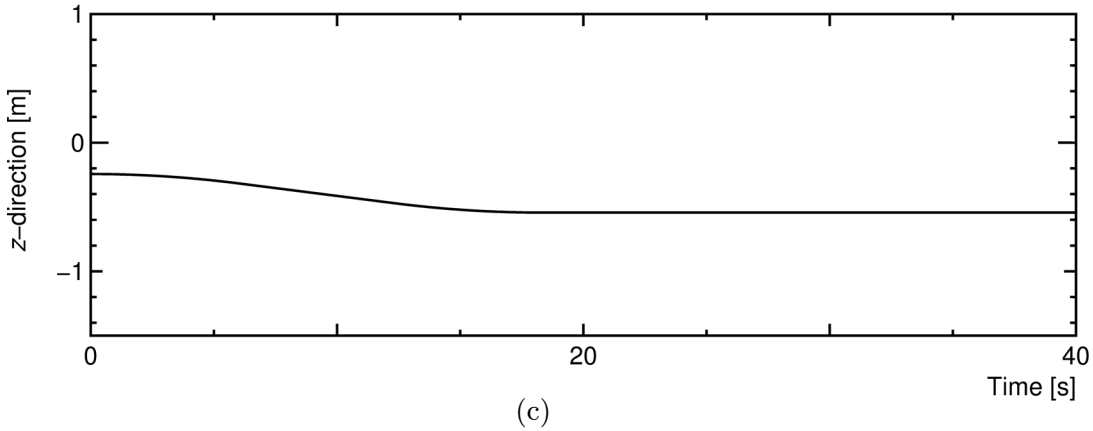

(c)

Fig. 4.13: Experimental results for case 1: Desired end-tip position for the right arm

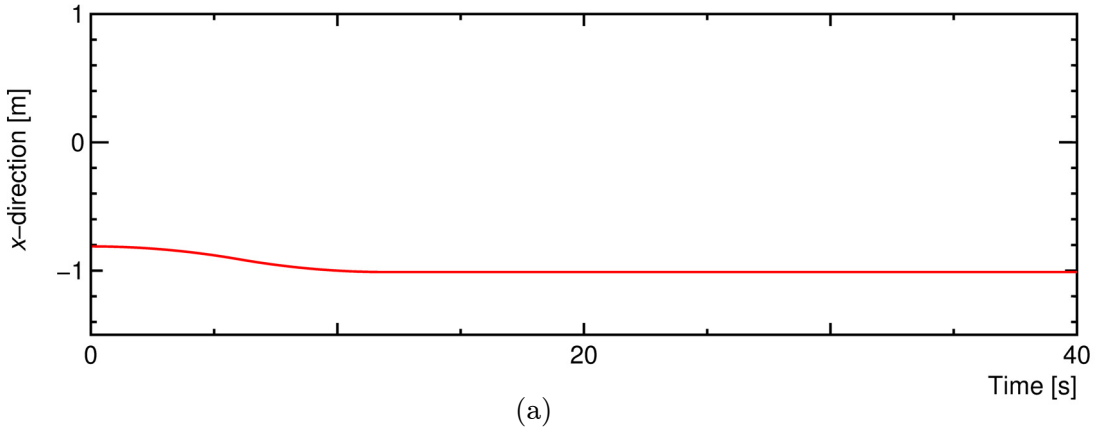

(a)

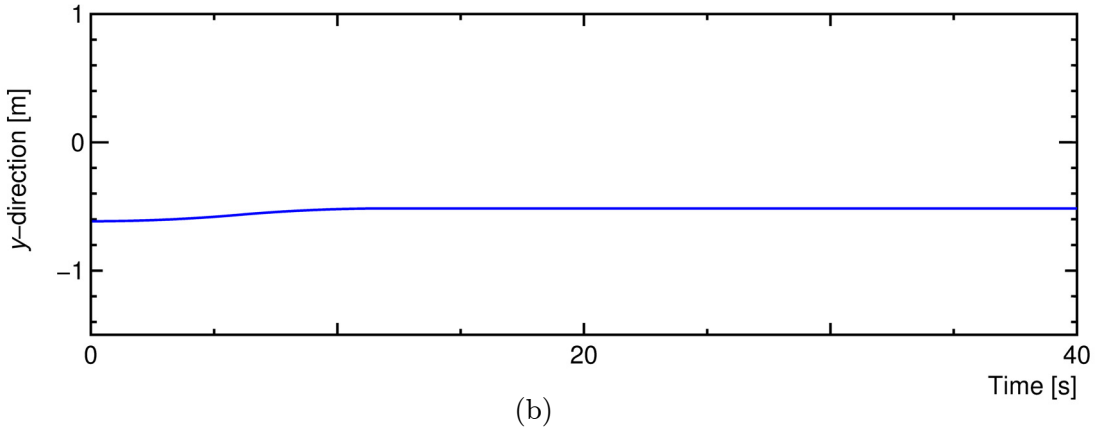

(b)

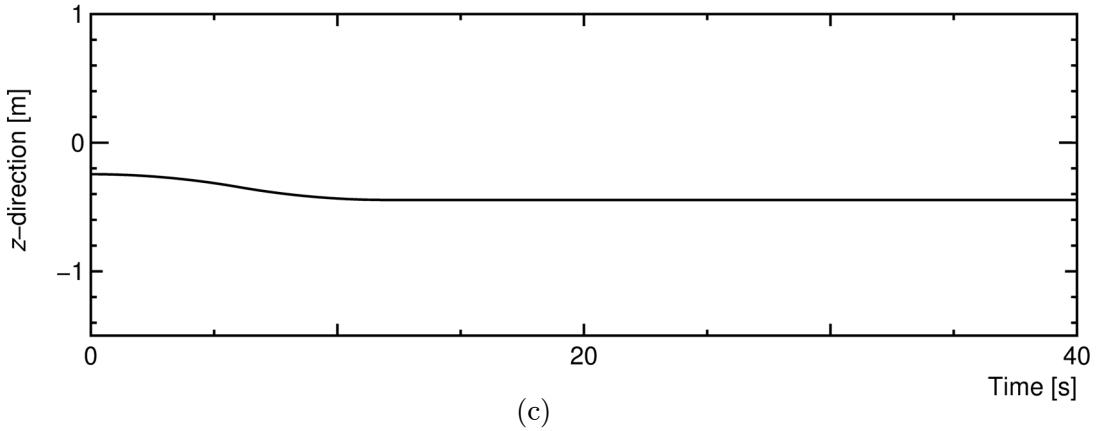

(c)

Fig. 4.14: Experimental results for case 1: Desired end-tip position for the left arm

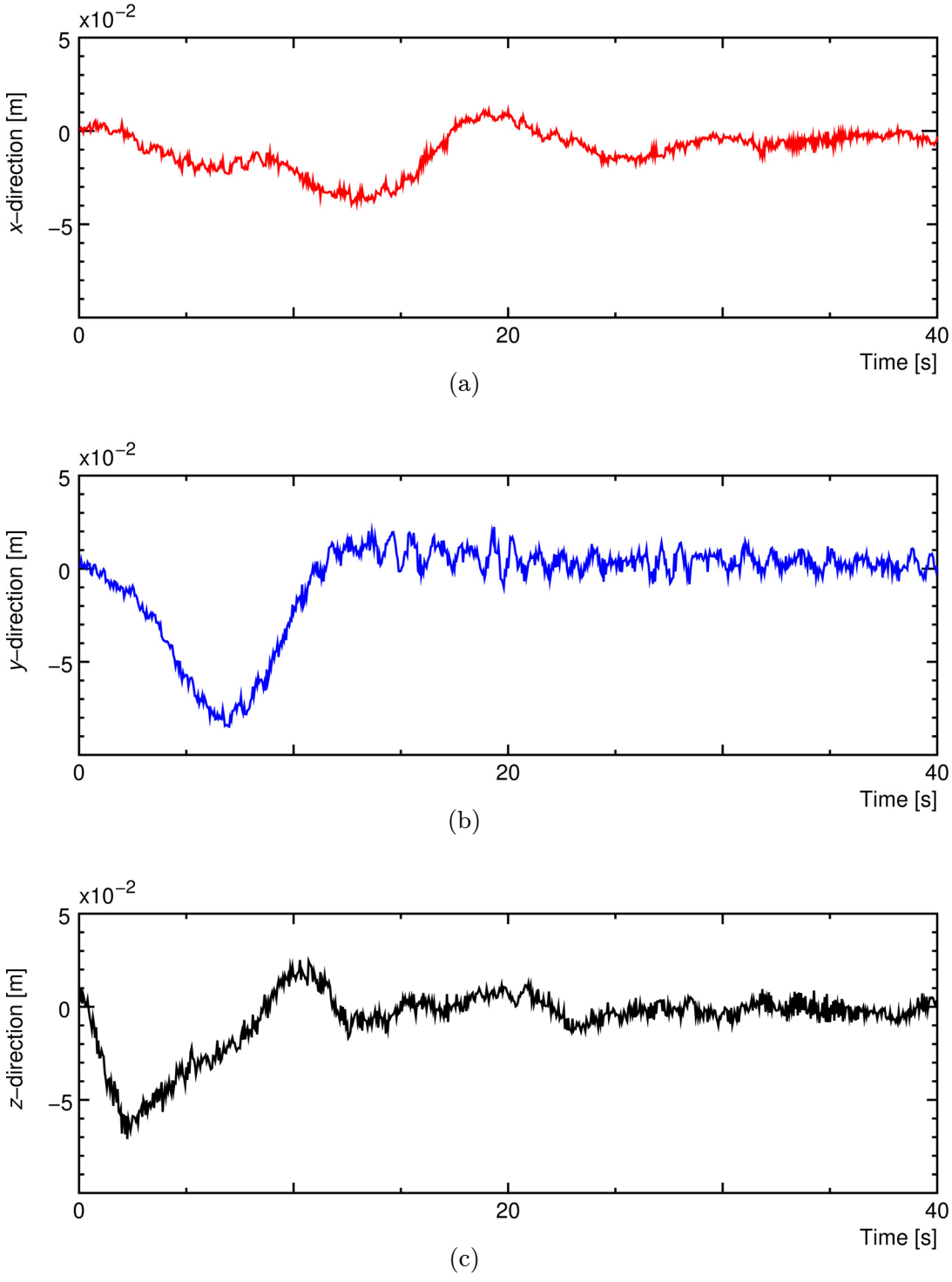

Fig. 4.15: Experimental results for case 1: Position error for right arm's end-tip

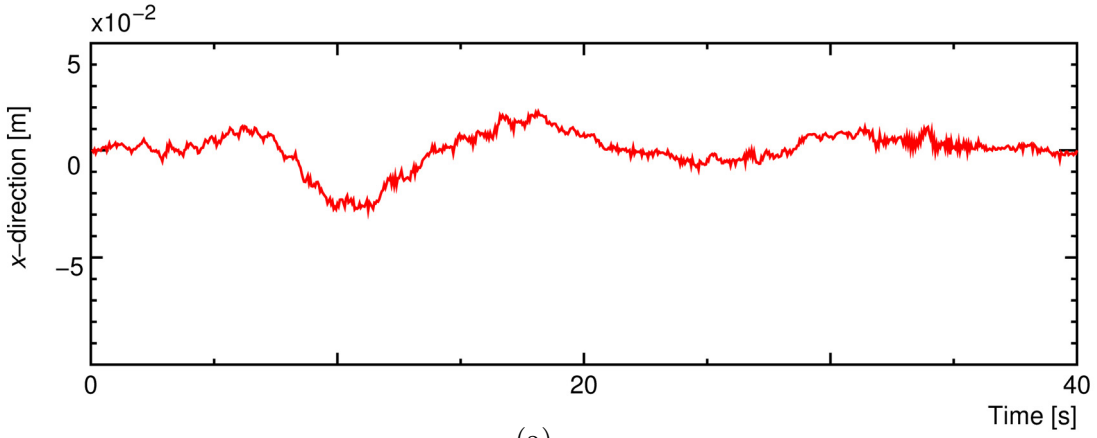

(a)

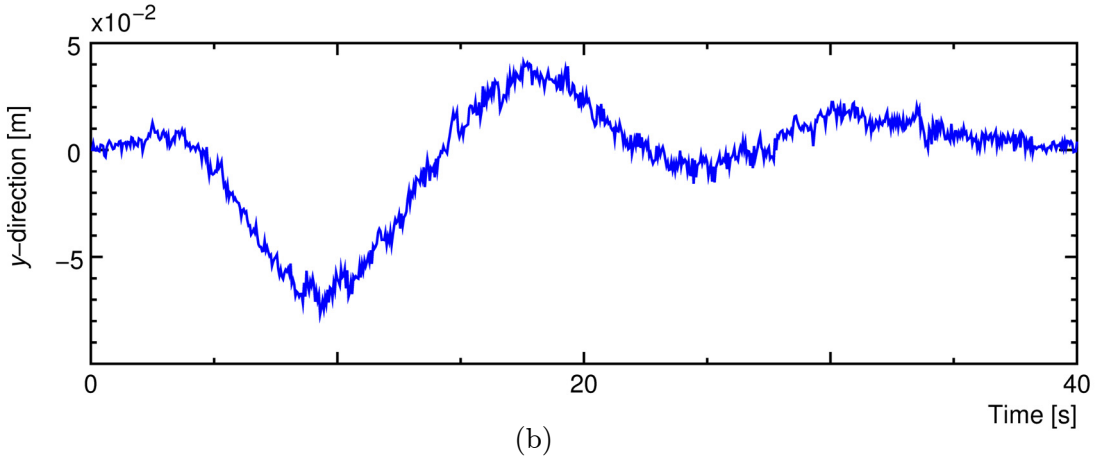

(b)

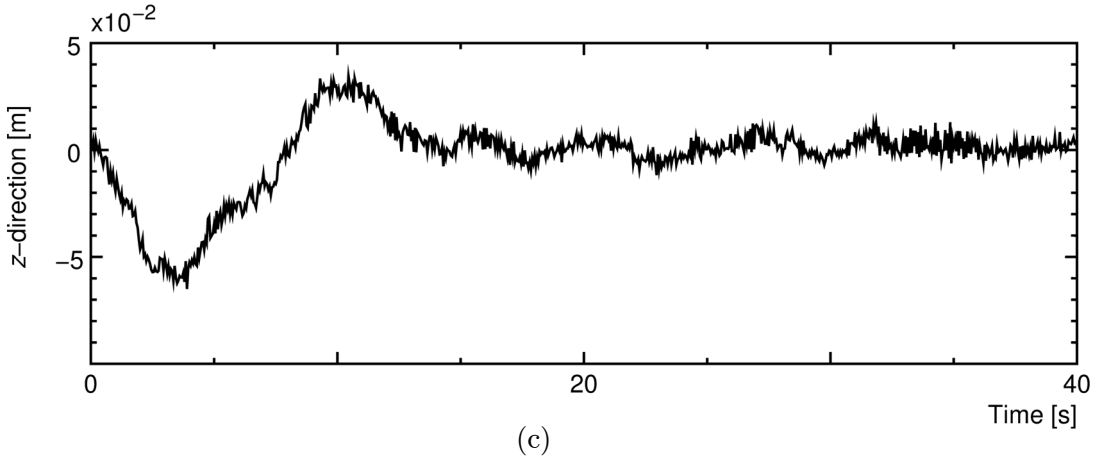

(c)

Fig. 4.16: Experimental results for case 1: Position error for left arm's end-tip

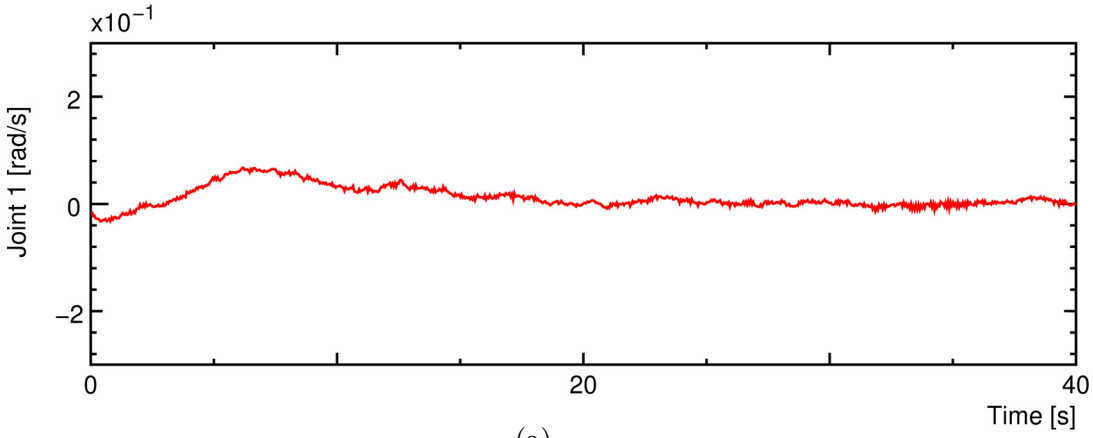

(a)

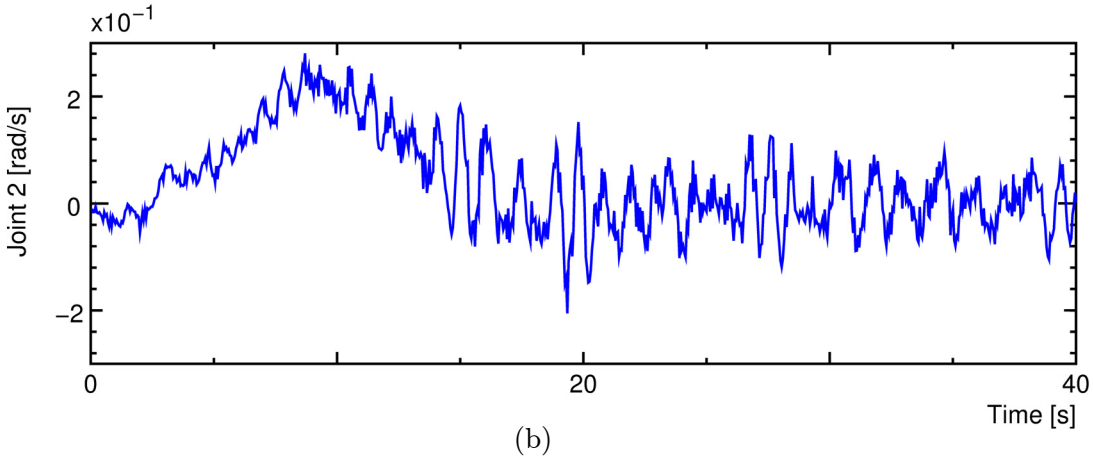

(b)

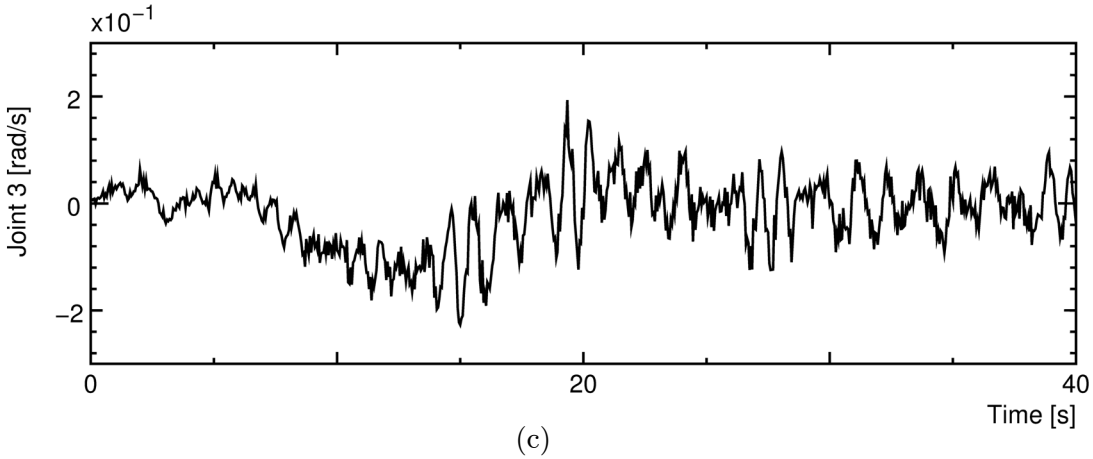

(c)

Fig. 4.17: Experimental results for case 1: Control inputs for right arm's joints

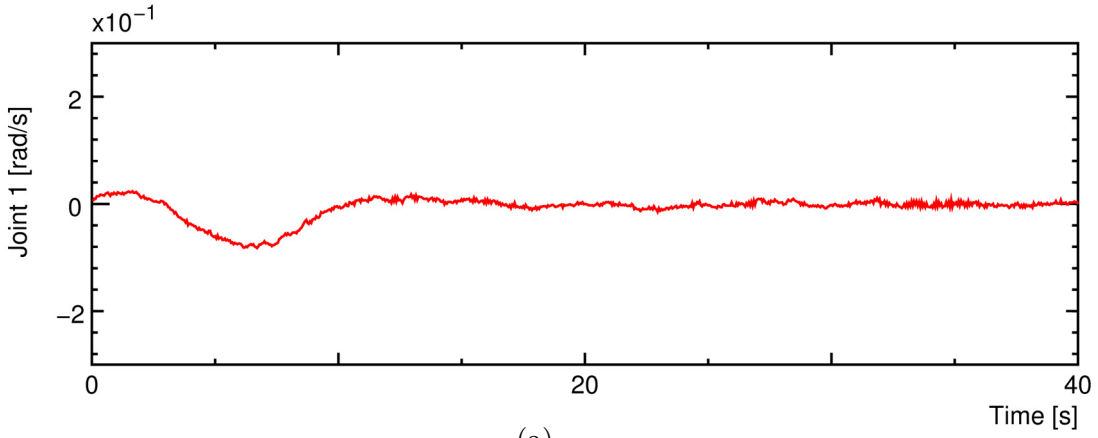

(a)

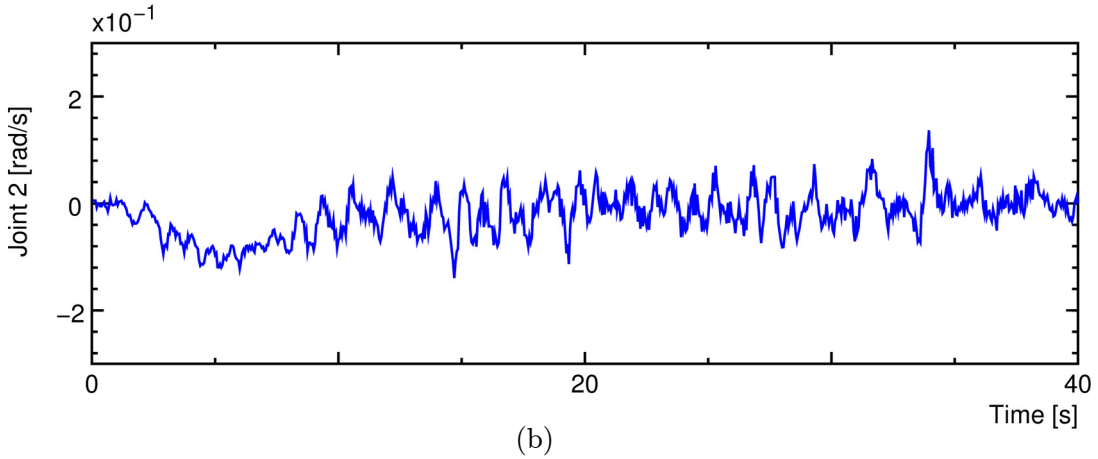

(b)

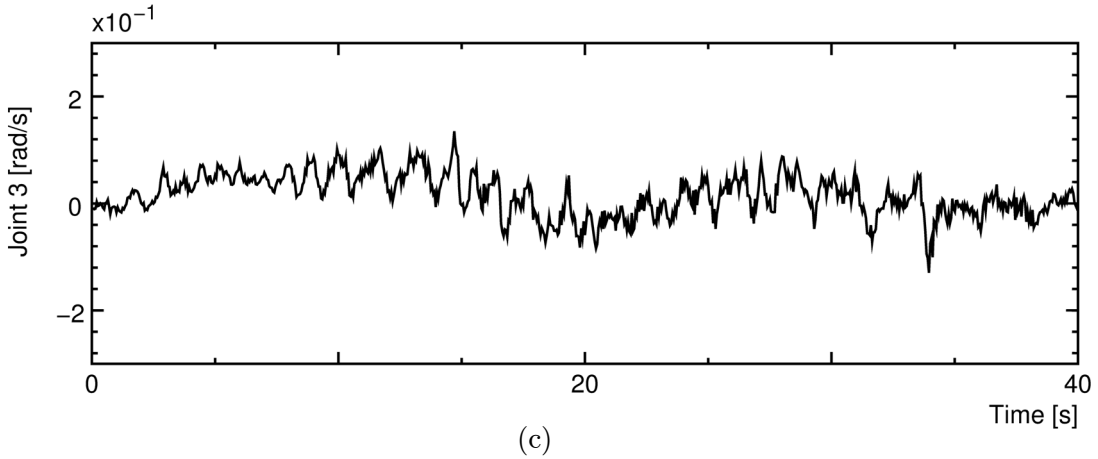

(c)

Fig. 4.18: Experimental results for case 1: Control inputs for left arm's joints

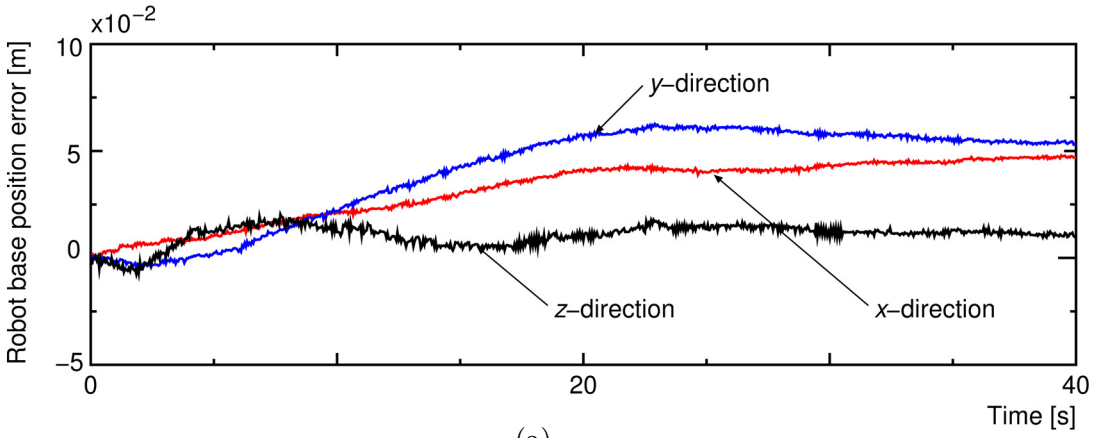

(a)

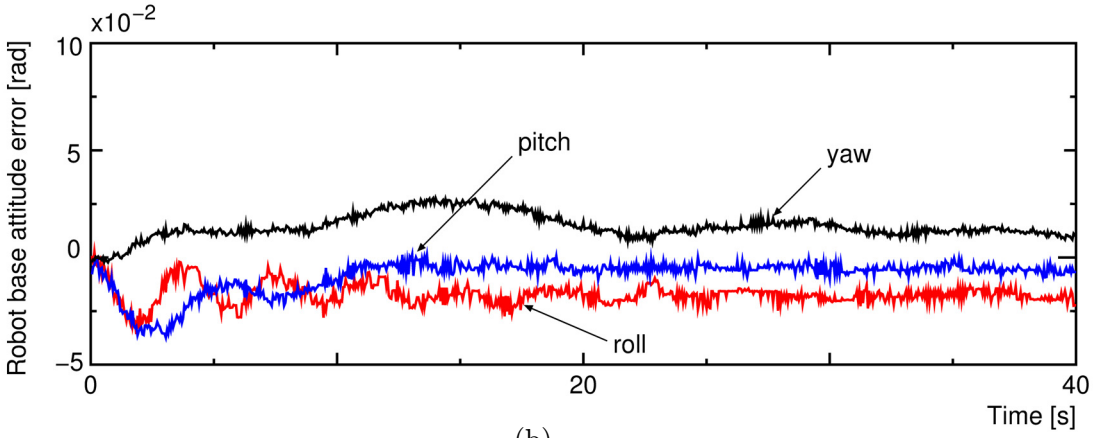

(b)

Fig. 4.19: Experimental results for case 2: Robot base position and attitude errors

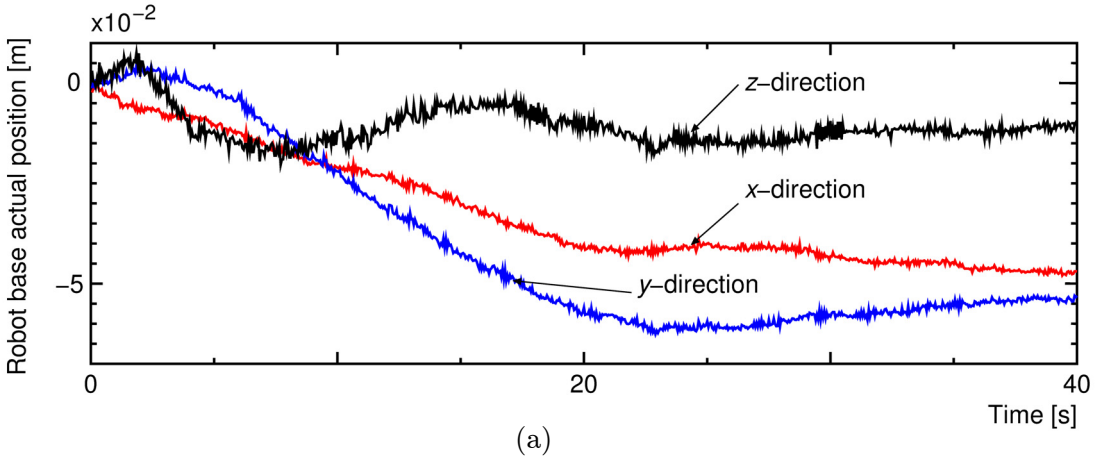

(a)

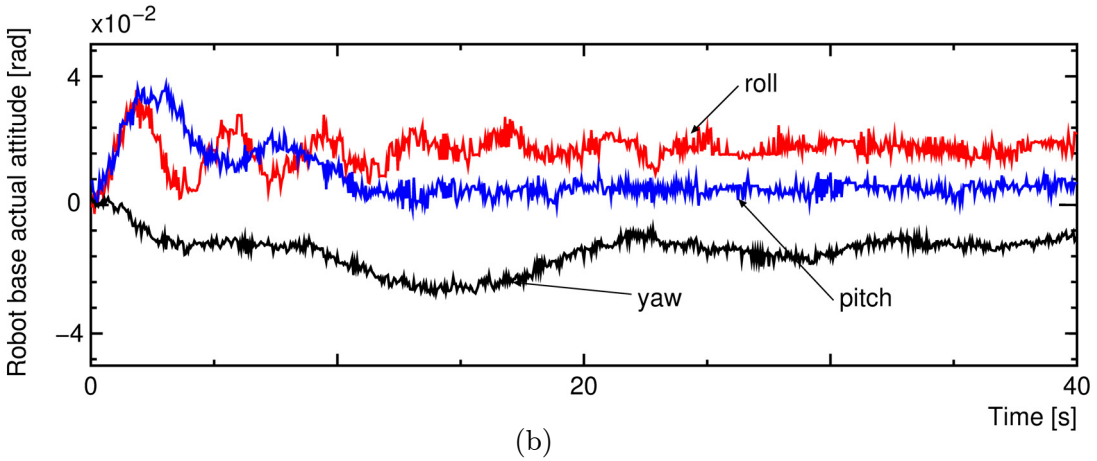

(b)

Fig. 4.20: Experimental results for case 2: Robot base actual position and attitude

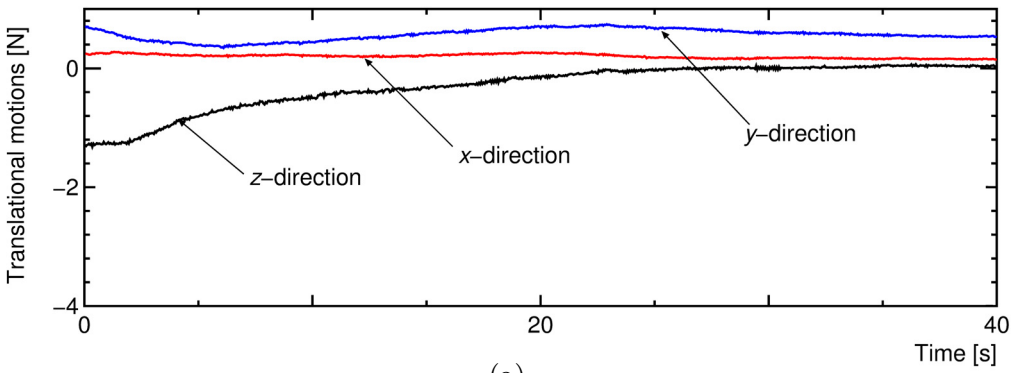

(a)

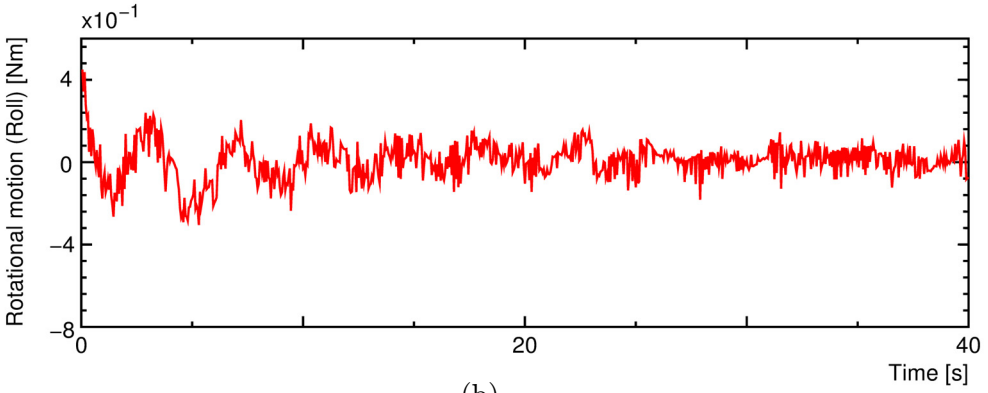

(b)

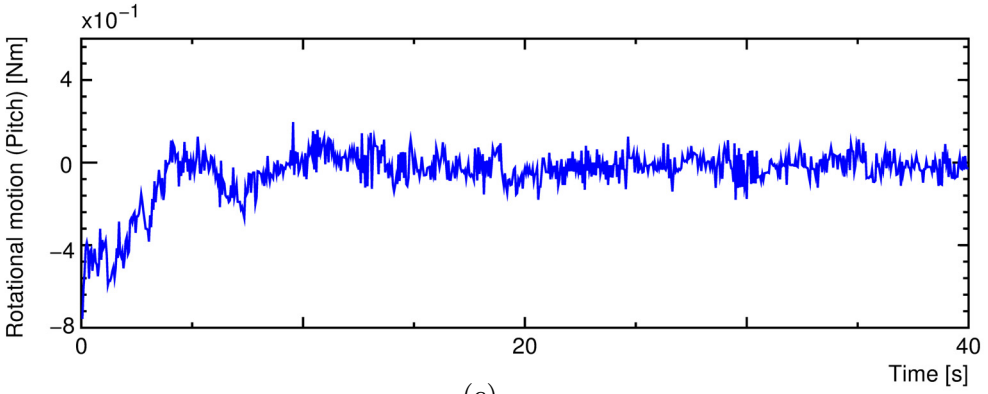

(c)

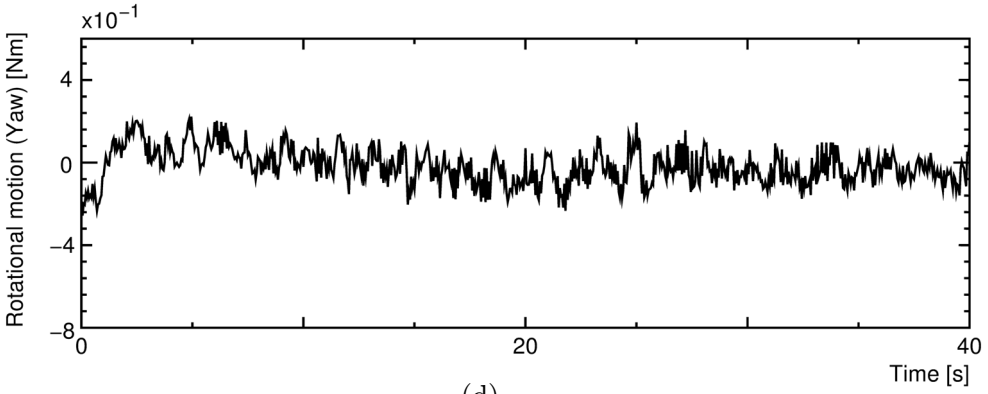

(d)

Fig. 4.21: Experimental results for case 2: Control inputs for robot base

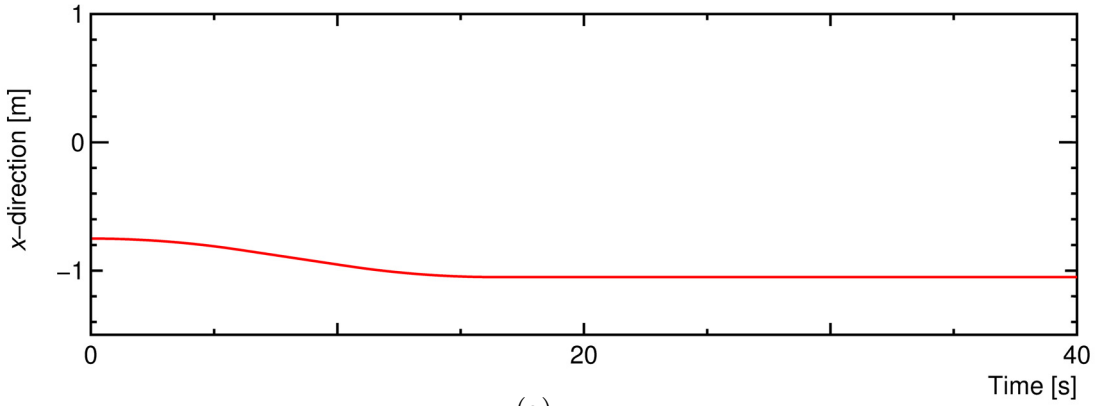

(a)

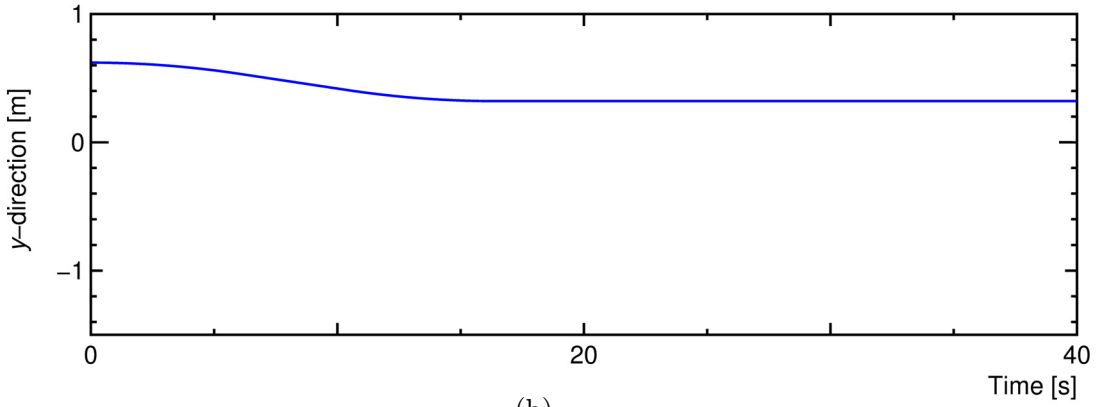

(b)

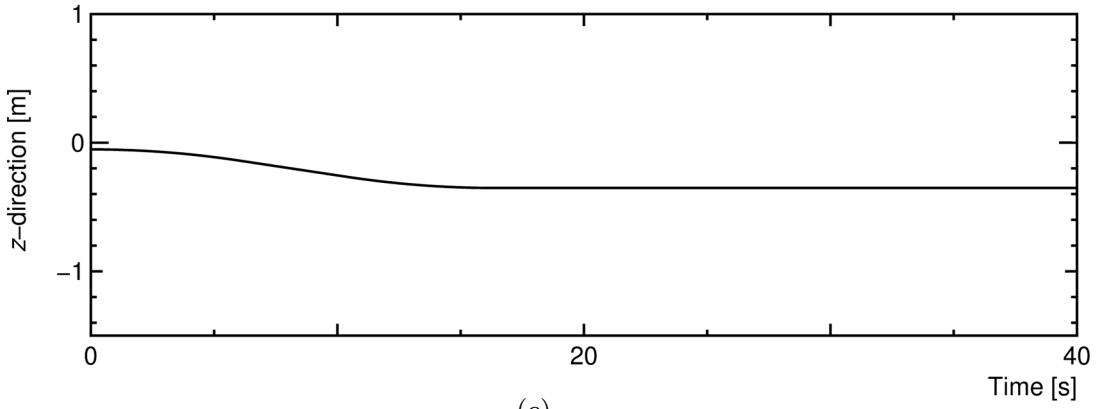

(c)

Fig. 4.22: Experimental results for case 2: Desired end-tip position for the right arm

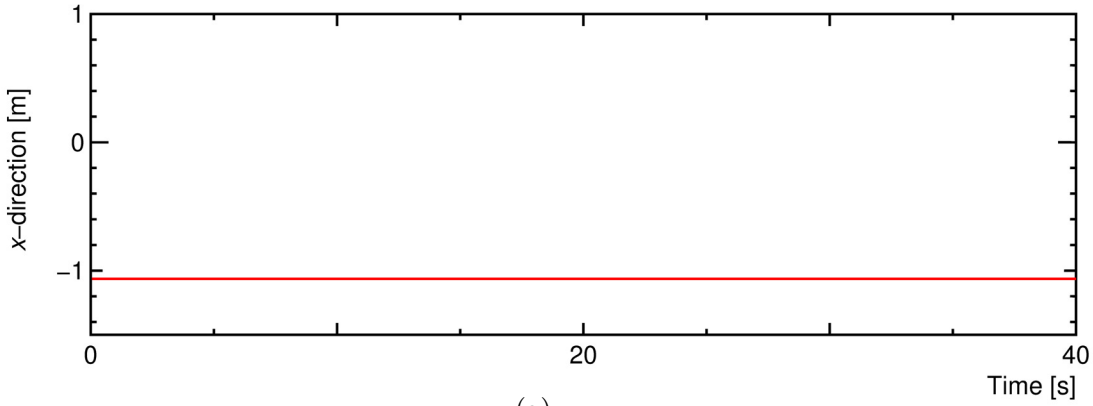

(a)

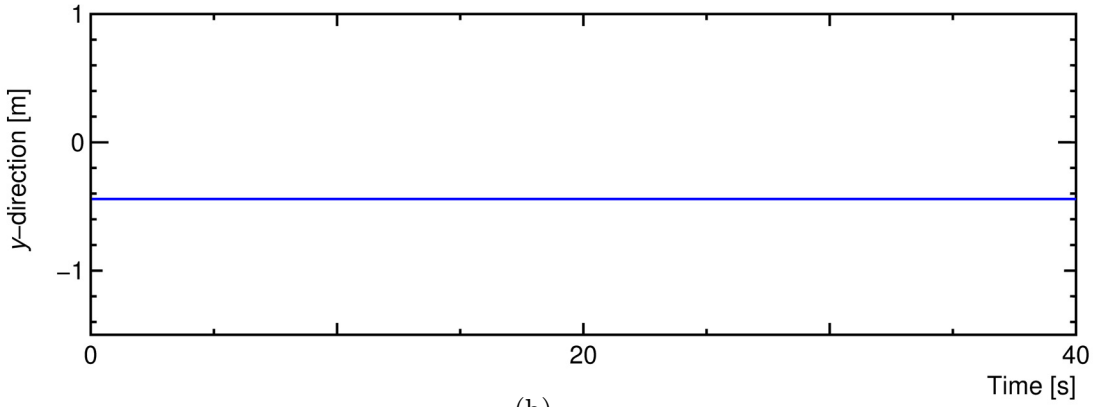

(b)

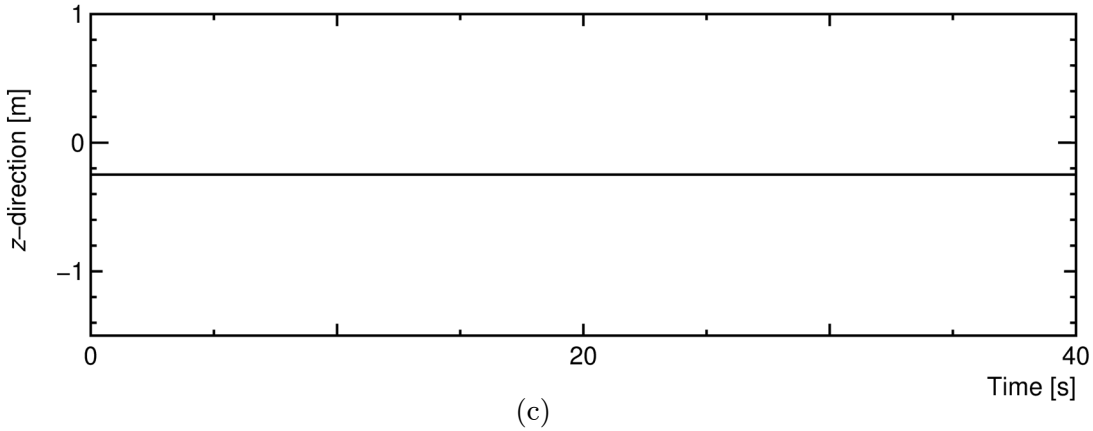

(c)

Fig. 4.23: Experimental results for case 2: Desired end-tip position for the left arm

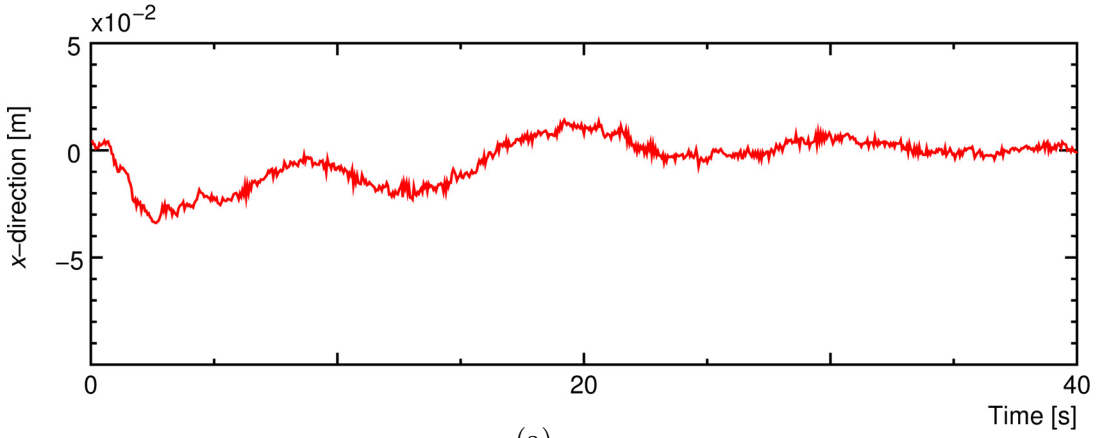

(a)

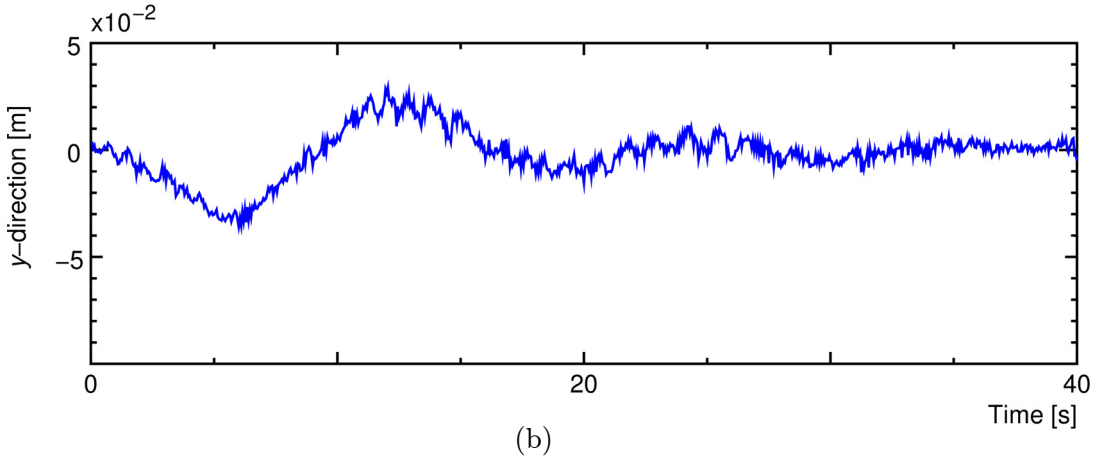

(b)

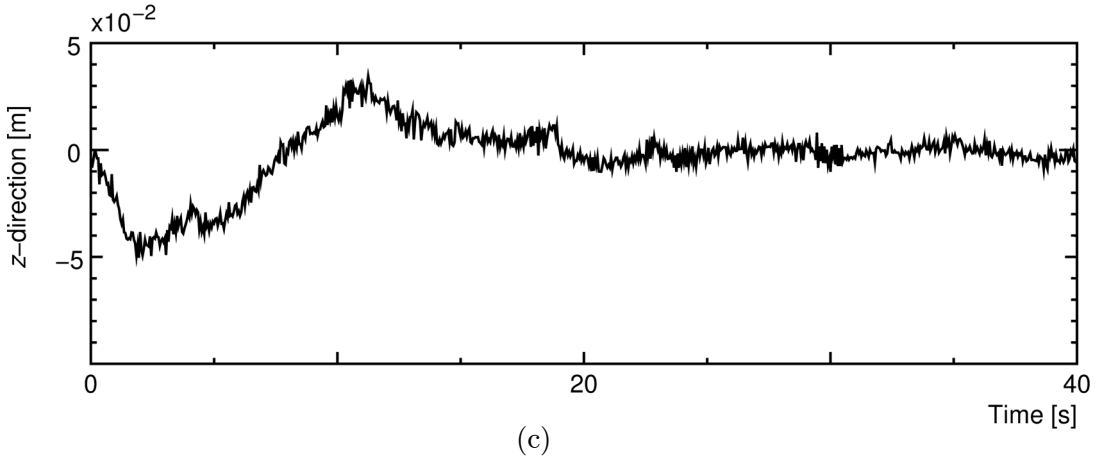

(c)

Fig. 4.24: Experimental results for case 2: Position error for right arm's end-tip

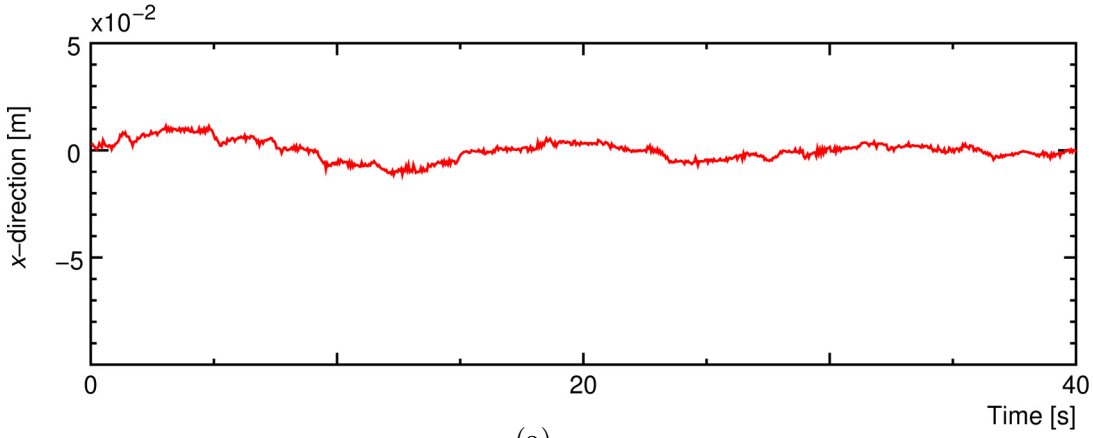

(a)

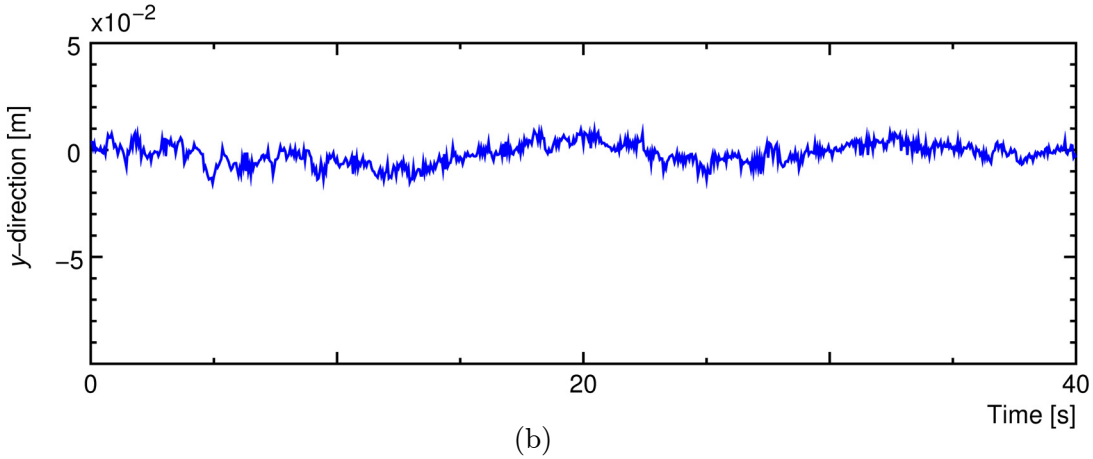

(b)

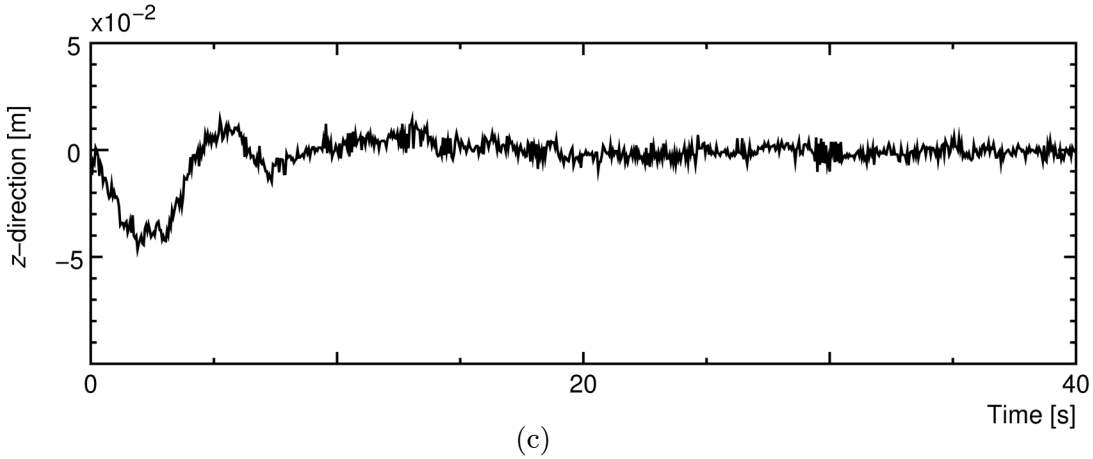

(c)

Fig. 4.25: Experimental results for case 2: Position error for left arm's end-tip

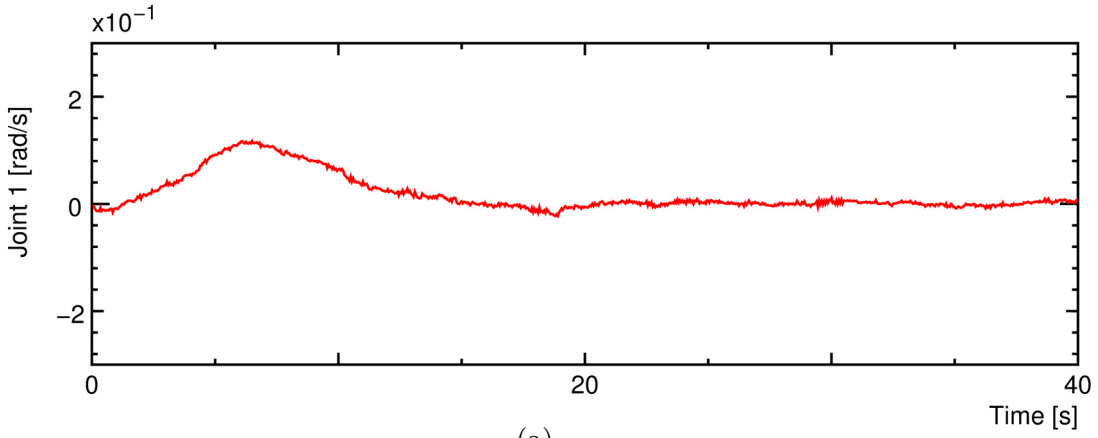

(a)

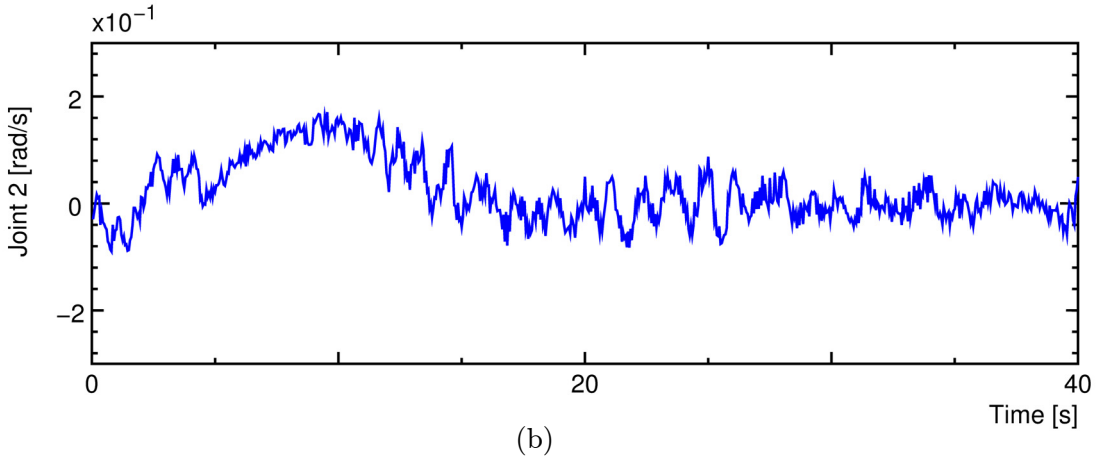

(b)

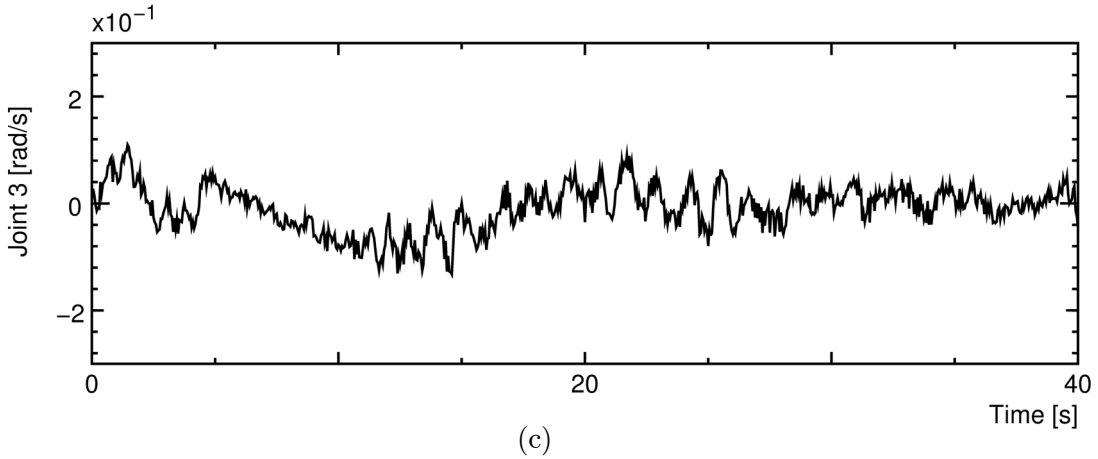

(c)

Fig. 4.26: Experimental results for case 2: Control inputs for right arm's joints

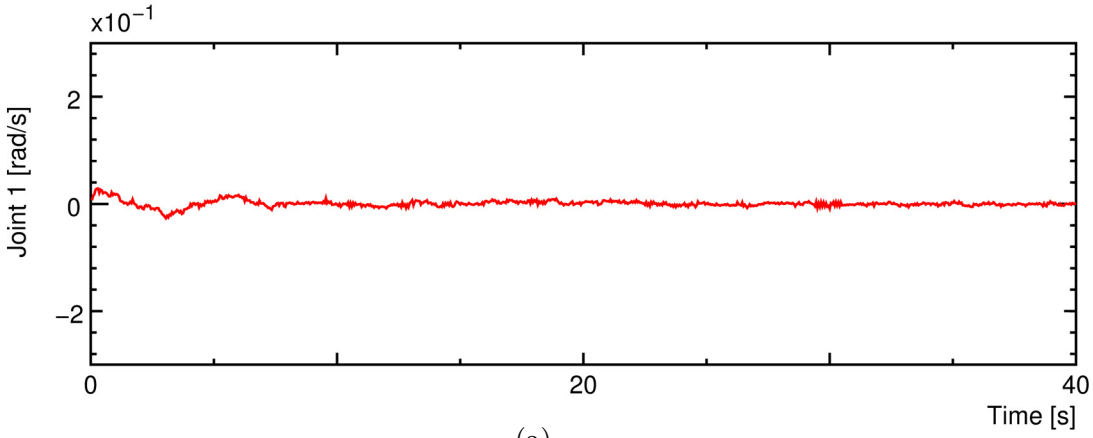

(a)

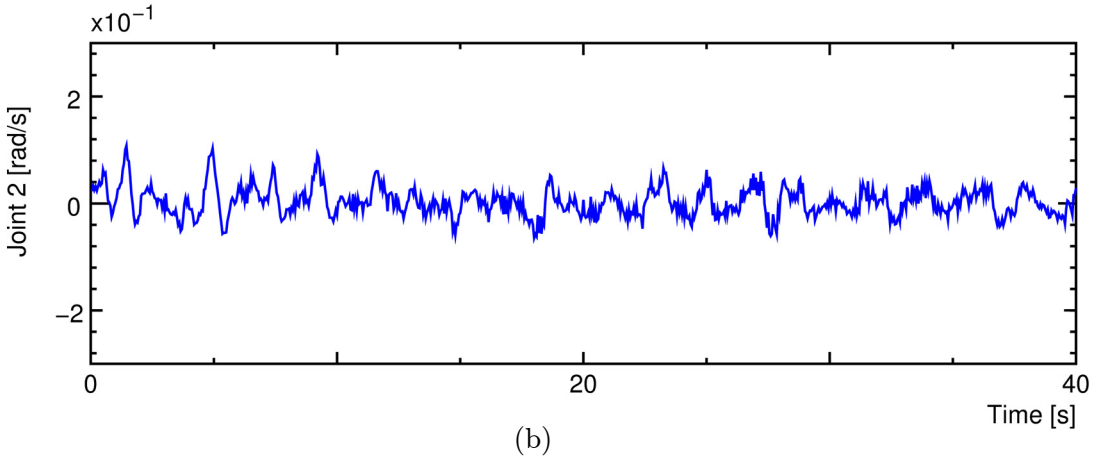

(b)

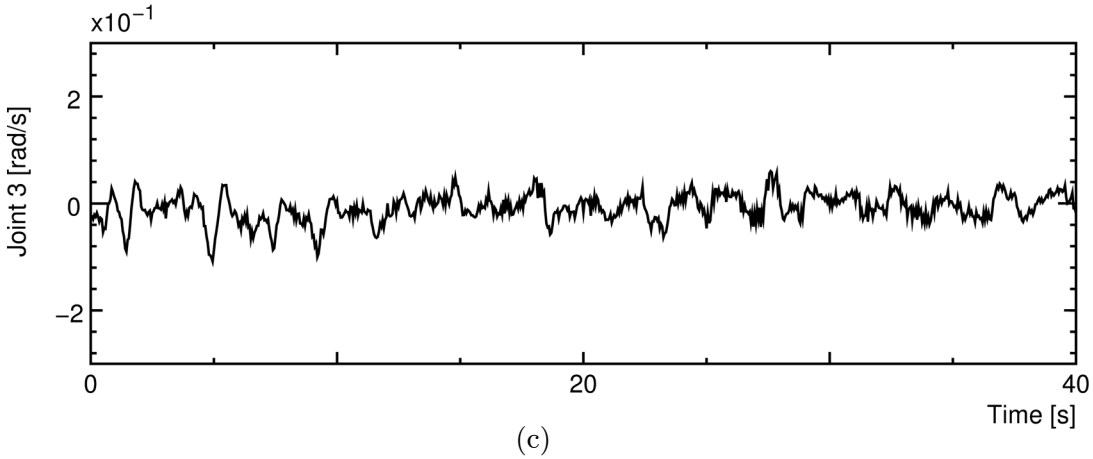

(c)

Fig. 4.27: Experimental results for case 2: Control inputs for left arm's joints

Chapter 5

Master-slave system for a 3-link dual-arm UVMS

5.1 Introduction

In Chapter 2, 3 and 4, autonomous control methods for coordinated control of AUV and multiple manipulators based on Resolved Acceleration Control (RAC) have been proposed. Moreover, the effectiveness of the proposed methods have been demonstrated through several experimental results. However, although the proposed methods demonstrated encouraging results, much more detail experiments needed to be done in order to realize fully autonomous underwater manipulation tasks. As the technologies for fully autonomous underwater manipulation using UVMS are still developing, the most relevant technique nowadays for controlling robots for underwater manipulation is by using master-slave system. In Chapter 1, various significant contributions of master-slave system in underwater intervention tasks have been explained through various events happened globally. These events showed that direct human intervention in underwater manipulation tasks using master-slave system are very essential and proved effective in solving underwater operations.

In order to be able to control an underwater robot effectively using master-slave system, an intuitive master controller that is capable for precise and easy control of robot is required. Although there are various types of off-the-shelf master controllers are being sold in the market, the products are usually very complex, expensive, and operators need to receive extensive training before being able to correctly operate the robot. These products usually require more than a single operator to control underwater robots with UVMS capabilities. Moreover, as far as the author's knowledge, there are very few studies that have focused on developing master controller that can control semi-AUVs equipped with multiple manipulators simultaneously. The authors believe that a UVMS that can be operated by a single operator is more effective and efficient due to the fact that operating UVMS by more than a single operator can create confusions that can reduce the effective-

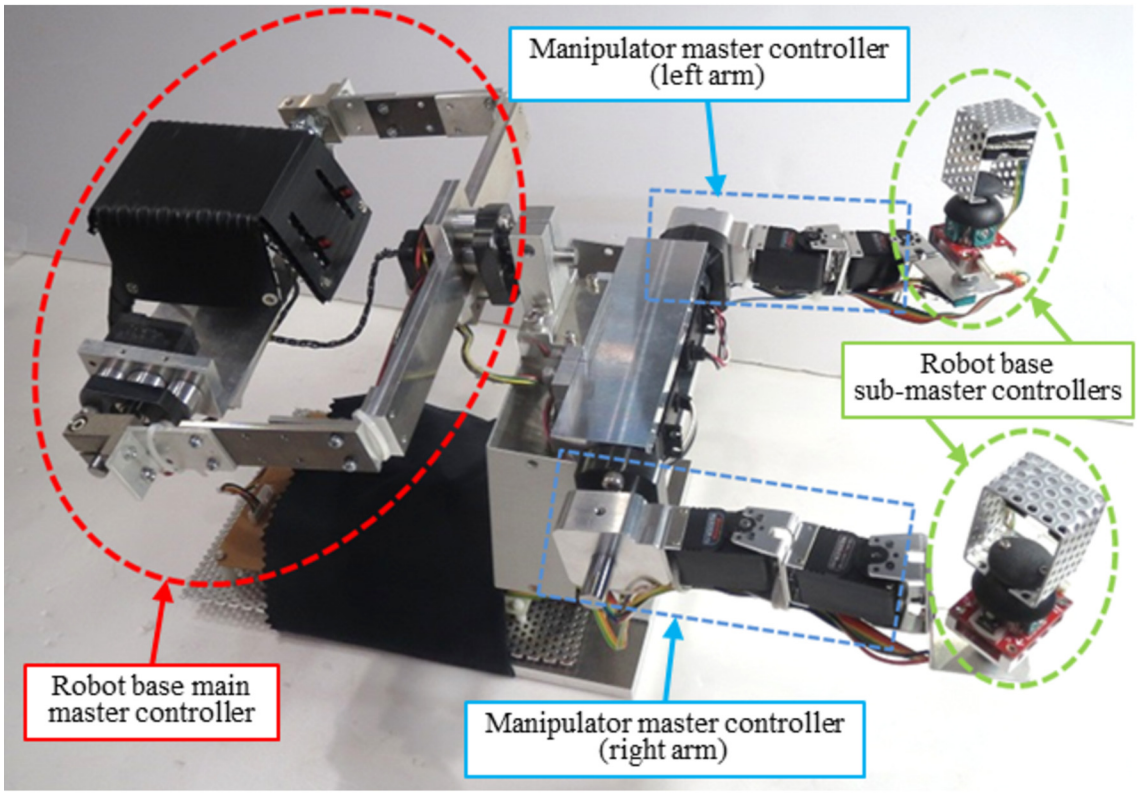

Fig. 5.1: Master controller for a 3-link dual-arm UVMS

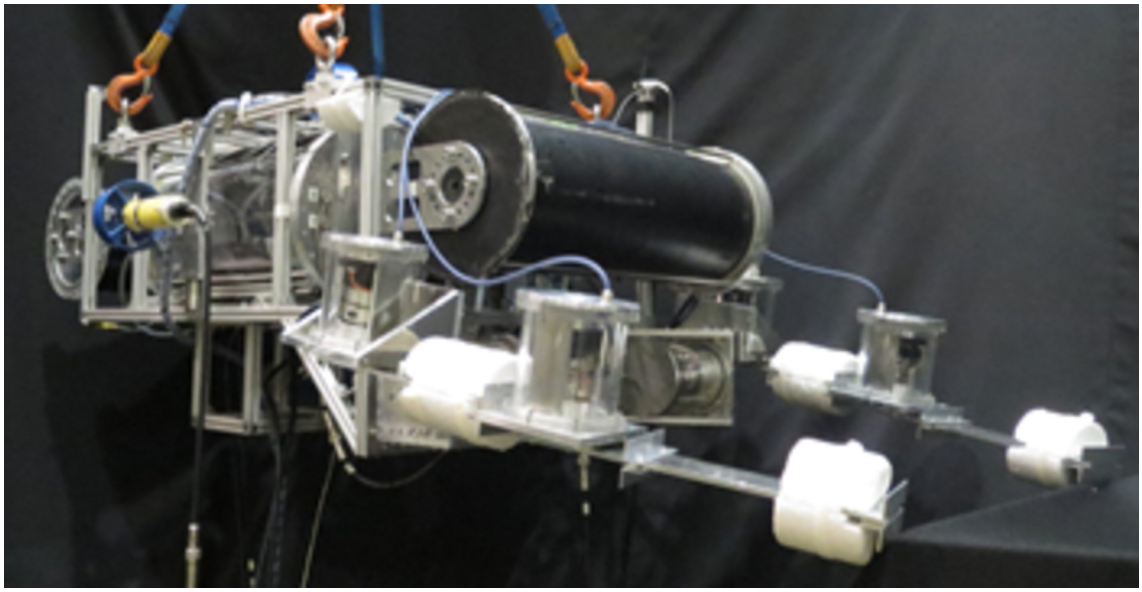

Fig. 5.2: Semi-AUV equipped with 3-link dual-arm

ness, and probably time consuming to create coherence or bonding between operators for completing any underwater intervention tasks.

This chapter addresses these problems by introducing a simple and intuitive master controller for an experimental semi-AUV equipped with 3-link dual-arm. The uniqueness of the developed master controller is the ability to simultaneously control two units of 3-link dual-arm and the position and attitude of the vehicle by only a single operator. The master controller includes a vehicle main master controller and two units of 3-link manipulator master controller. Moreover, each end-tips of the manipulator controller is attached with a vehicle sub-master controller consists of a joystick and tactile switches. These sub-master controllers are designed to have the similar functions as the vehicle main master controller which is to control the position and attitude of the vehicle.

In this chapter, the design of the developed master controller and the structure of a unilateral master-slave system are presented. The usefulness of the master controller is verified through experiment on controlling an actual dual-arm underwater robot to catch a target object in underwater environment.

5.2 Master controller

Fig. 5.1 shows the novel master controller developed in this work, consisting of a robot base main master controller, 2 units of 3-link manipulator master controller and 2 units of robot base sub-master controller that will be described in detail later in this chapter. The master controller is developed for simultaneous control of a semi-AUV and 3-link dual-arm as shown in Fig. 5.2 through master-slave system.

5.2.1 Robot base main master controller

Fig. 5.3 shows the robot base main master controller which is similar to the work done in [71]. The robot base main master controller enables the operator to control the motion of a semi-AUV in 3-dimensional space (3-DOF position and 3-DOF attitude) using only one hand.

The translational motion of the semi-AUV (x, y and z directions) can be controlled using three slide-type potentiometers installed in a box-shaped controller as shown in Fig. 5.4. The translational speed of the robot is proportional to the changes of electrical potential (voltage) from the potentiometers. Thus, the translational speed of the robot base can be controlled by adjusting the slide potentiometer levers. Fig. 5.3 also shows that the robot base controller is consists of three servo actuators. The third servo actuator is installed inside the box-shaped controller. The servo actuators were arranged so that the axes is perpendicular to the center of the box-shaped controller. These servo actuators enable the control of rotational motions of the robot base. Fig. 5.5 to Fig. 5.7 show the types of motions in order to control the semi-AUV's attitude.

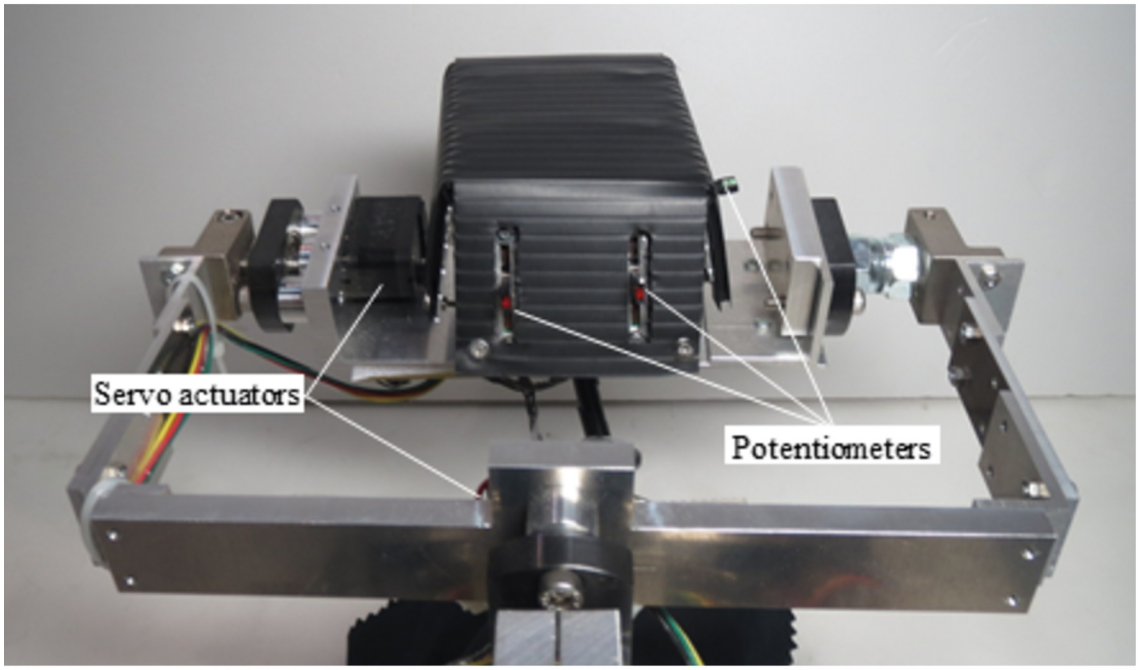

Fig. 5.3: Robot base main master controller

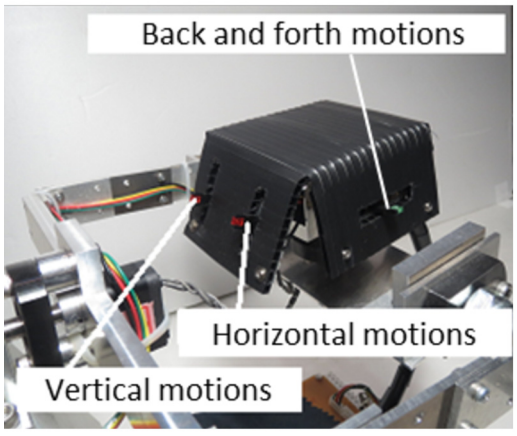

(a)

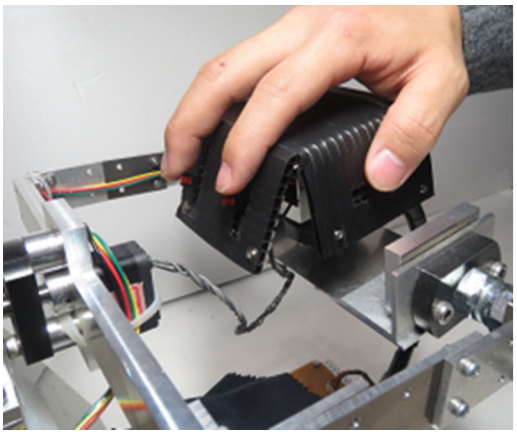

(b)

Fig. 5.4: Controlling robot base's translational motions using potentiometers. (a) Potentiometers assignments, (b) Method of handling the potentiometers

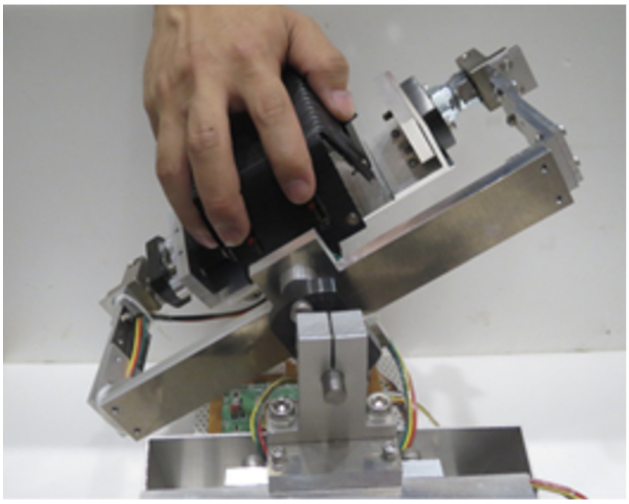

(a) Roll to the right

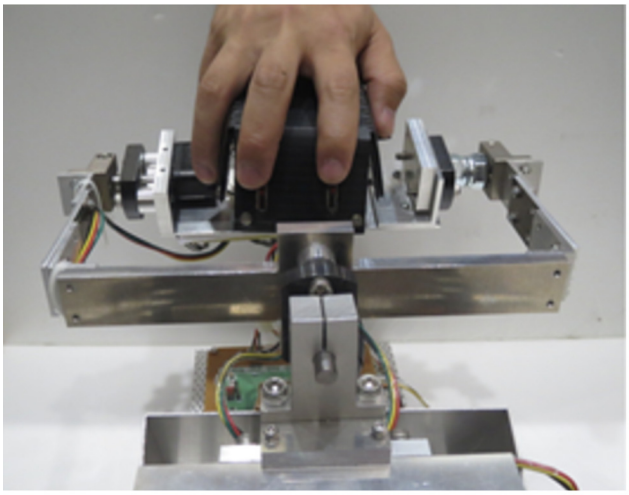

(b) Neutral position

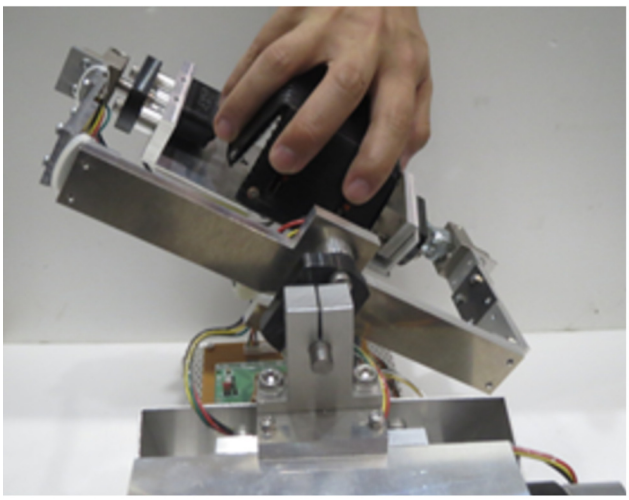

(c) Roll to the left

Fig. 5.5: Controlling robot base's roll motions using robot base main master controller

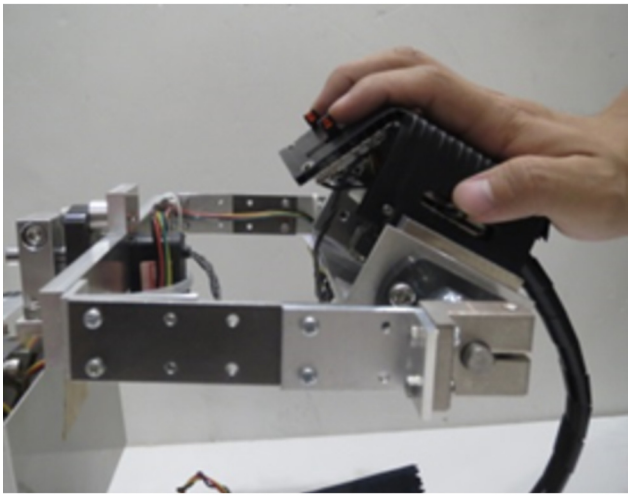

(a) Pitch up

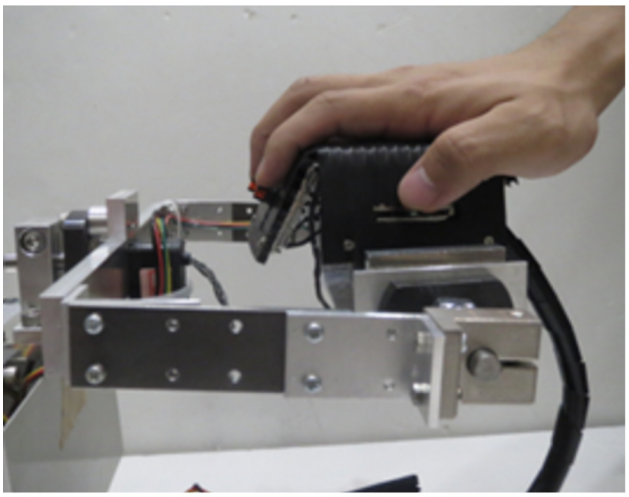

(b) Neutral position

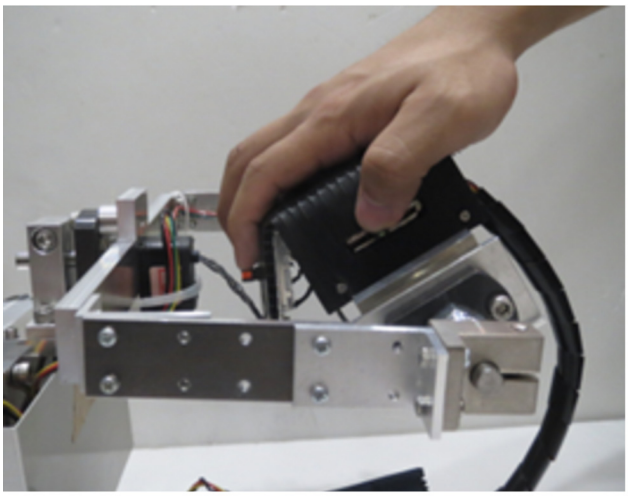

(c) Pitch down

Fig. 5.6: Controlling robot base's pitch motions using robot base main master controller

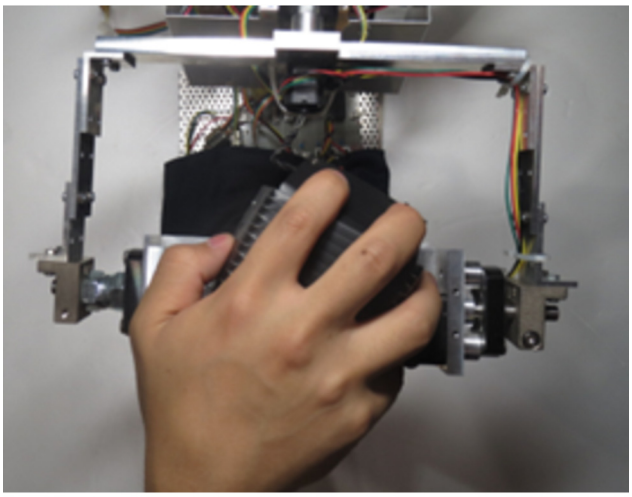

(a) Yaw to the right

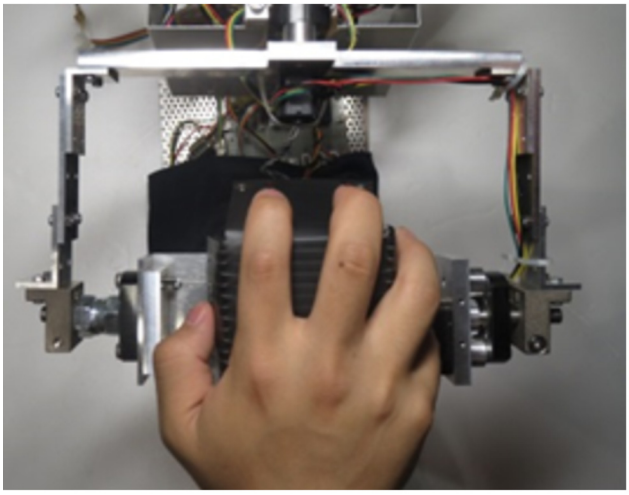

(b) Neutral position

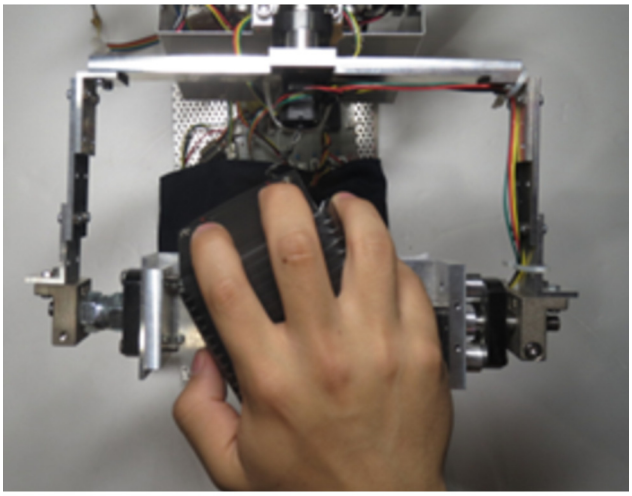

(c) Yaw to the left

Fig. 5.7: Controlling robot base's yaw motions using robot base main master controller

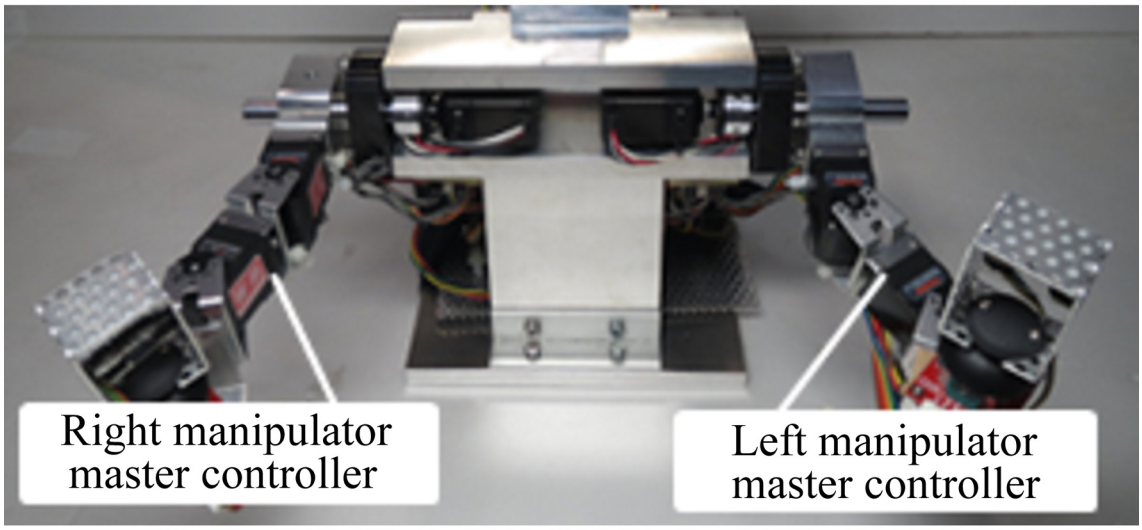

Fig. 5.8: 3-link dual-arm manipulator master controller

5.2.2 Manipulator master controller

Fig. 5.8 shows the 3-link dual-arm manipulator master controller. Each of the joints of the manipulator is consists of a RS302CD command-type servo actuator from Futaba Corporation. As the servo actuators utilize RS-485 communication protocol, high-speed communication between slave manipulators and manipulator master controllers are realized. These servo actuators are used to provide the desired joint angles for the manipulators of the slave robot including keeping any desired postures of the slave robot manipulators. Fig. 5.9 to Fig. 5.10 show the manipulator master controller motions.

5.2.3 Robot base sub-master controller

Fig. 5.11 shows the robot base sub-master controllers attached on both ends of the manipulator master controller. Fig. 5.12 shows a detail image of the sub-master controller.

It is consists of a 2-axis thumb joystick (SparkFun Electronics) equipped with a tactile switch. A U-shaped aluminum frame is attached to the joystick. A tactile switch is fixed on the aluminum frame using Velcro tape for easy positioning of the switch according to the operator's comfort. Fig. 5.12(a) and (b) show the components and the actual image of the tactile switch. It is designed in such a way so that the operator's thumb is able to push the switch at any position along the thin plastic layer as shown in Fig. 5.12(c).

The sub-master controllers have the similar function as the robot base main master controller which is to control the translational and rotational motions of robot base. Fig. 5.13 to Fig. 5.15 show the motions for controlling the position of the semi-AUV using the sub-master controller attached at the end of the right manipulator master controller. Using this sub-master controller, an operator can use his/her thumb to control the translational motions of robot base. The joystick permits the operator to control the robot base

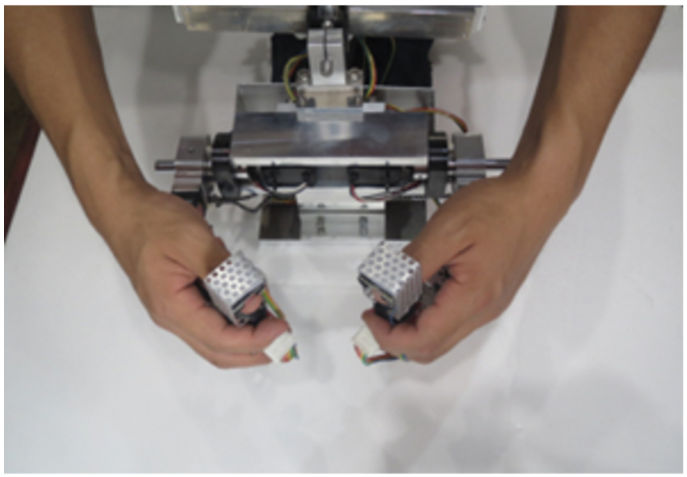

(a) Inward motion

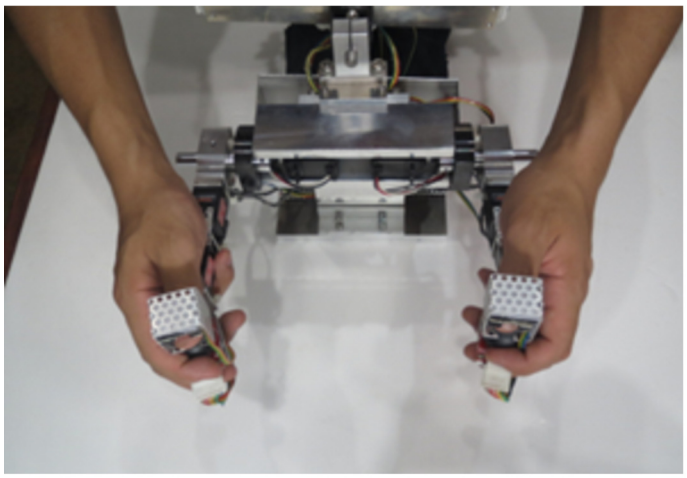

(b) Neutral position

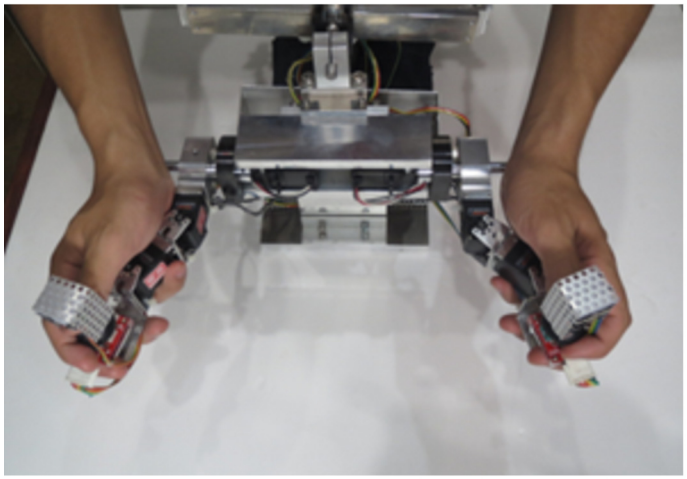

(c) Outward motion

Fig. 5.9: Controlling both arm's inward and outward motions using manipulator master controller

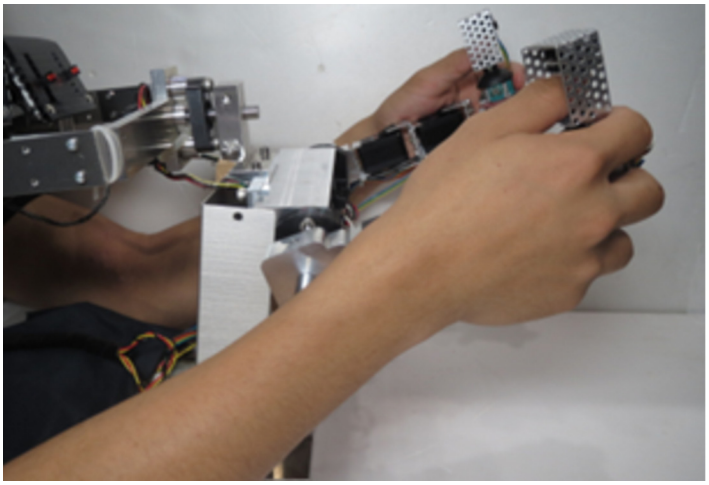

(a) Upward motion

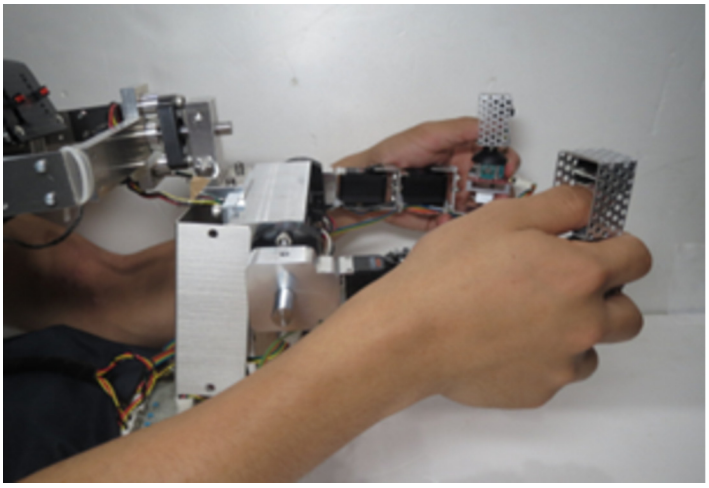

(b) Neutral position

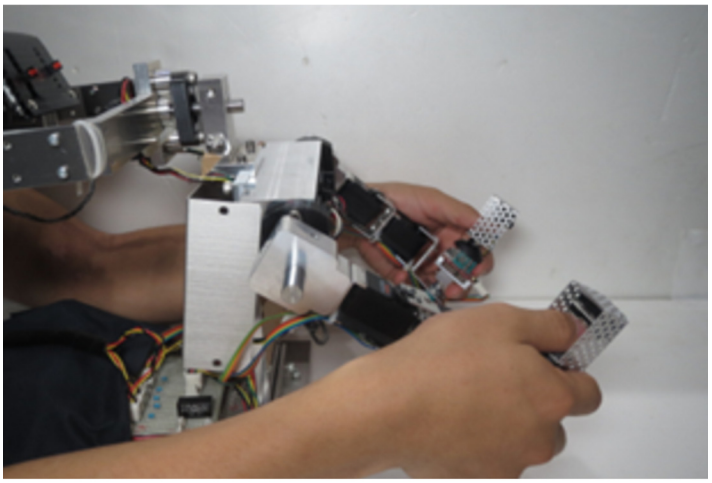

(c) Downward motion

Fig. 5.10: Controlling both arm's upward and downward motions using manipulator master controller

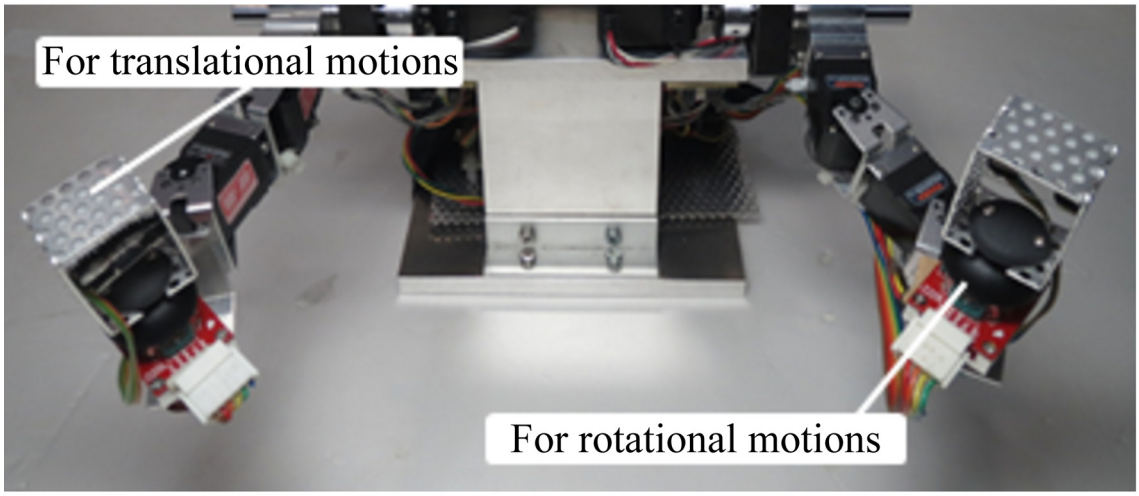

Fig. 5.11: Robot base sub-master controller

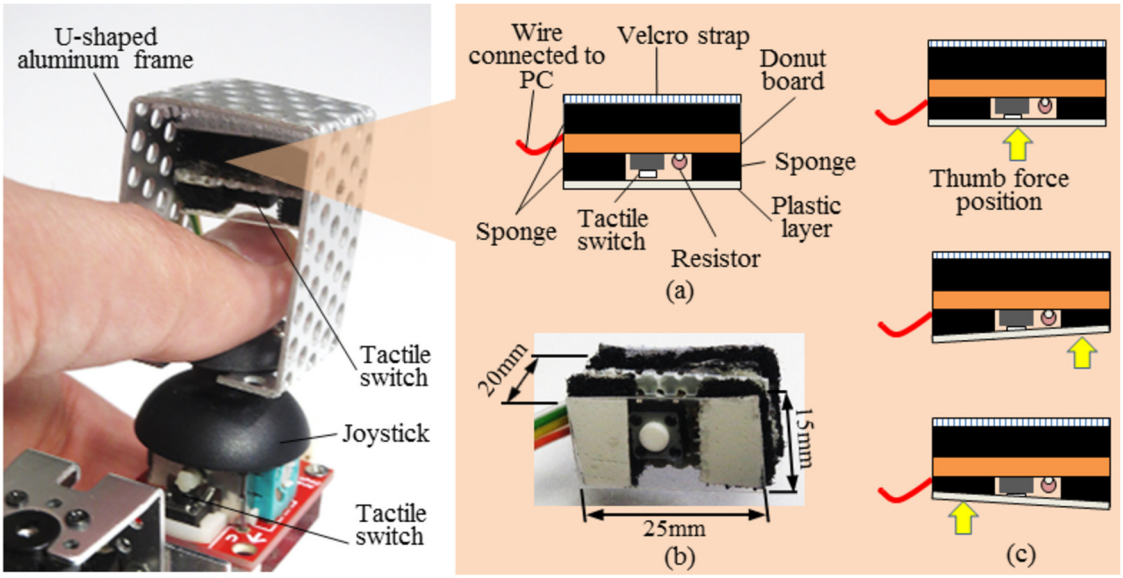

Fig. 5.12: Main components of the developed sub-master controller. (a) Detail composition of the tactile switch attached on a U-shaped aluminum frame. (b) Actual image of the tactile switch. (c) The tactile switch is guaranteed able to be pushed at any position along the thin plastic layer

to move to the front, back, left or right directions. When the joystick is pushed downward, the operator can control the robot base to move downward. The robot base can be controlled to move upward by pushing the upper tactile switch. Fig. 5.16 to Fig. 5.18 show the motions for controlling the attitude motions of the semi-AUV using the sub-master controller located at the end of the left manipulator master controller. This sub-master controller is for controlling the rotational motions of the robot base. The joystick allows the operator to control the robot base to roll to the left or right, and pitch to the front or

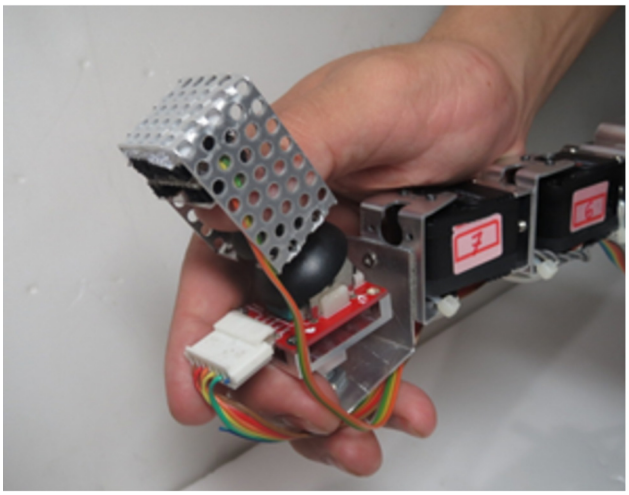

(a) Forward motion

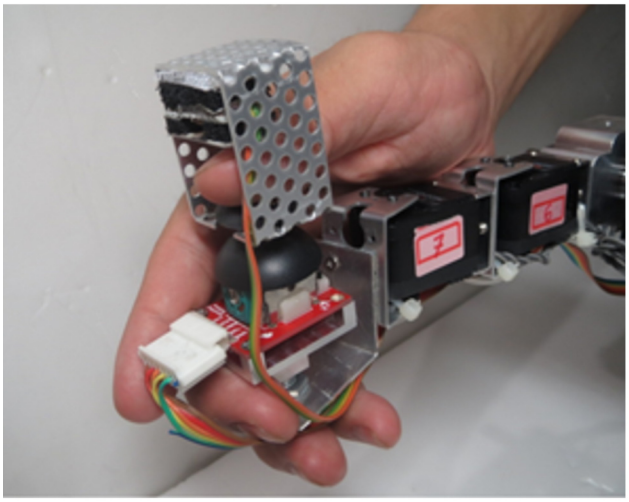

(b) Neutral position

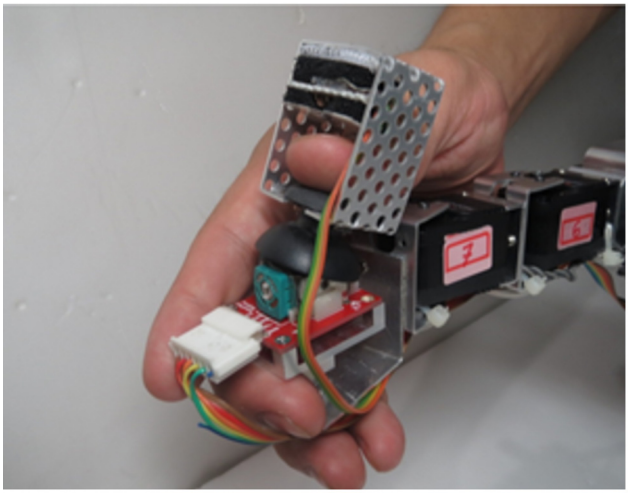

(c) Backward motion

Fig. 5.13: Controlling robot base forward and backward motions using robot base sub-master controller

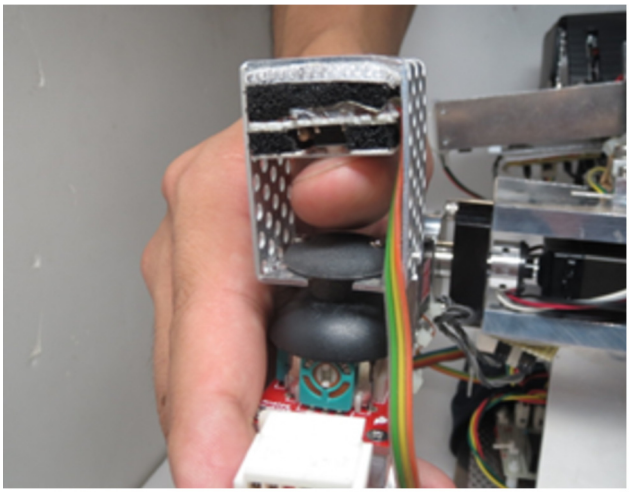

(a) Upward motion

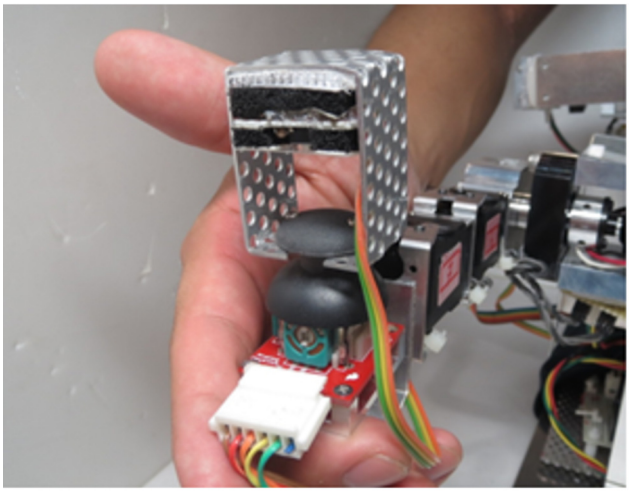

(b) Neutral position

(c) Downward motion

Fig. 5.14: Controlling robot base upward and downward motions using robot base sub-master controller

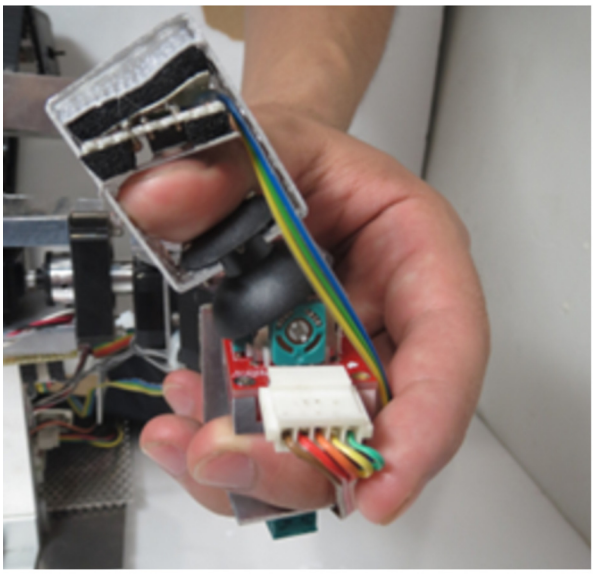

(a) Sway to the right

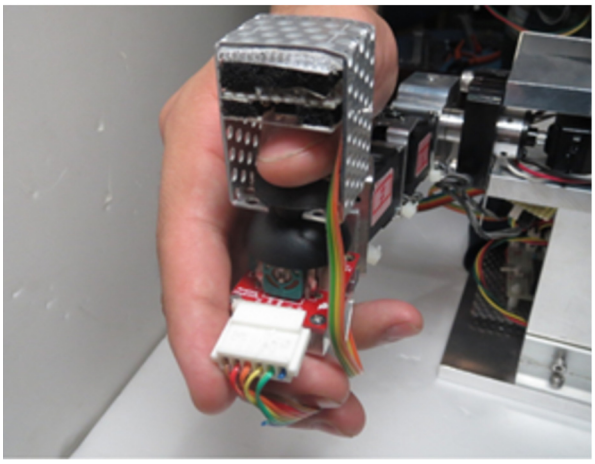

(b) Neutral position

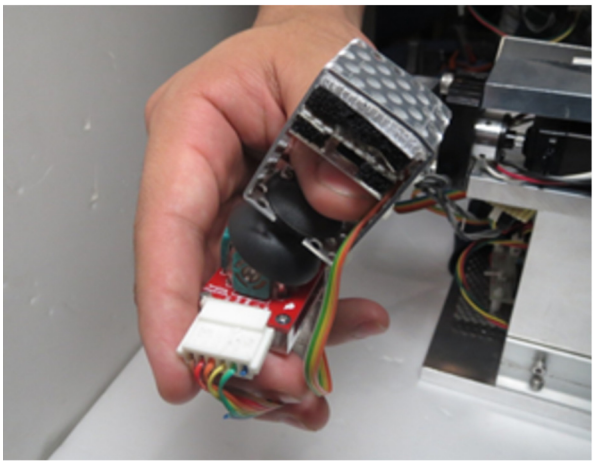

(c) Sway to the left

Fig. 5.15: Controlling robot base to sway to the right and left using robot base sub-master controller

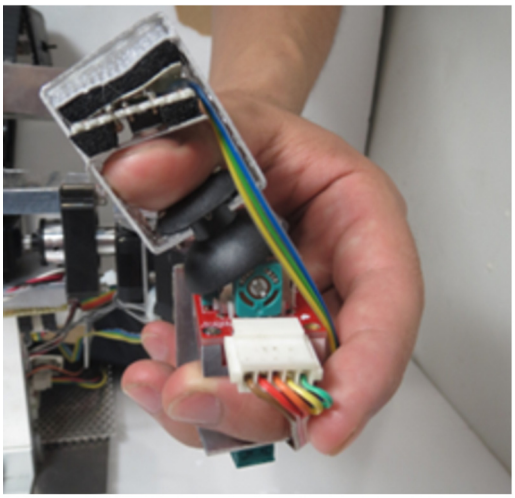

(a) Roll to the right

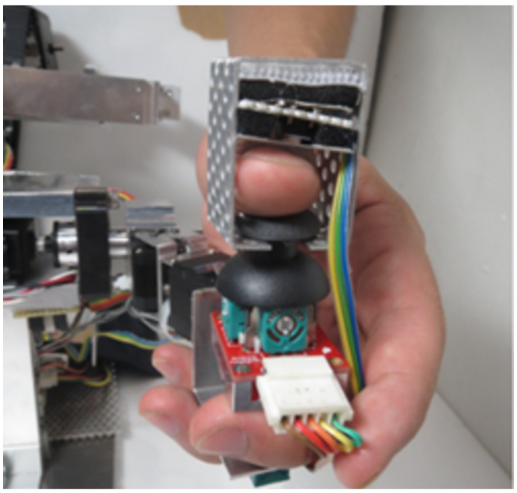

(b) Neutral position

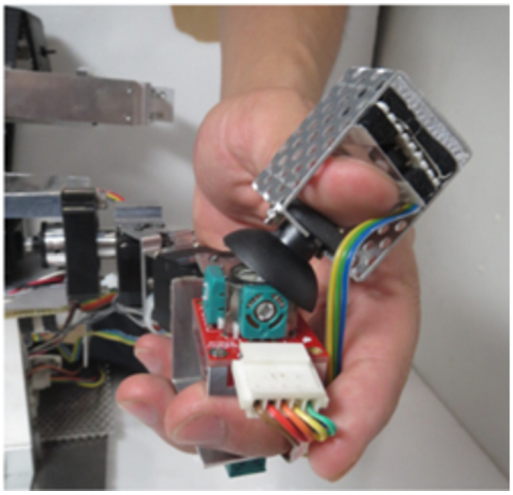

(c) Roll to the left

Fig. 5.16: Controlling semi-AUV's roll motions using robot base sub-master controller

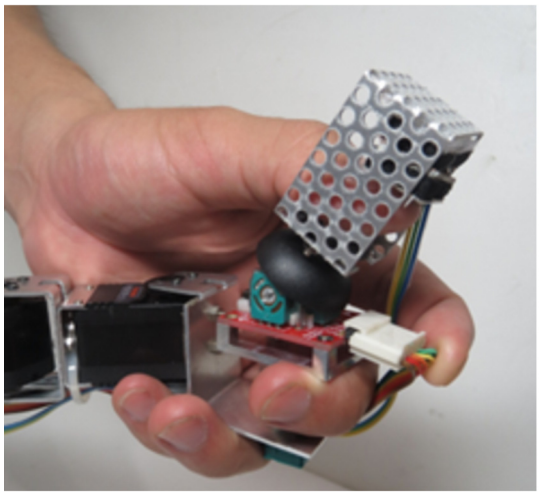

(a) Pitch down

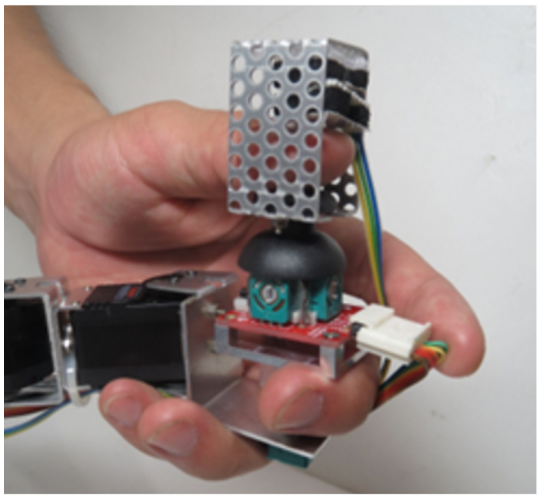

(b) Neutral position

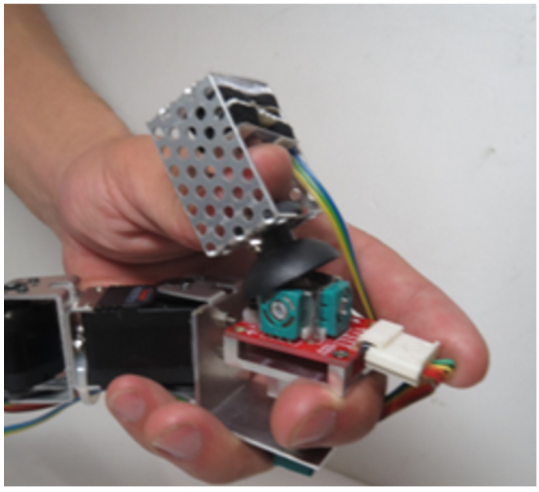

(c) Pitch up

Fig. 5.17: Controlling semi-AUV's pitch motions using robot base sub-master controller

(a) Yaw to the right

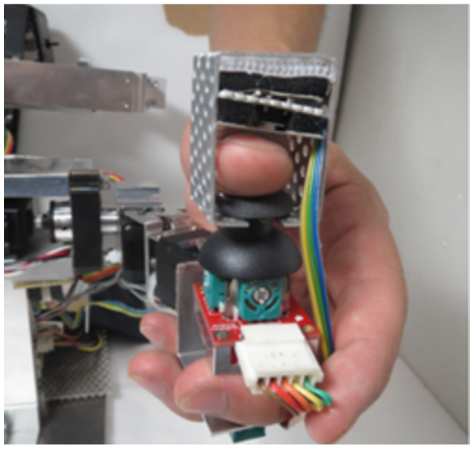

(b) Neutral position

(c) Yaw to the left

Fig. 5.18: Controlling semi-AUV's yaw motions using robot base sub-master controller

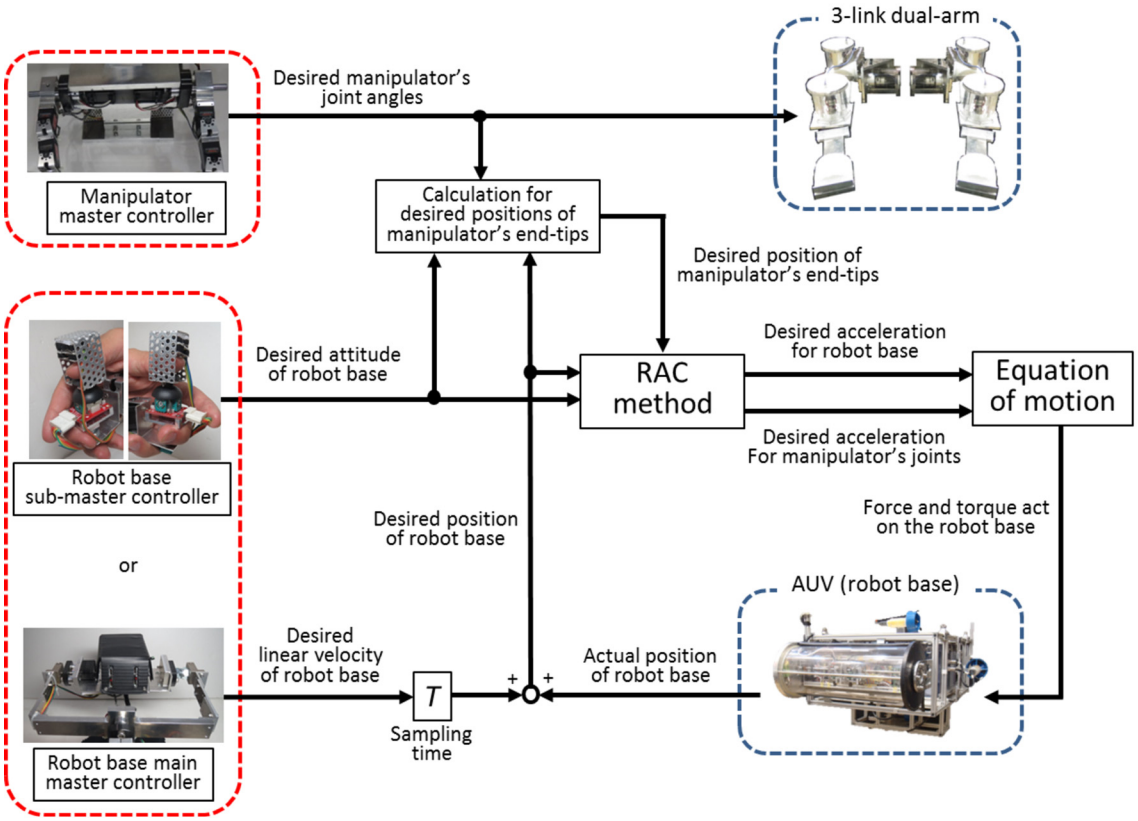

Fig. 5.19: Control system for master-slave system

back. The operator can control yaw to the left or right by pushing the joystick downward or upward, respectively.

Additionally, the control functions can be swapped between the two sub-master controllers according to the operator's comfort. The sub-master controllers allow an operator to control the motions of the underwater vehicle by only using both thumbs. At the same time, the operator can control the motions of both arms. This is a unique feature in the design of this master controller.

5.2.4 Control system

Fig. 5.19 shows a simplified diagram of the control system involved in the proposed master-slave system. The control system for the AUV equipped with 3-link dual-arm utilized in this work is based on the Resolved Acceleration Control (RAC) method introduced in Chapter 2. As verified in previous chapters, by using the proposed RAC method, coordinated motions control of the underwater vehicle and multiple arms have been achieved, resulting to a good performance for the control of the robotic arm's end-tips to follow the desired trajectories. However, in this work the RAC method controlled only the AUV by using the desired linear velocities and attitude of the robot base and manipulator's joint

angles from the master controller. The RAC method capable of keeping the stability of the AUV during the motions of both arms.

Based on the block diagram, each joints on the slave manipulator received the desired manipulator's joint angles signals directly from the manipulator master controller. On the other hand, RAC method introduced in Chapter 4 is used to calculate the actual force and torque applied to the robot base. In order to utilize the RAC method, the desired position and attitude of the robot base and manipulator's end-tips are required. Firstly, the desired position of the robot base is obtained by multiplying the desired linear velocity of the robot base with sampling time, which then added with the current position of the robot base. Furthermore, the desired attitude of the robot base is obtained directly from the desired attitude signals received from the master controller. Therefore, in term of signals received from the robot base, the RAC method utilizes the desired position and attitude of the robot base.

On the other hand, another important signals for RAC method is the desired position of the manipulator's end-tips. The desired position of the end-tips are obtained using the the desired position and attitude of the robot base described above, and also the geometrical relationship based on the desired manipulator's joint angles from the manipulator master controller.

Thus, the obtained desired position and attitude of the robot base and desired position of the end-tips are used in the RAC method to derive the desired linear and angular acceleration of the robot base and desired angular acceleration of the manipulator's joints. Then, the derived desired accelerations are utilized in the equation of motion for the UVMS described in section 4.3 to compute the required thrust force and torque that act on the robot base, and also the required torque for the slave manipulator's joints. However, as described previously, each joints on the slave manipulator received the desired signals directly from the manipulator master controller. As a result, only the required thrust force and torque that act on the robot base are sent to the the AUV as shown in the diagram. The parameters of the velocity error feedback gains, and position and attitude error feedback gains for the robot base and both arm's end-tips are similar to the parameters explained in subsection 4.5.1.

5.3 Experimental setup and conditions

Fig. 5.20 shows the structure of the master-slave system. A total of 9 units of servo actuators, 7 units of potentiometers and two tactile switches are used in the developed master controller. All data from the potentiometers and switches are sent to A/D converters of a surface master computer. On the other hand, all servo actuators are connected to the master computer via an FPGA board. The FPGA board is connected to a MAX485 chip to convert RS-485 data signals into RS-232C signals and vice versa.

The experiment for verifying the effectiveness of the developed master controller on

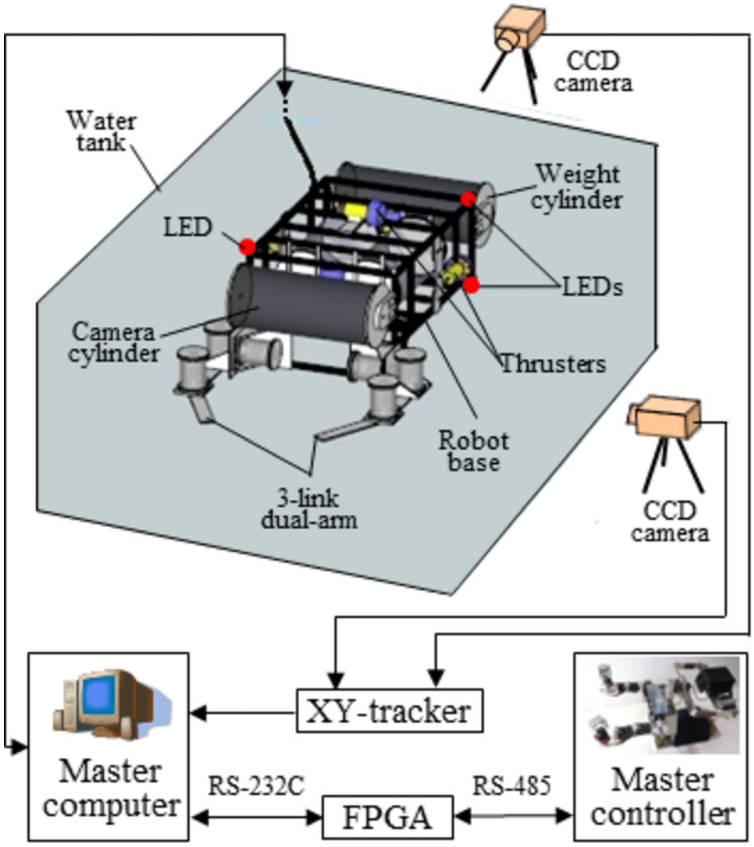

Fig. 5.20: Structure of the master-slave system

controlling an actual 3-link dual-arm underwater robot was conducted based on the experimental setup shown in Fig. 5.20. The experiment was carried out in a water tank. The tank specifications are 3[m] width, 2[m] length and 2[m] depth. The position and attitude of the robot can be calculated by monitoring the movement of three LEDs light sources via CCD cameras. The data from CCD cameras were converted to position data using an X-Y video tracker. The data sampling period was $T = 1/20$[s].

Regarding the experimental conditions, as described in the previous section, the robot base main master controller is similar to the work done in [71]. Thus, the detail experimental results to demonstrate the effectiveness of the robot base main master controller will not be described here, it is presented in [71]. In this experiment, an operator was asked to catch an object using (a) the robot base sub-master controllers to move the robot base and, (b) manipulator master controllers to move the slave manipulators.

5.4 Experimental results and discussions

Fig. 5.21 shows image sequences during the experiment. The small figures on the upper left are the images of the master controller being used during the experiment. Fig. 5.21(a) and

(b) show the robot moving towards the target object. After 50[s], the operator successfully caught the target object using both arm as shown in Fig. 5.21(c). Fig. 5.21(d) shows the user moving both arms upward while holding the target object.

The desired and actual arm's joint angles for right and left arms during the experiment are shown in Fig. 5.22 and Fig. 5.23, respectively. Both figures show that both slave arms mounted on the semi-AUV followed the desired joint angles command from the manipulator master controller. Furthermore, Fig. 5.24 and Fig. 5.25 show the time histories of the robot position and attitude during the experiment, respectively. It can be seen that the results demonstrate the actual robot position and attitude correspond to the desired position and attitude from the robot base sub-master controller. During the experiment, the operator only controlled the translational motion of the robot as there were no need for rotational motions. The experiment demonstrate that the operator was able to control the robot base and both arms simultaneously using the robot base sub-master controllers and manipulator master controllers.

5.5 Conclusions

We have developed a master controller for a 3-link dual-arm semi-autonomous underwater vehicle. By using the proposed master controller, an operator is able to remotely control the motion of an underwater vehicle equipped with 3-link dual-arm in 3-dimensional space.

The uniqueness of the proposed master controller is that a human operator is able to control two units of 3-link manipulator and also controls the motion of underwater vehicle simultaneously. As far as the author's knowledge, there are no research-based or even commercially available master controller that enables a single operator to operate a vehicle and multiple manipulators simultaneously. The usefulness of the proposed master controller was verified through experiments on controlling an actual 3-link dual-arm semi-autonomous underwater vehicle.

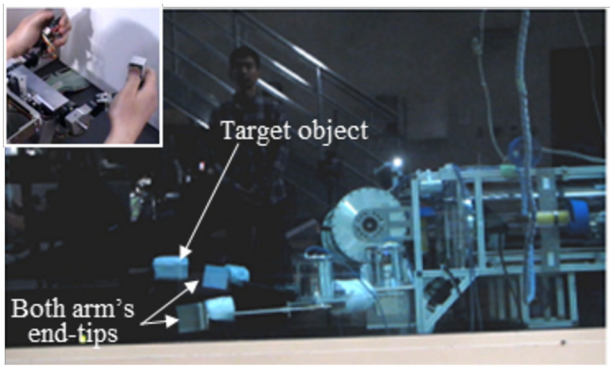

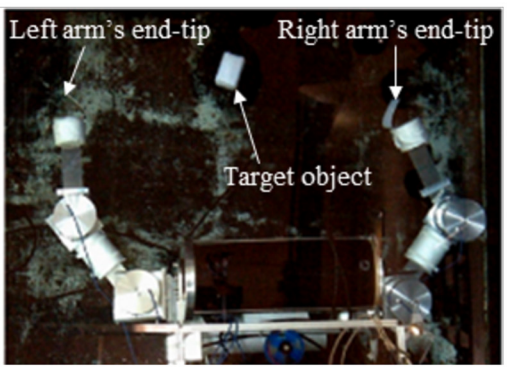

(a) Time = 5[s]

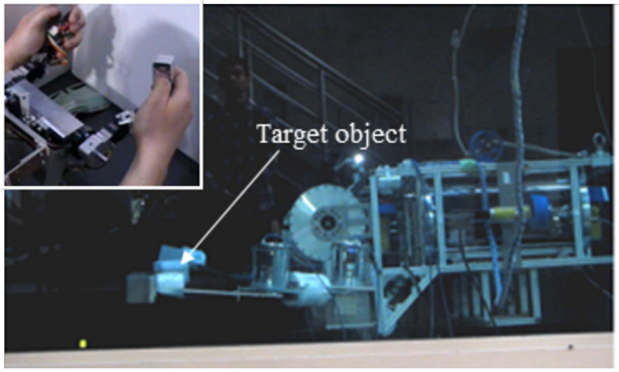

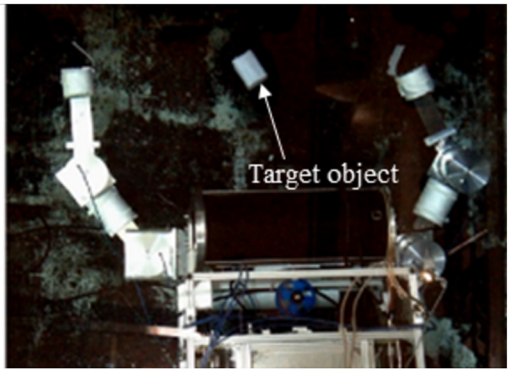

(b) Time = 15[s]

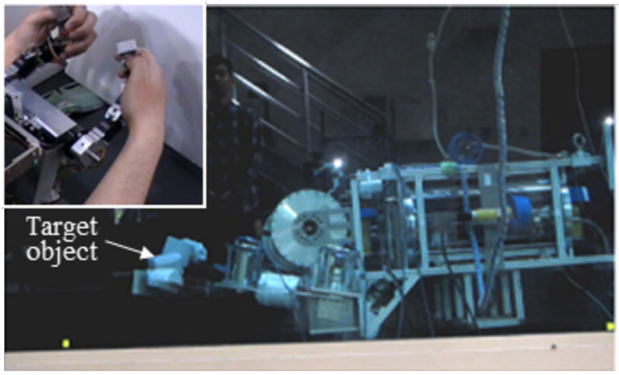

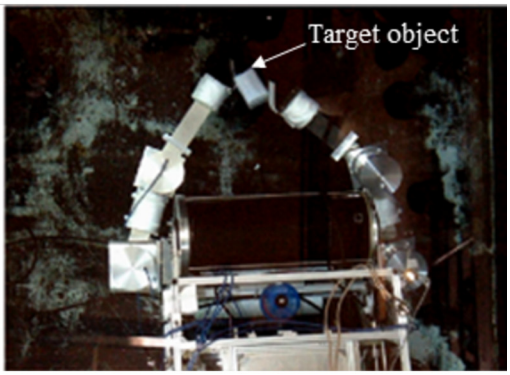

(c) Time = 50[s]

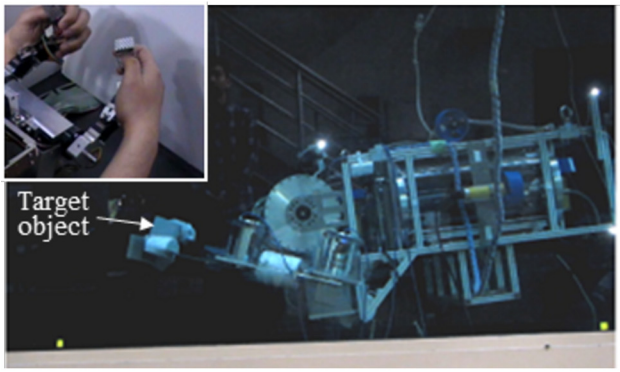

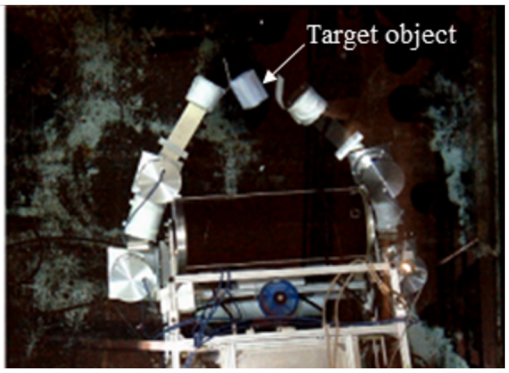

(d) Time = 75[s]

Fig. 5.21: UVMS motions during experiment

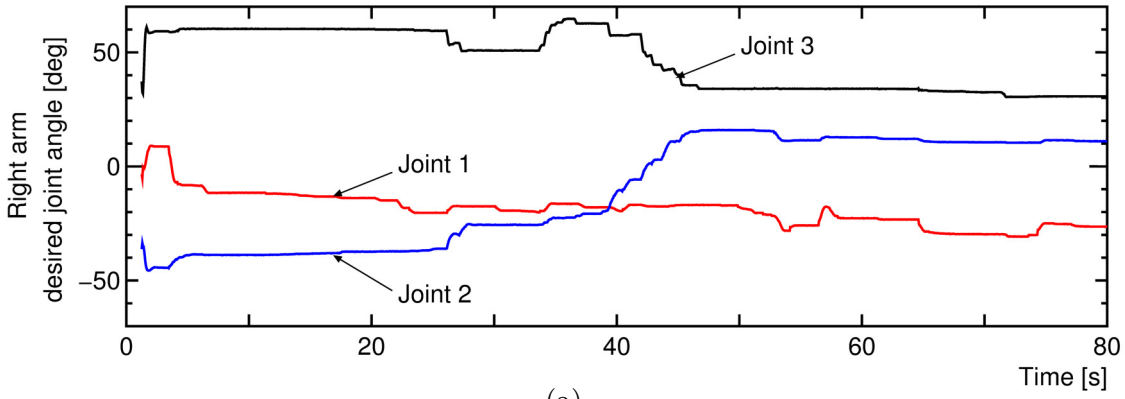

(a)

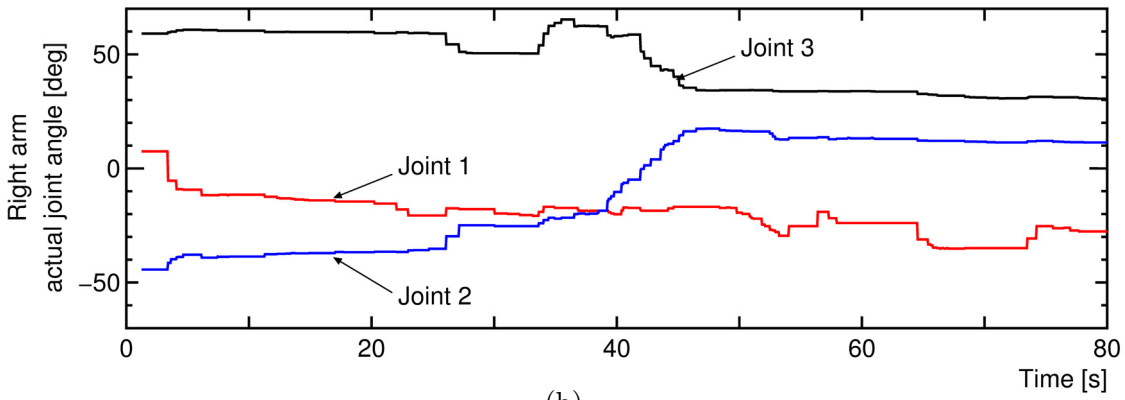

(b)

Fig. 5.22: Time history of right arm's joint angles

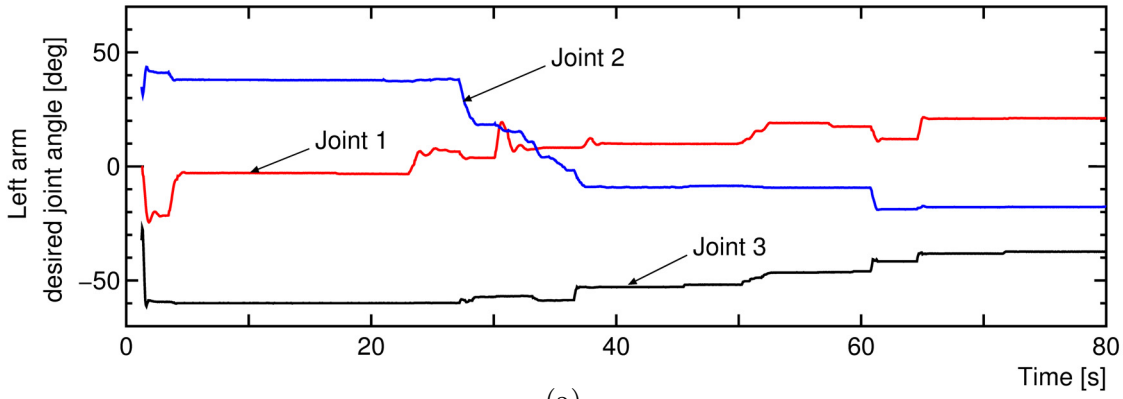

(a)

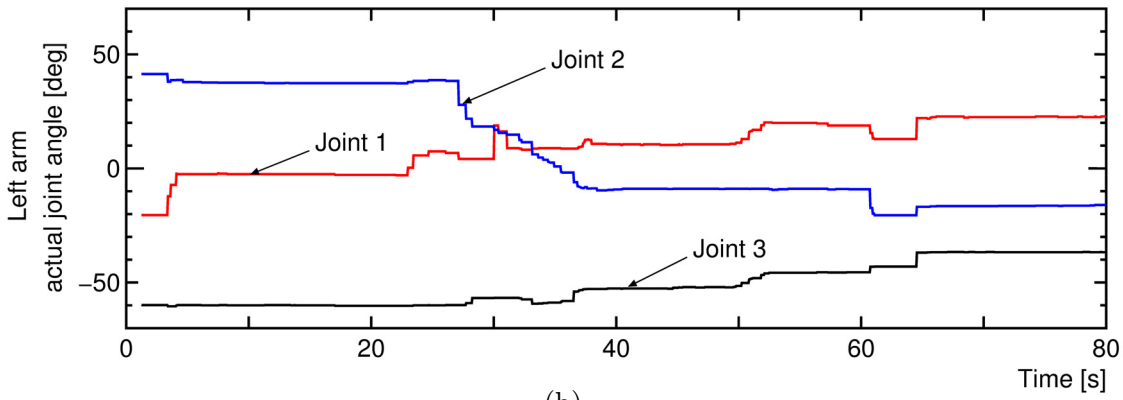

(b)

Fig. 5.23: Time history of left arm's joint angles

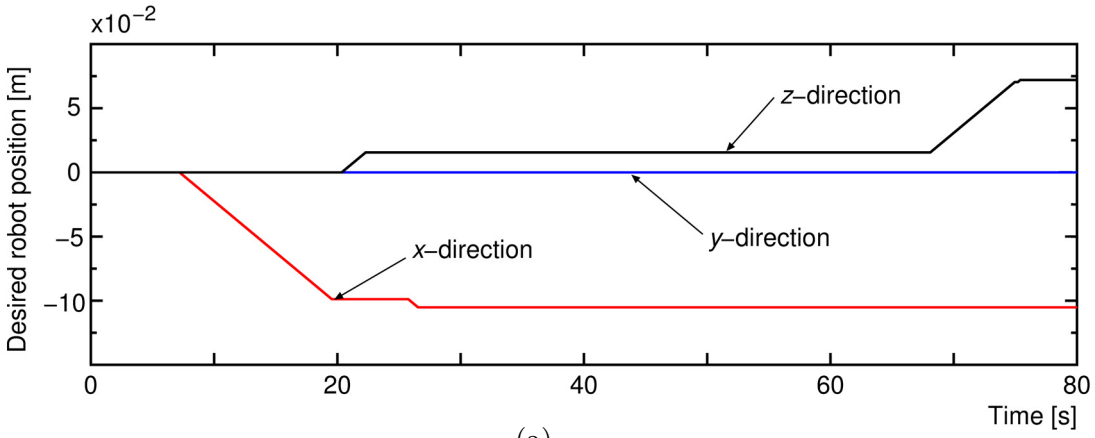

(a)

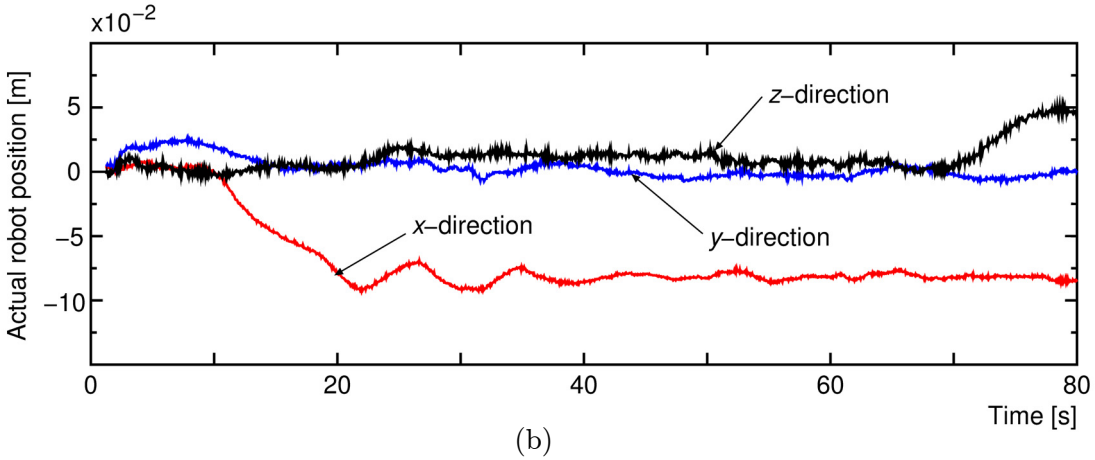

(b)

Fig. 5.24: Time history of the desired and actual position of robot base

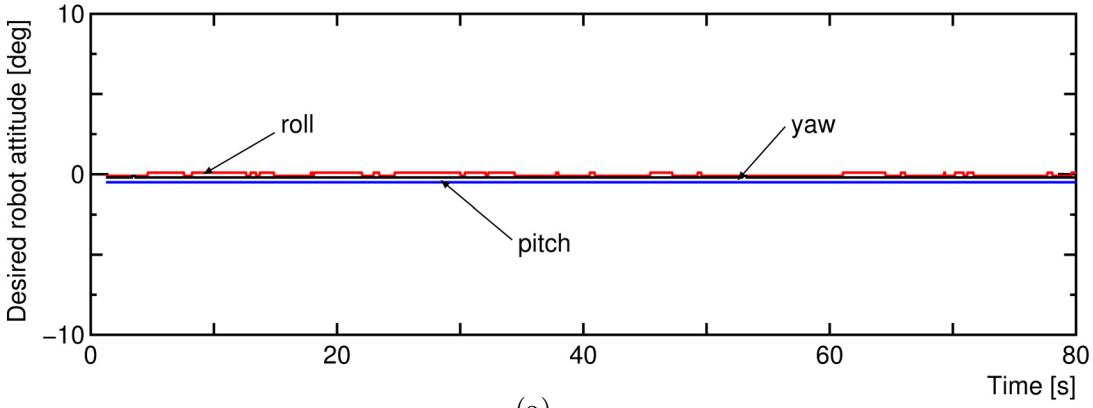

(a)

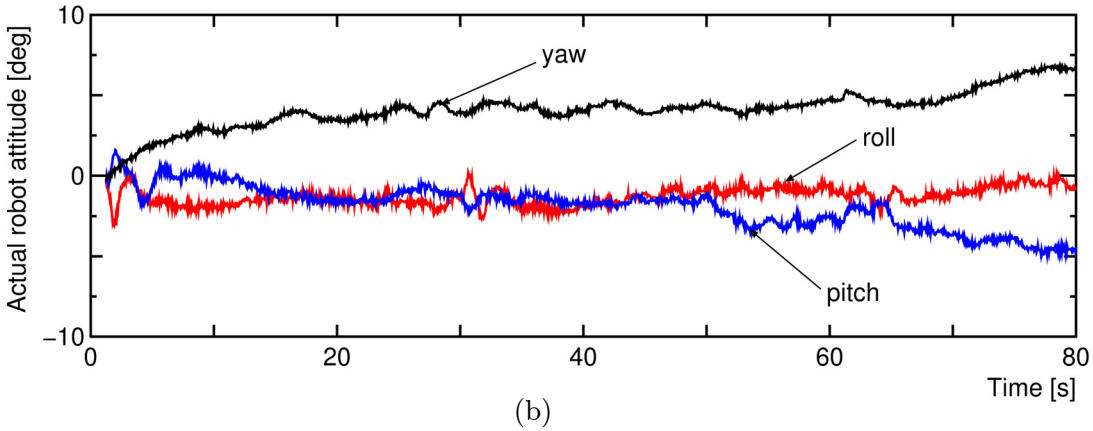

(b)

Fig. 5.25: Time history of the desired and actual attitude of robot base

Chapter 6

Conclusions and future recommendations

The aim of this doctoral thesis is to present Resolved Acceleration Control (RAC) method for coordinated motion control of fully autonomous underwater vehicle (fully-AUV) and multiple arms. The effectiveness of the proposed RAC method was demonstrated through two experiments using actual full-AUVs equipped with dual-arm that were divided into two separate chapters. As the technologies for underwater manipulation tasks using fully-AUVs equipped with multiple arms are still premature stage, the utilization of master-slave in manipulation tasks are very relevant currently. Thus, the thesis also presented a chapter describing a novel master controller for a master-slave system that can simultaneously controls a semi-autonomous underwater vehicle (semi-AUV) and 3-link dual-arm by only a single human operator. In this chapter, the results of each chapter is summarized.

Chapter 2 described the detail steps on developing a RAC method for multi-link and multi-arm underwater vehicle-manipulator system (UVMS). Based on literature, there are very few studies that consider the coordinated motions of a fully-AUV and multiple arms. Moreover, as far as the author's knowledge, there are no detail experiment-oriented studies related to this topic. In the beginning of Chapter 2, the model of a multi-link multi-arm UVMS is presented, and from this model, the kinematic and momentum equations for the UVMS is described. The developed momentum equation was consisted of linear and rotational momentum of the UVMS considering hydrodynamic added mass and added inertia moment acting on the UVMS. The hydrodynamic drag forces, drag moment and buoyant forces acting on the UVMS were also formulated. Then, the dynamic equation to obtain the desired motion of the UVMS was described. At the end of Chapter 2, the detail explanation about the proposed RAC method that was developed with the purpose to precisely control the position of manipulator's end-tip to follow the desired pre-planned trajectory was introduced.

Chapter 3 presented the experimental results that demonstrated the effectiveness of the RAC method proposed in Chapter 2. Up to the present time, this is the first study

that verified the effectiveness of a control method for multiple arm UVMS through actual experiment. The experiment was carried out using a 2-link planar dual-arm UVMS. The joints of the developed 2-link planar arm were actuated by command-type servo motors. Torques were transmitted to move each arm's link via magnetic coupling mechanism. The experiment results demonstrated good performance of coordinated control of the fully-AUV and 2-link planar dual-arm. The results showed that both arm's end-tips were able to be controlled along the desired trajectories with small position errors in spite of a significantly large motions of the fully-AUV.

Chapter 4 described the experimental results to further demonstrate the effectiveness of the RAC method to control the positions of the end-tips in 3-dimensional space. In the previous chapter, a RAC method for controlling 2-link planar dual-arm UVMS was developed. However, the developed method could only control the end-tips in a 2-dimensional space only. Therefore, in Chapter 4, a RAC method for a 3-link dual-arm UVMS was introduced and the effectiveness of the method was verified through experiments that were divided into two separate cases. The experimental results of both cases showed very encouraging results. In both experiments, despite the fully-AUV was excited by the reaction forces due to the motions of the arms, the end-tips of both arms were able to be controlled to follow the desired trajectories with very small position. Chapter 4 also described the structure of a newly developed joint for the 3-link dual-arm. The command-type servo motors that were used in the first joint on both arms have larger torque from the rest of the joints. The reason was in the experiment carried out for Chapter 3, the first joints received larger loads during arm motions. Larger load means larger torque was needed to move the arm. Since magnetic couplings were utilized for the joints in Chapter 3, slip will occur when the servo motors rotated fast. Thus, in the design of the joints for the 3-link arm, command-type servo motors with larger torque were used, and instead of magnet coupling mechanism, conventional waterproofing of the joints using O-rings were utilized.

In Chapter 5, a very first master controller that enables a single operator to operate a semi-AUV and multiple manipulators simultaneously was introduced. The detail designs of the easy-to-use and intuitive master controller which include a vehicle main master controller and two units of 3-link manipulator master controller were described. The developed master controller also consists of two units of vehicle sub-master controller that allow the operator to simultaneously control two units of 3-link dual-arm and the position and attitude of the vehicle. At the end of this chapter, experimental results on controlling an actual dual-arm underwater robot to catch a target object in underwater environment using the proposed master controller were presented and discussed.

The thesis has provided significant contributions by presenting experimental results that show the effectiveness of the proposed RAC method on producing coordinated motions control of a fully-AUV and multiple arms. Furthermore, a novel, one of a kind master controller for controlling a 3-link dual-arm UVMS has been introduced, and the usefulness of the developed master controller was verified through catching a target object

experiment.

There are several exciting future studies that can be carried out following the positive results achieved in this work. Currently, the position and attitude of the robot are depended on X-Y video tracker. Thus, upgrading it to commercial off-the-shelf inertial measurement unit (IMU) can provide a more precise control of the robot and simplify the experimental setup. The developed underwater vehicle is a type of semi-AUV that is suitable for underwater intervention tasks. Therefore, a master-slave system can be developed for the semi-AUV, utilizing human-robot interface to an autonomous underwater vehicle system. Furthermore, the effectiveness of the master-slave system can be further enhanced by incorporating a novel stereo-vision system that are currently under development [89]. Once completed, the vision system is capable to visually assist the operator during manipulation tasks. As a result, the performance of the underwater vehicle can be improved by maintaining the ability of direct human intervention in an autonomous robotic system. Furthermore, the development of hand grippers for the dual-arm are necessary for future underwater intervention tasks. Lastly, the developed master controller should be improved further by considering force feedback control to realize an intuitive user interface that has the capability of bilateral control.

Acknowledgement

In the name of Allah, Most Gracious, Most Merciful

First and foremost, the author would like to thank to his supervisor, Associate Professor Dr. Shinichi Sagara, Department of Mechanical and Control Engineering, Kyushu Institute of Technology, for his great wisdom, his valuable guidance and support towards the completion of this research work. The author always be in astonishment of his vast experience and inventiveness on solving problems making the journey of completing this research under his supervision as invaluable experience.

Special thanks are extended to the members of the dissertation committee for their invaluable inputs: Professor Dr. Masahiro Oya, Professor Dr. Kim Hyoungseop and Associate Professor Dr. Hiroyuki Miyamoto.

The author would also like to thank Mr. Tomohisa Inada for being the frequent technical advisor in the laboratory, and Mr. Shunji Akashima for helping on the prototyping of the master controller. The advices and and support are greatly treasured.

The author would also like to sincerely thanks to every students of Professor Sagara's Laboratory, especially Kenichi Imaike, Naoki Koresue, Kazuki Ueno, Masahiro Suganuma, Kazunori Kakumu and Masataka Urabe who have offered various support and suggestions in this work.

The author would also like to express heartfelt gratitude to Universiti Tun Hussein Onn Malaysia and the Government of Malaysia through the Ministry of Education who gave the opportunity and financial support that enable the author to pursue his studies in Kyushu Institute of Technology.

Finally, the author would like to thank both his parents for giving him never ending moral support, prayers and encouragements that only Allah can repay them; to his wife for the love and taking care of the children back in Malaysia; to his beautiful children for giving the author the strength to keep focused on the goals ahead; and to his brothers, families and friends for the continuous prayers.

References

[1] WM. Blake Tyrrell: "Star Trek as myth and television as mythmaker", The Journal of Popular Culture, 10(4):711-719, 1977.

[2] A. Pigafetta and R. A. Skelton: "Magellan's voyage: A narrative account of the first circumnavigation", Courier Dover Publications, 1994.

[3] J. Piccard: "Seven miles down: The story of the Bathyscaph Trieste", Putnam Publisher, First Edition, 1961.

[4] E. H. Oelkers, J. G. Hering and Z. Chen: "Water: Is there a global crisis?", Elements, 7(3):17-162, 2011.

[5] X. Chen: "Why do people misunderstand climate change? Heuristics, mental models and ontological assumptions", Climatic Change:108(1-2), pp. 31-46, 2011.

[6] P. H. Gleick: "Water in crisis: A guide to the world's fresh water resources", Ecological Applications 8:571-579, 1993.

[7] R. Moore: "A time to die: The untold story of the Kursk tragedy", New York: Crown Publishers, Random House, 2003.

[8] G. Williams *et al.*: "Thick and deformed Antarctic sea ice mapped with autonomous underwater vehicles", Nature Geoscience, 8:61-67, 2015.

[9] C. J. Cleveland, M. Hogan and P. Saundry: "Deepwater Horizon oil spill", In Encyclopedia of Earth, Environmental Information Coalition, National Council for Science and the Environment, 2011.

[10] R. A. Church, D. J. Warren, A. W. Hill and J. S. Smith: "The discovery of U-166: Rewriting history with new technology", Proceedings of Offshore Technology Conference, OCT 14136, 2000.

[11] J. C. Kincey *et al.*: "Assessing the Deepwater Horizon oil spill with the sentry autonomous underwater vehicle", Proceedings of 2011 IEEE/RSJ International Conference on Intelligent Robots and Systems, pp. 261-267, 2011.

[12] Internet article: "Scorpio 45: The UK's deep-sea rescuer", http://news.bbc.co.uk/2/hi/uk_news/4128728.stm (accessed on 26th December 2014).

[13] Internet sourced image: https://www.flickr.com/photos/pallo/208447927 from Pal-Loberg (accessed on 8th June 2015).

[14] Internet article: "Russia to buy Scorpio underwater robots after rescue of trapped sub", http://www.spacewar.com/2005/050809073845.lqzme3ki.html (accessed on 26th December 2014).

[15] Internet article: "Seaeye develops new markets while energy sector continues to boom", http://www.seaeye.com/whatsnew_2006.html (accessed on 26th December 2014).

[16] Internet article: "University of New Orleans to develop underwater spy robot", http://navaltoday.com/2011/08/09/university-of-new-orleans-to-develop-underwater-spy-robot-usa/ (accessed on 26th December 2013).

[17] Internet article: "Underwater robot sheds new light on Antarctic sea ice", http://www.whoi.edu/newsrelease/SeabedAntarctic (accessed on 7th June 2015).

[18] A. Bleicher: "The Gulf spill's lessons for robotics", IEEE Spectrum, vol. 47, no. 3, pp. 9-11, 2010.

[19] Internet article: "Rewriting history with new oilfield technology", http://www.geotimes.org/aug02/feature_oil.html (accessed on 8th June 2015).

[20] G. Troni, J. C. Kinsey, D. R. Yoerger and L. L. Whitcomb: "Field performance evaluation of new methods for in-situ calibration of attitude and doppler sensors for underwater vehicle navigation", Proceedings of 2012 International Conference on Robotics and Automation (ICRA), pp. 5334-5339, 2012.

[21] Internet article: "Underwater robot to stake Canada's Arctic claim", http://www.theepochtimes.com/n2/canada/efforts-on-track-to-determine-limits-of-continental-shelf-for-land-claim-to-un-commission-by-2013-32982.html (accessed on 8th June 2015).

[22] Internet article: "Underwater robots at work in Japan", http://cosmiclog.msnbc.msn.com/_news/2011/04/21/6508009-underwater-robots-at-work-in-japan (accessed on 8th June 2015).

[23] R. R. Murphy *et al.*: "Use of remotely operated marine vehicles at Minamisanriku and Rikuzentakata Japan for disaster recovery", Proceedings of 2011 IEEE International Symposium on Safety, Security, and Rescue Robotics (SSRR), pp. 19-25, 2011.

[24] F. Søreide: "Ships from the depths: Deepwater archaeology", Texas A & M University Press, pp. 29-40, 2011.

[25] M. A. Moline: "Remote environmental monitoring units: An autonomous vehicle for characterizing coastal environments", Journal of Atmospheric and Oceanic Technology, 22(11):1797-1808, 2005.

[26] D. R. Blidberg: "The development of autonomous underwater vehicles (AUVs); A brief summary", Proceedings of IEEE International Conference on Robotics and Automation (ICRA), 2001.

[27] V. Rigaud *et al.*: "UNION: underwater intelligent operation and navigation", IEEE Robotics & Automation Magazine, vol. 5, no. 1, pp. 25-35, 1998.

[28] M. Kyo *et al.*: "The sea trial of "KAIKO", the full ocean depth research ROV", Proceedings of MTS/IEEE OCEANS 1995, vol. 3, pp. 1991-1996, 1995.

[29] B. H. Jun *et al.*: "Workspace control system of underwater tele-operated manipulators on ROVs", Proceedings of IEEE/MTS OCEANS 2009-EUROPE, pp. 1-6, 2009.

[30] S. Sagara *et al.*: "Experiments on a floating underwater robot with a two-link manipulator", Artificial Life and Robotics 5:215-219, 2001.

[31] A. D. Bowen *et al.*: "The Nereus hybrid underwater robotic vehicle for global ocean science operations to 11,000m depth", Proceedings of IEEE/MTS OCEANS 2008, pp. 1-10, 2008.

[32] R. Yang *et al.*: "Modeling of a complex-shaped underwater vehicle", Proceedings of 2014 IEEE International Conference on Autonomous Robot Systems and Competitions (ICARSC), pp. 36-41, 2014.

[33] H. Wang, S. Rock and M. J. Lee: "OTTER: The design and development of an intelligent underwater robot", Autonomous Robots, vol. 3, issue 2-3, pp. 297-320, 1996.

[34] H. T. Choi, S. K. Choi and J. Yuh: "Development of an underwater robot, ODIN-iii", Proceedings of 2003 IEEE/RSJ International Conference on Intelligent Robots and Systems, vol. 1, pp. 836-841, 2003.

[35] J. Yuh *et al.*: "Design of a semi-autonomous underwater vehicle for intervention missions (SAUVIM)", Proceedings of International Symposium on Underwater Technology. pp. 63-68, 1998.

[36] G. De Novi *et al.*: "A new approach for a reconfigurable autonomous underwater vehicle for intervention", Proceedings of the 3rd. Annual IEEE International Systems Conference, pp. 23-26, 2009.

[37] J. Evans *et al.*: "Autonomous docking for Intervention-AUVs using sonar and video-based real-time 3D pose estimation", Proceedings of IEEE/MTS OCEANS 2003, vol. 4, pp. 2201-2210, 2003.

[38] D. M. Lane *et al.*: "AMADEUS: Advanced manipulation for deep underwater sampling", IEEE Robotics and Automation Magazine, vol. 4, no. 4, pp. 34-45, 997.

[39] T. Fujii and T. Ura: "Development of an autonomous underwater robot "Twin-Burger" for testing intelligent behaviors in realistic environments", Autonomous Robots, vol. 3, pp. 285-296, 1996.

[40] R. D. Christ and R. L. Wemli Sr.: "The ROV manual: A user guide for remotely operated vehicles", Butterworth-Henemann Publisher, Second edition, 2013.

[41] G. Antonelli: "Underwater robots: Motion and force control of vehicle-manipulator systems", 2nd Edition, Springer Tracts in Advanced Robotics, vol. 2, pp. 1-13, 2006.

[42] J. Yuh: "Design and Control of Autonomous Underwater Robots: A Survey", Autonomous Robots, vol. 8, pp. 7-24, 2000.

[43] M.W. Dunnigan and G.T. Russell: "Evaluation and reduction of the dynamic coupling between a manipulator and an underwater vehicle", IEEE Journal of Oceanic Engineering, vol. 23, no. 3, pp. 260-273, 1998.

[44] B. Xu, S. Abe, N. Sakagami and S. R. Pandian: "Robust nonlinear controller for underwater vehicle-manipulator systems", Proceedings of 2005 IEEE/ASME International Conference on Advanced Intelligent Mechatronics, pp. 711-716, 2005.

[45] S. Soylu, B. J. Buckham and R. P. Podhorodeski: "Development of a coordinated controller for underwater vehicle-manipulator systems", Proceedings of IEEE/MTS OCEANS 2008, pp. 1-9, 2008.

[46] H. Mahesh, J. Yuh and R. Lakshmi: "A coordinated control of an underwater vehicle and robot manipulator", Journal of Robotic Systems, vol. 8, pp. 339-370, 1991.

[47] N. Sarkar, J. Yuh, T. K. Podder: "Adaptive control of underwater vehicle-manipulator systems subject to joint limits", Proceedings of 1999 IEEE/RSJ International Conference on Intelligent Robots and Systems (IROS'99), vol. 1, pp. 142-147, 1999.

[48] G. Antonelli and S. Chiaverini: "Adaptive tracking control of underwater vehicle-manipulator systems based on the virtual decomposition approach", IEEE Transactions on Robotics and Automation, vol. 20, no. 3, pp. 594-602, 2004.

[49] S. Mohan and J. Kim: "Indirect adaptive control of an autonomous underwater vehicle-manipulator system for underwater manipulation tasks", Ocean Engineering, vol. 54, pp. 233-243, 2012.

[50] G. Antonelli and S. Chiaverini: "Fuzzy redundancy resolution and motion coordination for underwater vehicle-manipulator Systems", IEEE Transactions on Fuzzy Systems, vol. 11, no. 1, pp. 109-120, 2003.

[51] S. Soylu, B. J. Buckham and R. P. Podhorodeski: "Redundancy resolution for underwater mobile manipulators", Ocean Engineering, vol. 37, pp. 325-343, 2010.

[52] S. McMillan, D. E. Orin and R. B. McGhee: "Efficient dynamic simulation of an unmanned underwater vehicle with a manipulator", 1994 IEEE International Conference on Robotics and Automation (ICRA), vol. 2, pp. 1133-1140, 1994.

[53] T. J. Tarn, G. A. Shoults and S. P. Yang: "A dynamic model of an underwater vehicle with a robotic manipulator using Kane's method", Autonomous Robots, vol. 3, pp. 269-283, 1996.

[54] N. Kato and D. M. Lane: "Co-ordinated control of multiple manipulators in underwater robots", Proceedings of 1996 IEEE International Conference on Robotics and Automation, vol. 3, pp. 2505-2510, 1996.

[55] R. Mukherjee and Y. Nakamura: "Formulation and efficient computation of inverse dynamics of space robots", IEEE Transactions on Robotics and Automation, vol. 8, no. 3, pp. 400-406, 1992.

[56] N. Sarkar and T. K. Podder: "Coordinated motion planning and control of autonomous underwater vehicle-manipulator systems subject to drag optimization", IEEE Journal of Oceanic Engineering, vol. 26, no. 2, pp. 228-239, 2001.

[57] Y. Cui and J. Yuh: "A unified adaptive force control of underwater vehicle-manipulator systems (UVMS)", Proceedings of IEEE/RSJ International Conference on Intelligent Robots and Systems, pp. 553-558, 2003.

[58] J. Han, J. Park and W. K. Chung: "Robust coordinated motion control of an underwater vehicle-manipulator system with minimizing restoring moments", Ocean Engineering, vol. 38, pp. 1197-1206, 2011.

[59] O. Korkmaz, S.K. Ider, and M.K. Ozgoren: "Control of an underactuated underwater vehicle manipulator system in the presence of parametric uncertainty and disturbance", American Control Conference (ACC), pp. 578-584, 2013.

[60] T. W. McLain, S. M. Rock and M. J. Lee: "Experiments in the coordinated control of an underwater arm/vehicle system", Autonomous Robots, vol. 3, pp. 214-232, 1996.

[61] S. Sagara *et al.*: "Digital RAC for underwater vehicle-manipulator systems considering singular configuration", Artificial Life and Robotics 10:106-111, 2006.

[62] S. Sagara, T. Yatoh and T. Shimozawa: "Digital RAC with a disturbance observer for underwater vehicle-manipulator systems", Artificial Life and Robotics 15:270-274, 2010.

[63] G. Antonelli, T. I. Fossen and D. R. Yoerger: "Underwater robotics", Springer Handbook of Robotics, pp. 987-1008, 2008.

[64] J. O. Gray and D. G. Caldwell: "Advanced robotics and intelligent machines", Institution of Electrical Engineers, 1st Edn, 1996.

[65] A. A. Goldenberg *et al.*: "A remote manipulator for forestry operation", IEEE Transaction on Robotics and Automation, vol 11, no. 2, pp. 185-197, 1995.

[66] S.-U. Lee *et al.*: "Development of a Tele-operated Underwater Robotic System for maintaining a light-water type power reactor", Proceedings of International Joint Conference SICE-ICASE, pp. 3017-3021, 2006.

[67] F. Takemura and R. T. Shiroku: "Development of the actuator concentration type removable underwater manipulator", Proceedings of 11th International Conference on Control Automation Robotics and Vision (ICARCV), pp. 2124-2128, 2010.

[68] S. Soylu *et al.*: "Comprehensive underwater vehicle-manipulator system teleoperation", Proceedings of MTS/IEEE OCEANS 2010, pp. 1-8, 2010.

[69] J. J. Yao *et al.*: "Development of a 7-function hydraulic underwater manipulator system", Proceedings of 2009 IEEE International Conference on Mechatronics and Automation, pp. 1202-1206, 2009.

[70] M. Shibata, T. Saito, N. Sakagami and S. Kawamura: "Simultaneous operation of dual arm and body of mobile robots", Proceedings of 2010 IEEE International Conference on Robotics and Biomimetics (ROBIO), pp 2010, pp. 149-154, 2010.

[71] K. Kawano, T. Shimozawa, and S. Sagara: "A master-slave control system for a semi-autonomous underwater vehicle-manipulator system", Artificial Life and Robotics, vol. 16, pp. 465-468, 2012.

[72] M. Prats, J. J. Fernandez and P. J. Sanz: "An approach for semi-autonomous recovery of unknown objects in underwater environments", Proceedings of OPTIM, pp. 1452-1457, 2012.

[73] T. I. Fossen: "Guidance and control of ocean vehicles", John Wiley & Sons, pp. 431-452, 1995.

[74] S. Sagara: "Resolved acceleration control of underwater vehicle-manipulator systems: Continuous and discrete time approach", Underwater Vehicles, Alexander V. Inzartsev (Ed.), InTech, pp. 437-458, 2009.

[75] T. W. McLain and S. M. Rock: "Development and experimental validation of an underwater manipulator hydrodynamic model", International Journal of Robotics Research, vol. 17, no. 7, pp. 748-759, 1998.

[76] S. McMillan, D. E. Orin and R. B. McGhee: "Efficient dynamic simulation of an underwater vehicle with a robotic manipulator", IEEE Transactions on Systems, Man, and Cybernetics, 25(8):1194-1206, 1995.

[77] M. Tamura, "Experimental study on resolved acceleration control for underwater vehicle-manipulator systems", Ph.D. Thesis, Kyushu Institute of Technology, 2006. (in Japanese)

[78] B. L'evesque and M. J. Richard: "Dynamic analysis of a manipulator in a fluid environment", International Journal of Robotics Research, vol. 13, no. 3, pp. 221-231, 1994.

[79] J. Fukuda, "Experimental study on measuring propulsion of thruster for underwater vehicle using infrared sensor", Bachelor Degree Thesis, Kyushu Institute of Technology, 2008. (in Japanese)

[80] G. Antonelli: "Underwater robots", Springer, pp. 1194-1206, 2003.

[81] R. B. Ambar, S. Sagara and F. Takemura: "Development of manipulator joint for underwater vehicle-manipulator system using neodymium magnetic coupling - application on a 2-link manipulator", No.13-2 Proceeding of the 2013 JSME Conference on Robotics and Mechatronics, 2A2-M08, 2013.

[82] R. B. Ambar, S. Sagara and K. Imaike: "Experiment on a dual-arm underwater robot using resolved acceleration control method", Artificial Life and Robotics, 20(1): 34-41, 2014.

[83] R. Ravaud and G. Lemarquand: "Magnetic couplings with cylindrical and plane air gaps: Influence of the magnet polarization direction", Progress In Electromagnetics Research B, vol. 16, pp. 333-349, 2009.

[84] K. Yoshida, S. Abiko and J.M. Ota: "Development of an articulated gripper for an underwater ROV", Transaction of the Japan Society of Mechanical Engineers, ser.C, vol.68, no.675, pp. 237-244, 2002.

[85] M. Ishitsuka and K. Ishii: "Development and control of an underwater manipulator for AUV", Proceedings of Symposium on Underwater Technology and Workshop on Scientific Use of Submarine Cables and Related Technologies, pp. 337-342, 2007.

[86] T. W. McLain: "Modeling of underwater manipulator hydrodynamics with application to the coordinated control of an arm/vehicle System", Ph.D Thesis, Stanford University, 1995.

[87] K. N. Leabourne and S. M. Rock: "Model development of an underwater manipulator for coordinated arm-vehicle control", Proceedings of IEEE/MTS OCEANS 1998, vol.2, pp. 941-946, 1998.

[88] Q. Zhang, A. Zhang and K. Yan: "Improved design and control experiments of an underwater electric manipulator", Proceedings of 2006 SICE-ICASE International Joint Conference, pp. 3089-3093, 2006.

[89] S. Sagara, R. B. Ambar and F. Takemura: "A stereo vision system for underwater vehicle-manipulator systems-Proposal of a novel concept using pan-tilt-slide cameras", Journal of Robotics and Mechatronics, vol. 25, no. 5, pp. 785-794, 2013.